Vol. 6 No. 1 2022
pISSN 2586-1719 / eISSN 2799-3299

KJAR

Korean Journal of Abdominal Radiology

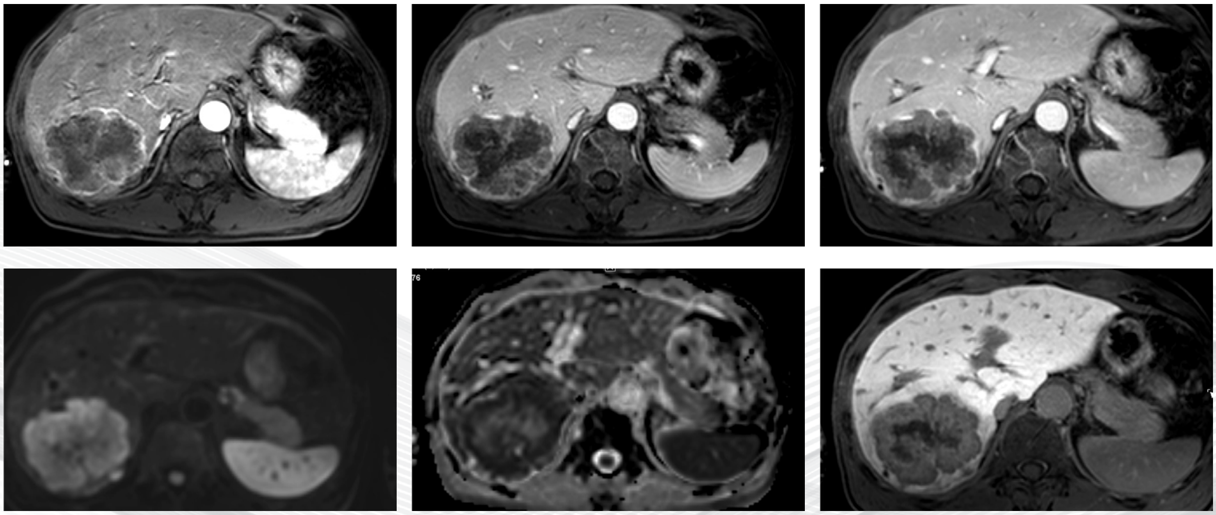

KSAR
대한복부영상의학회
Korean Society of Abdominal Radiology

KJAR
Korean Journal of Abdominal Radiology

Vol. 6 • No. 1 • July 15, 2022
pISSN 2586-1719 / eISSN 2799-3299

Editorial Board

Editor-in-Chief

이제희	강남세브란스병원	Jei Hee Lee	Gangnam Severance Hospital

Editors

강효진	서울대학교병원	Hyo-Jin Kang	Seoul National University Hospital
김보현	서울성모병원	Bohyun Kim	Seoul St. Mary's Hospital
안지현	원주세브란스기독병원	Jhii-Hyun Ahn	Wonju Severance Christian Hospital
유미혜	건국대학교병원	Mi Hye Yu	Konkuk University Medical Center
이은선	중앙대학교병원	Eun Sun LEE	Chung-Ang University Hospital
하홍일	한림대 성심병원	Hong-il Ha	Hallym University Sacred Heart Hospital

Publisher

양달모	강동경희대학교병원	Dal Mo Yang	Kyung Hee University Hospital at Gangdong

Layout Editor

송병규	성문각	Byeong Kyu Song	Sungmungak

Editorial Assistant

황순정	대한복부영상의학회	Soon Jeong Hwang	Korean Society of Abdominal Radiology

Publisher	Dal Mo Yang	Kyung Hee University Hospital at Gangdong
Editor-in-Chief	Jei Hee Lee	Gangnam Severance Hospital

KJAR Editorial Office
103-1103, The Sharp Seocho, 21, Seochojungang-ro 2-gil, Seocho-gu, Seoul 06720, Korea
Tel: +82-2-3474-1983 · Fax: +82-2-3474-1982 · E-mail: office@ksar.kr

Printing Office Sungmungak
#301, 72-15 Soopyo-ro, Jung-gu, Seoul 04543, Korea
Tel: +82-2-2266-9198 · Fax: +82-2-2275-9198 · E-mail: sbgsong@chol.com

Copyright © The Korean Society of Abdominal Radiology

KJAR
Korean Journal of Abdominal Radiology

Vol. 6 • No. 1 • July 15, 2022
pISSN 2586-1719 / eISSN 2799-3299

종 설 | Review Articles

원 저 | Original Article

증 례 | Case Reports

www.e-kjar.org
https://doi.org/10.52668/kjar.2022.00150

pISSN 2586-1719 / eISSN 2799-3299
Copyright © The Korean Society of Abdominal Radiology

Korean J Abdom Radiol 2022;6:1-11

Review Article

Review of Mass-Forming Intrahepatic Cholangiocarcinoma

Mi-Suk Park

Department of Radiology and Research Institute of Radiological Sciences, Severance Hospital, Yonsei University College of Medicine, Seoul, Korea

---

The incidence of intrahepatic cholangiocarcinoma (iCCA) is highest in Eastern countries, such as Thailand, South Korea, and China, but its incidence and mortality are increasing worldwide. Over recent decades, the worldwide age-standardized incidence for iCCA has been steadily increasing, whereas that for perihilar CCA and distal CCA has been decreasing. The macroscopic growth pattern of CCA is somewhat different according to the anatomic location of the tumor. iCCA can show three main patterns of growth: mass forming, periductal infiltrating, and intraductal growing. Morphologic classification is important to understand the mode of tumor spread, which is critical in predicting a tumor's resectability and in planning the extent of surgery. Furthermore, different macroscopic growth types are resulting in different imaging findings and different list of differential diagnosis. This review provides a comprehensive and critical overview of current knowledge and what is envisaged on the horizon for iCCA, focusing on mas-forming type.
1. Tumor growth pattern
2. Histological subtype of iCCA
3. Imaging phenotype and differential diagnosis of iCCA
4. Staging of iCCA
5. Preoperative prognostic prediction of iCCA

Keywords: Cholangiocarcinoma; Liver; Diagnosis

Overview of Cholangiocarcinoma

On the basis of the anatomic location of origin, cholangiocarcinomas (CCA) are classified into intrahepatic CCAs (iCCA), perihilar CCAs (pCCA), and distal CCAs (dCCA). iCCA is defined as an adenocarcinoma located in the periphery of the segmental bile ducts (second-order bile ducts), pCCA involves the right and/or left hepatic ducts and/or their junction, and dCCA arises in the common bile duct (1). The clinical significance of anatomic classification is that the tumor location implies the surgical extent. iCCA is typically treated through hepatectomy of the involved lobe or segments if resectable, while dCCA requires pancreaticoduodenectomy (1). pCCA requires resection of the confluence of the bile duct, and can also include perihilar tumors with a significant intrahepatic component (1).

The incidence of iCCA is highest in Eastern countries

Received: March 28, 2022 **Accepted:** April 25, 2022
Correspondence: Mi-Suk Park, MD
Department of Radiology, Severance Hospital, Yonsei University College of Medicine, 50-1 Yonsei-ro, Seodaemun-gu, Seoul, 03722, Korea
Tel: +82-2-2228-7400 Fax: +82-2-393-3035 E-mail: radpms@yuhs.ac
This is an Open Access article distributed under the terms of the Creative Commons Attribution Non-Commercial License (http://creativecommons.org/licenses/by-nc/4.0/) which permits unrestricted non-commercial use, distribution, and reproduction in any medium, provided the original work is properly cited.

such as Thailand, South Korea, and China, but its incidence and mortality are increasing worldwide (1). Over recent decades, the worldwide age-standardized incidence for iCCA has been steadily increasing, whereas that for pCCA and dCCA has been decreasing (1, 2). Several risk factors are known to be related to CCA. Although some are shared by all forms of CCA, others suggest greater specificity for one subtype and seem to be more important in different geographical regions (2). A common characteristic among many of these risk factors is that they are associated with chronic inflammation of the biliary epithelium and bile stasis, such as choledochal cysts, biliary stones, primary sclerosing cholangitis, and liver flukes (Opisthorchis viverrini, Clonorchis sinensis) (2). Several environmental toxins such as Thorotrast (banned in 1969), 1, 2-dichloropropane, asbestos, and tobacco smoking have been identified as risk factors for CCA. Several recognized risk factors such as viral infections (hepatitis B virus (HBV) and hepatitis C virus (HCV)), high alcohol consumption, obesity, metabolic syndrome, and nonalcoholic fatty liver disease have increased globally over recent decades and could be contributing to the increasing CCA rates (1-3). However, in most locations, the majority of CCA cases remains sporadic without any identifiable risk factors (1).

Tumor Growth Pattern

The macroscopic growth pattern of CCA is somewhat different according to the anatomic location. iCCAs can exhibit three main patterns of growth: mass forming, periductal infiltrating, and intraductal growth (1, 4). pCCAs and dCCAs present as peri-ductal infiltrating, nodular sclerosing tumors or, less frequently, as intraductal papillary tumors (4). Morphologic classification is important to understand the mode of tumor spread, which is critical in predicting a tumor's resectability and in planning the extent of surgery (5-7). In regard to longitudinal extension, submucosal tumor spread is predominant in periductal infiltrating types, whereas mucosal spread is more common in intraductal growing or mass-forming types (7). According to spread pattern, the length of discrepancy between microscopic and macroscopic tumor margins differs. In mucosal spreading, microscopic tumor spread beyond the macroscopic tumor margin has been reported to 10–20 mm, while 6–10 mm extensions have been observed submucosally (7). Therefore, to obtain a negative surgical margin, it is recommended to resect at least 20 mm past the ends of the macroscopic tumor in intraductal growing or mass-forming types and at least 10 mm in periductal infiltrating types (7, 8). Regarding transverse extension, periductal infiltrating type frequently extend beyond the bile duct wall and can directly involve adjacent organs or the hepatoduodenal ligament (7, 8). This can result in perineural invasion, vascular invasion, and lymphatic spread, which suggest a poor prognosis as well as affect tumor resectability (7, 9). Furthermore, different macroscopic growth types are associated with in different imaging findings and different lists of differential diagnoses.

This review provides a comprehensive and critical overview of the current literature for iCCA, focusing on mass-forming types.

Histological Subtype of iCCAs

Increasing evidence suggests that iCCAs are a heterogeneous group of tumors with varying etiologies, anatomic locations of origin, gross morphologies, histopathologies, and molecular features (1, 10). Histologically, iCCAs can take the form of conventional, cholangiolocarcinoma, and rare variants (1, 11). Conventional iCCAs can be further classified into two main histological subtypes, small and large bile duct types, according to the level or size of the affected duct (12, 13) (Table 1). Small bile duct iCCAs present as a small-sized tubular or acinar adenocarcinoma with nodular growth invading the liver parenchyma with minimal to no mucin production (12, 13). Large bile duct iCCAs arise in large intrahepatic bile ducts and comprise mucin-producing columnar tumor cells arranged in a large duct or papillary architecture (12, 13). Small duct iCCAs are associated with chronic liver diseases including viral hepatitis without known precursor lesions (1, 10, 12, 13). In contrast, large-duct-type iCCAs are associated with chronic bile duct disease, including an intrahepatic stone or parasitic infection, and are thought to arise from precursor lesions including biliary intraepithelial lesions or intraductal papillary neoplasms of the bile duct; and progress to invasive intraductal neoplasms, periductal, or mass-forming types of tumors (10, 12-14).

Table 1. Pathologic classification of conventional intrahepatic cholangiocarcinomas

	Large duct type	Small duct type
Pathologic features		
Putative cell of origin	Peribiliary glands (Mucinous cells/columnar cholangiocyst)	Interlobular bile duct (Cuboidal cholangiocyte)
Stromal desmoplasia	Abundant	Minimal
Mucin	Abundant	Minimal
Gene mutation	KRAS, TP53	IDH1, IDH2, FGFR2
Lymph node metastasis	Frequent	Rare
Imaging features		
Arterial enhancement		
Diffuse/hetero	Rare	More common
No enhancement	Frequent	Rare
Bile duct invasion	Frequent	Rare
Target appearance	More frequent	Less frequent
Lymph node enlargement	Frequent	Rare
Clinical features		
Common underlying condition	Biliary disease (Hepatolithiasis/ primary sclerosing cholangitis)	Liver disease (Chronic hepatitis/liver cirrhosis)
Prognosis	Worse	Better

IDH = isocitrate dehydrogenase; FGFR = fibroblast growth factor receptor

Imaging Phenotype and Differential Diagnosis of iCCA

The imaging features of iCCAs are thought to reflect the pathologic subtype and gross morphology of the tumor (Table 1).

The typical imaging features of mass-forming iCCAs are a nonencapsulated mass of lobulated or irregular contour accompanied by hepatic capsular retraction and dilated peripheral bile ducts (7, 15). On the arterial phase of dynamic contrast-enhanced CT and MRI images, iCCAs typically exhibit peripheral rim enhancement or diffuse hypoenhancement (6, 7, 15). On portal venous or delayed phase, iCCAs present with peripheral washout or progressive centripetal enhancement (6, 7, 15). Hypercellularity in the periphery of tumors with small extracellular volume contributes to peripheral enhancement in the arterial phase and peripheral washout appearance in the portal venous phase and/or delayed phase (7, 15). On the other hand, central hypovascularity and mild progressive enhancement reflect the desmoplastic stroma with sparse tumor cells in the central portion of the tumor (7, 15). The different compositions of the periphery and center of the tumor can present as a target-like appearance with peripheral hyperintensity and central hypointensity on high-b-value diffusion weighted images (DWI), reflecting the hypercellularity of the peripheral portion versus hypocellularity of the central portion with a fibrous component (16). On the hepatobiliary phase (HBP) of gadoxetic acid-enhanced MRI, the reversed target-like appearance of peripheral hypointensity and central cloud-like hyperintensity can be of value in the diagnosis of iCCAs (7, 17) (Fig. 1).

Recently, atypical imaging features of mass-forming iCCAs have been reported more frequently, and several studies have suggested a subclassification based on imaging features (7, 10, 14, 18). A recent single-center study divided mass-forming iCCAs into three groups according to arterial enhancement pattern on MRI – peripheral rim enhancement, diffuse hypoenhancement, or diffuse hyperenhancement (19). Patients with diffuse hyperenhancement type on arterial phase exhibited more frequent chronic liver disease (13 of 20; 65%), less frequent vascular invasion (6 of 20; 30%), and less

Fig. 1. A 66-year-old man with a mass-forming iCCA.
An approximately 8 cm mass-forming intrahepatic cholangiocaricnoma at liver segment 7. Contrast enhanced dynamic CT show peripheral enhancing lobulated mass on arterial phase (A) and persistent peripheral enhancement on portal phase (B) and delay phase (C). Gadoxetic acid enhanced MRI demonstrates peripheral enhancing mass on arterial (D), portal (E), and transisitonal phase (F) and target appearance on diffusion weighted image (G), ADC map (H) and hepatobiliary phase (I).

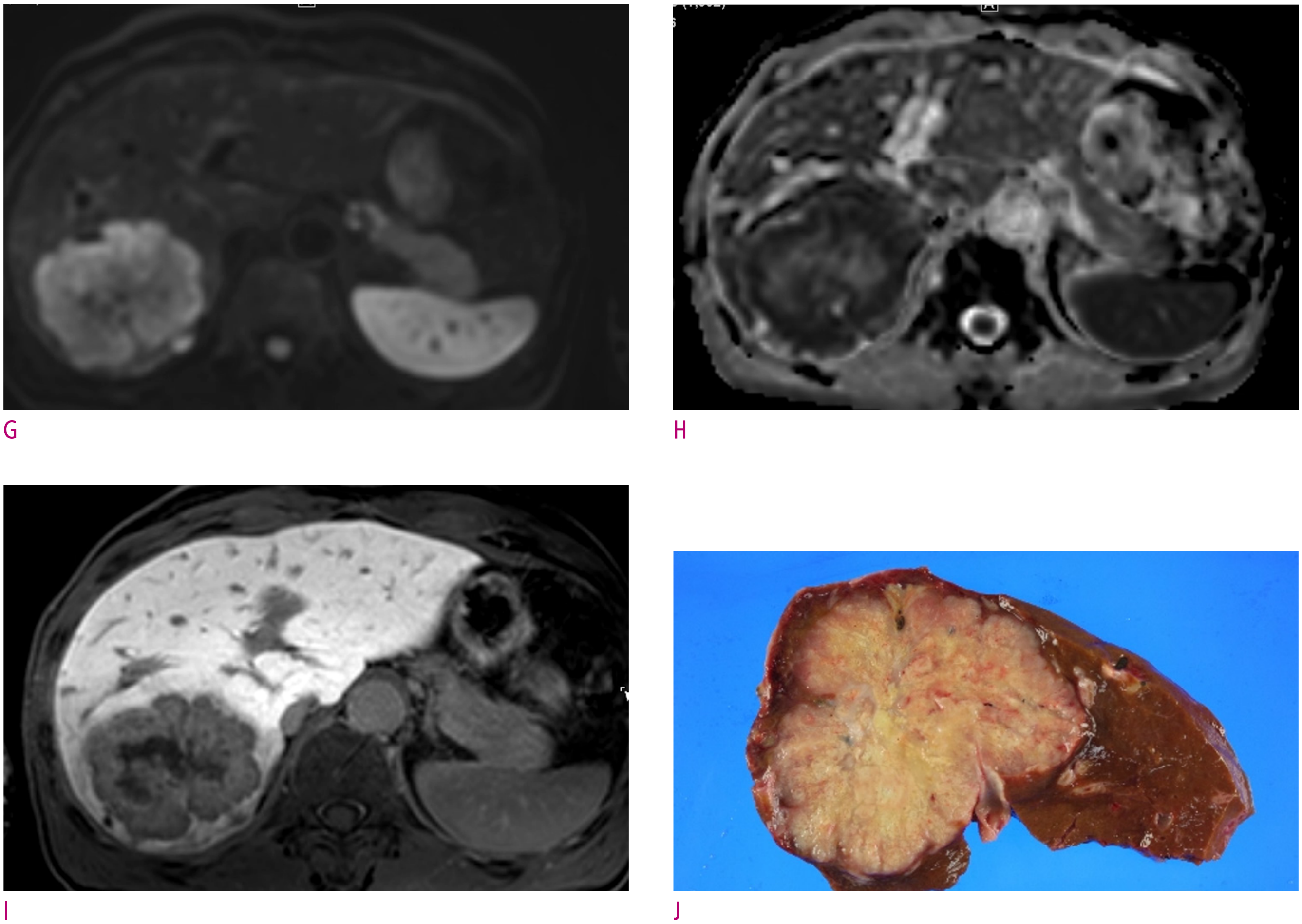
G

H

I

J

Fig. 1. A gross pathologic specimen demonstrates about 7.5 cm mass-forming intrahepatic cholangiocaricnoma with Clonorchis sinensis infection and chronic cholangitis of nontumor liver pathology (J).

frequent tumor necrosis (3 of 20; 15%) compared to peripheral rim enhancement or diffuse hypoenhancement type (19) (Fig. 2). Another study recommended subdivision of mass-forming iCCAs into parenchymal and ductal types and revealed more frequent arterial hypervascularity and better overall survival in the parenchymal type (10, 19-21).

The diffuse arterial phase hyperenhancement pattern of iCCAs can mimic HCCs. Sharing risk factors of chronic liver disease makes it more difficult to differentiate between on through imaging. A case-control study to differentiate iCCAs from HCCs in patients with cirrhosis confirmed that the typical enhancement patterns of iCCAs – peripheral/rim enhancement in the AP followed by persistent or progressive contrast enhancement in the PVP and TP – are more frequent than HCCs in cirrhotic livers using gadoxetic acid–enhanced MRI, similar to extracellular contrast agent–enhanced CT and MRI in noncirrhotic livers (18-21). In addition to the dynamic enhancement pattern, peritumoral bile duct dilatation and target appearance were independent and significant factors suggestive of iCCAs. A well-known pitfall of gadoxetic acid–enhanced MRI is the misinterpretation of atypical iCCA as HCC owing to the "pseudo washout" effect (7). To avoid false diagnoses, an exclusive washout definition on PVP of gadoxetic acid–enhanced MRI was suggested but led to a significant decrease in sensitivity for HCCs (7, 21). Considering the extremely lower prevalence of atypical (global wash in and washout) enhancing iCCAs compared to HCCs, however, it is difficult to accept the washout definition exclusively based on PVP in daily practice. Moreover, the prognosis following treatment with the same method used for equivalent-stage HCCs has not been well-established and has undefined clinical relevance (22-24).

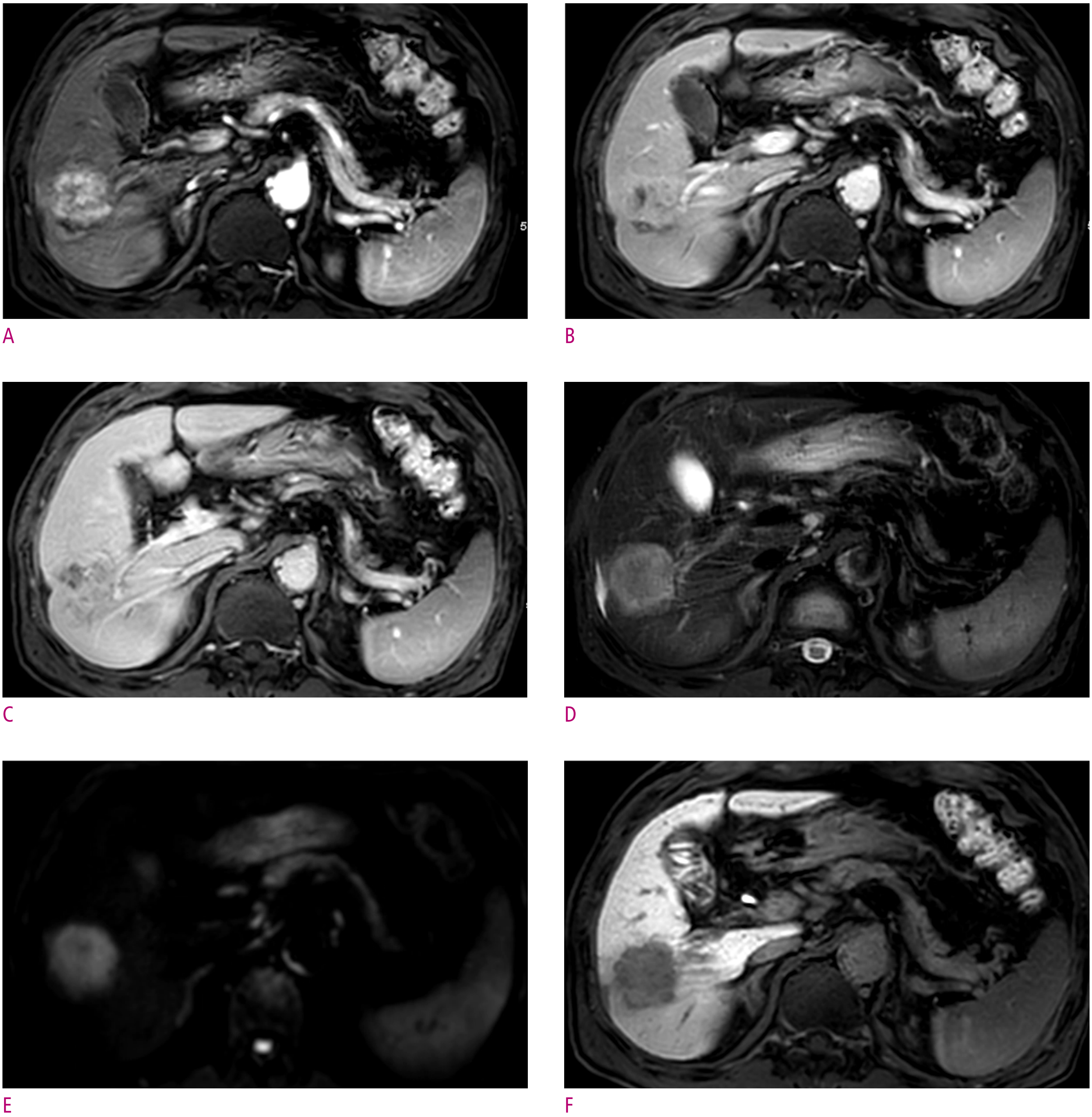

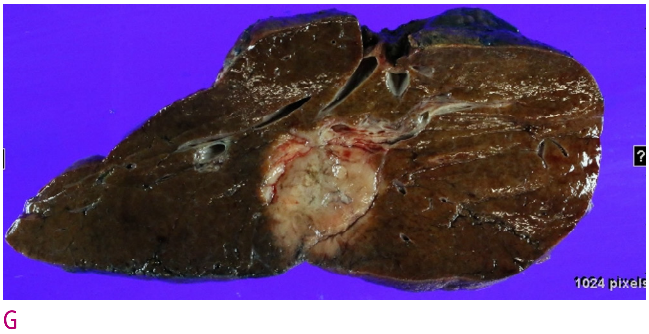

Fig. 2. A 78-year-old man with liver cirrhosis.
Gadoxetic acid enhanced MRI demonstrates an approximately 3 cm hypervascular mass on arterial phase (A). On portal venous (B) and transitional phase (C), the mass shows heterogeneous iso-intensity. It shows moderate high signal intensity on T2WI (D), diffusion restriction on DWI (E), and hypointensity on hepatobiliary phase (F). A gross pathologic specimen demonstrates about 3 cm mass-forming intrahepatic cholangiocaricnoma, small duct type with cholangiololcellular differentiation, with macro- and micro-nodular cirrhosis of nontumor liver pathology (G).

Combined hepatocellular cholangiocarcinomas have been reported to be more commonly misdiagnosed as iCCAs rather than HCCs on preoperative imaging even though they can mimic either (25). The presence of the target-like appearance on hepatobiliary phase images, the absence of major vascular thrombosis, and the presence of intrahepatic bile duct dilatation suggest iCCAs over combined hepatocellular cholangiocarcinomas. The preoperative differential diagnosis of iCCAs on the basis of imaging features typically is not possible, and biopsies should be considered for confirmation of the diagnosis (25). Benign lesions mimicking iCCAs include liver abscess and sclerosing hemangioma (Fig. 3).

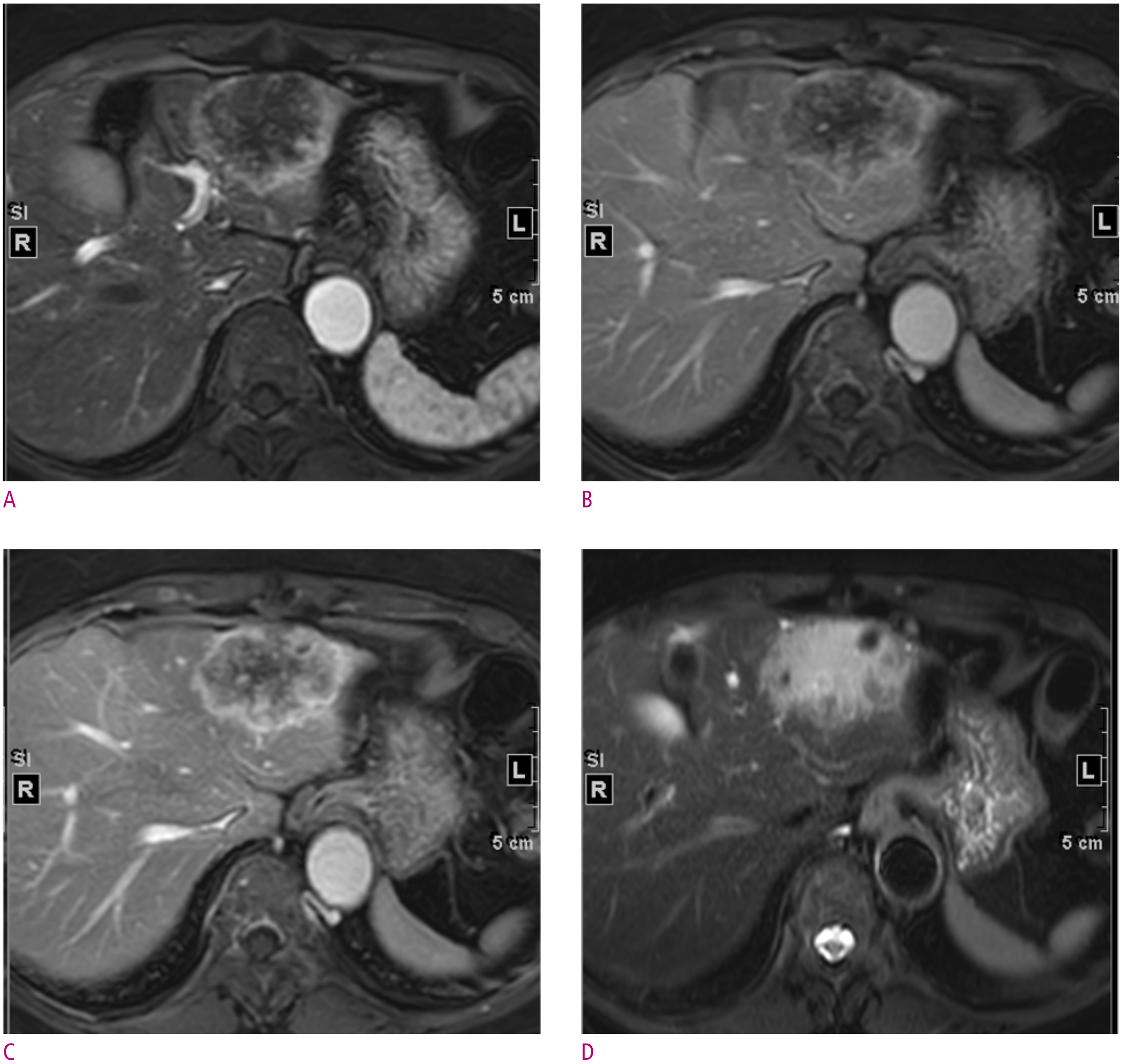

Fig. 3. A 72-year-old woman with a sclerosing hemangioma.
Extracellular agent enhanced dynamic MRI show peripheral, progressive enhancing lobulated mass at liver segment 3 on arterial phase (A), portal phase (B), and delay phase (C). The mass shows moderately high signal intensity on T2 weighted image (D) with several dark signal foci.

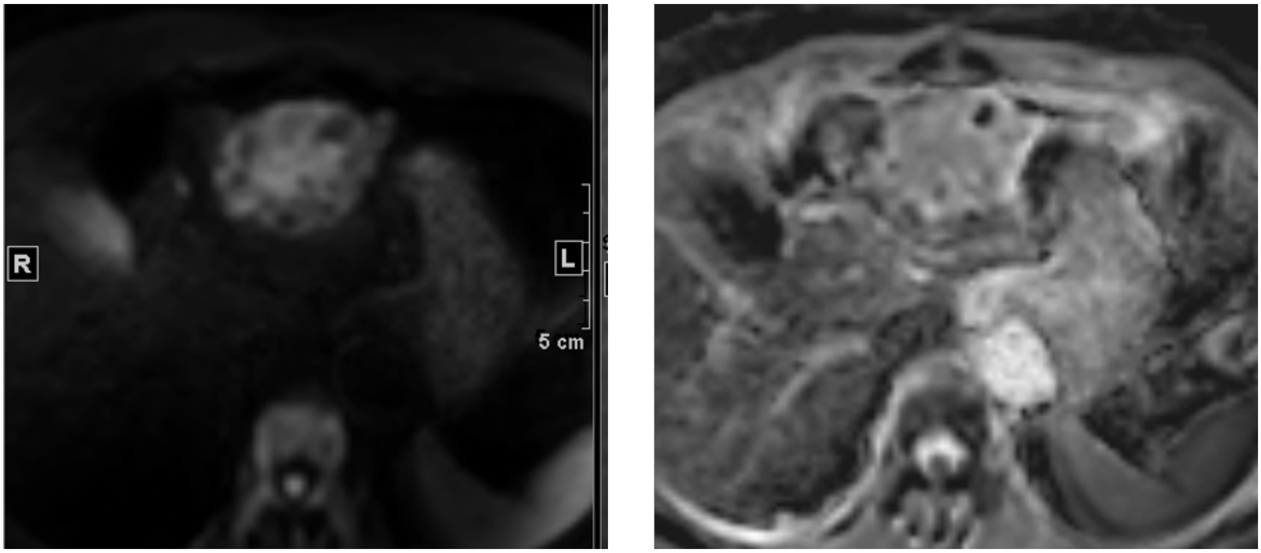

E

F

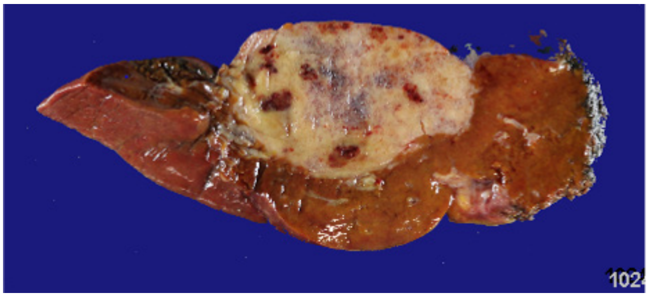

G

Fig. 3. On diffusion weighted images (E) the mass show equivocal diffusion restriction with 1.806 ADC value (F). On pathology (G) the mass was a fibrotic lesion composed of various size blood vessels with organizing thrombi and partial sclerosis, consistent with sclerosing hemangioma.

Staging of iCCAs

iCCAs, pCCAs, and dCCAs differ in tumor characteristics and have distinguishing American Joint Committee on Cancer (AJCC) tumor-node-metastasis (TNM) stage (1). Before the 7th edition of the AJCC system in 2010, iCCAs shared the same stage as HCCs (26-29). In the 7th edition, the size cut-off of 5 cm in multiple tumors was discarded, and periductal infiltrating tumor growth type was considered to indicate a poor prognosis, staged as T4. In the 8th edition of the AJCC system, several major changes were made to the T staging of iCCAs – the T1 stage (solitary tumor without vascular invasion) was divided into T1a and T1b stages using a size cut-off of 5 cm; T2a (solitary tumor with vascular invasion) and T2b (multiple tumors with or without vascular invasion) stages in the 7th edition were unified into the T2 stage; extrahepatic organ invasion replaced periductal invasion for determination of the T4 stage (26-29) (Table 2). Since surgical resection is the only potentially curative treatment for patients with cholangiocarcinoma, it is important to accurately determine its clinical stage using imaging studies to identify surgical candidates. A recent multicenter cohort study showed that MRI exhibited superior sensitivity to CT for diagnosing tumor multiplicity, particularly gadoxetic acid–enhanced MRI (28). Recent studies have demonstrated that intrahepatic metastasis is an important prognostic factor for iCCAs, and T2 tumors with multiplicity showed a worse prognosis than T3 tumors in the AJCC 8th edition, with one study even classifying them into the M1a stage (29). It is critical to detect intrahepatic metastasis in iCCA, and the use of gadoxetic acid–enhanced MRI is recommended in addition to CT before surgery to detect additional intrahepatic metastases (28).

Table 2. AJCC TNM staging of intrahepatic cholangiocarcinomas: 7th vs 8th Edition

<table>
<tr><th colspan="4">AJCC 7th Staging</th><th colspan="4">AJCC 8th Staging</th></tr>
<tr><td colspan="8">T staging</td></tr>
<tr><td colspan="4">T1: Solitary tumor without vascular invasion</td><td colspan="4">T1a: Solitary tumor ≤5 cm without vascular invasion
T1b: Solitary tumor >5 cm without vascular invasion</td></tr>
<tr><td colspan="4">T2a: Solitary tumor with vascular invasion
T2b: Multiple tumors, with or without vascular invasion</td><td colspan="4">T2: Solitary tumor with intrahepatic vascular invasion or multiple tumors with or without vascular invasion</td></tr>
<tr><td colspan="4">T3: Tumor perforating the visceral peritoneum or involving local hepatic structures by direct invasion</td><td colspan="4">T3: Tumor perforating the visceral peritoneum</td></tr>
<tr><td colspan="4">T4: Tumor with periductal invasion</td><td colspan="4">T4: Tumor involving local extrahepatic structures by direct invasion</td></tr>
<tr><td colspan="8">TNM Staging</td></tr>
<tr><td>T</td><td>N</td><td>M</td><td>Stage</td><td>T</td><td>N</td><td>M</td><td>Stage</td></tr>
<tr><td>T1</td><td>N0</td><td>M0</td><td>I</td><td>T1a</td><td>N0</td><td>M0</td><td>IA</td></tr>
<tr><td>T2a</td><td>N0</td><td>M0</td><td>IIA</td><td>T1b</td><td>N0</td><td>M0</td><td>IB</td></tr>
<tr><td>T2b</td><td>N0</td><td>M0</td><td>IIB</td><td>T2</td><td>N0</td><td>M0</td><td>II</td></tr>
<tr><td>T3</td><td>N0</td><td>M0</td><td>IIIA</td><td>T3</td><td>N0</td><td>M0</td><td>IIIA</td></tr>
<tr><td>T4</td><td>N0</td><td>M0</td><td>IIIB</td><td>T4</td><td>N0</td><td>M0</td><td>IIIB</td></tr>
<tr><td>Any T</td><td>N1</td><td>M0</td><td>IIIB</td><td>Any T</td><td>N1</td><td>M0</td><td>IIIB</td></tr>
<tr><td>Any T</td><td>Any N</td><td>M1</td><td>IV</td><td>Any T</td><td>Any N</td><td>M1</td><td>IV</td></tr>
</table>

AJCC = American Joint Committee on Cancer; TNM = tumor-node-metastasis.

Preoperative Prognostic Prediction of iCCA

As mentioned earlier, several imaging features with better or worse prognosis have been reported based on tumor heterogeneity of iCCAs. Diffuse or nodular arterial phase hyperenhancement is the representative imaging feature correlated with better overall and/or progression-free survival after surgical resection (19). Histologically, the area of hyperenhancement is correlated with the hypercellular component, whereas areas of delayed phase enhancement correspond to the fibrosis component (7, 19). A recent study correlated enhancement pattern on CT with the subtype of conventional iCCA as small and large duct types, which exhibit different tumor aggressiveness and clinical outcomes (30). They revealed that arterial hyperenhancement or rim enhancement was common in the small duct type, while arterial hypoenhancement was common in the large duct type (30). A multicenter retrospective study suggested the use of preoperative MRI prognostic models that include serum CA19-9 and four MRI features (bile duct invasion, tumor multiplicity, lymph node metastasis, and cirrhosis) for calculating the overall survival of mass-forming iCCAs (31). The preoperative MRI prognostic score showed comparable discriminatory performance to pathologic staging systems and might be used to determine an optimal treatment strategy (31).

Conclusions

iCCAs are highly aggressive and heterogeneous tumors with a poor prognosis. Tumor resection remains the only potentially curative option for these patients, and preoperative imaging diagnosis, resectability assessment, and accurate tumor staging are of great importance. Current concepts regarding risk factors, tumor biology, and histologic classifications might also allow for a better understanding of the diverse imaging features of iCCAs. Therefore, knowledge of the updated classification systems and current principles for management of iCCAs might be helpful in determining a clinically relevant interpretation of the imaging studies. Despite the recent advanced knowledge of iCCAs, it remains an open field of research with important gaps that need to be filled. Therefore, all efforts must be gathered to ultimately decipher the complexity of iCCAs.

References

1. Banales JM, Marin JJG, Lamarca A, Rodrigues PM, Khan SA, Roberts LR, et al. Cholangiocarcinoma 2020: the next horizon in mechanisms and management. Nat Rev Gastroenterol Hepatol 2020;17:557-588.
2. Khan SA, Tavolari S, Brandi G. Cholangiocarcinoma: Epidemiology and risk factors. Liver Int 2019;39 Suppl 1:19-31.
3. Clements O, Eliahoo J, Kim JU, Taylor-Robinson SD, Khan SA. Risk factors for intrahepatic and extrahepatic cholangiocarcinoma: a systematic review and meta-analysis. J Hepatol 2020;72:95-103.
4. Nakanuma Y, Sato Y, Harada K, Sasaki M, Xu J, Ikeda H. Pathological classification of intrahepatic cholangiocarcinoma based on a new concept. World J Hepatol 2010;2:419-427.
5. Blechacz B, Komuta M, Roskams T, Gores GJ. Clinical diagnosis and staging of cholangiocarcinoma. Nat Rev Gastroenterol Hepatol 2011;8:512-522.
6. Joo I, Lee JM. Imaging bile duct tumors: pathologic concepts, classification, and early tumor detection. Abdom Imaging 2013;38:1334-1350.
7. Joo I, Lee JM, Yoon JH. Imaging Diagnosis of Intrahepatic and Perihilar Cholangiocarcinoma: Recent Advances and Challenges. Radiology 2018;288:7-13.
8. Akamatsu N, Sugawara Y, Hashimoto D. Surgical strategy for bile duct cancer: advances and current limitations. World J Clin Oncol 2011;2:94-107.
9. de Jong MC, Nathan H, Sotiropoulos GC, Paul A, Alexandrescu S, Marques H, et al. Intrahepatic cholangiocarcinoma: an international multi-institutional analysis of prognostic factors and lymph node assessment. J Clin Oncol 2011;29:3140-3145.
10. Rhee H, Kim MJ, Park YN, An C. A proposal of imaging classification of intrahepatic mass-forming cholangiocarcinoma into ductal and parenchymal types: clinicopathologic significance. Eur Radiol 2019;29:3111-3121.
11. Kendall T, Verheij J, Gaudio E, Evert M, Guido M, Goeppert B, et al. Anatomical, histomorphological and molecular classification of cholangiocarcinoma. Liver Int 2019;39 Suppl 1:7-18.
12. Hayashi A, Misumi K, Shibahara J, Arita J, Sakamoto Y, Hasegawa K, et al. Distinct Clinicopathologic and Genetic Features of 2 Histologic Subtypes of Intrahepatic Cholangiocarcinoma. Am J Surg Pathol 2016;40:1021-1030.
13. Akita M, Fujikura K, Ajiki T, Fukumoto T, Otani K, Azuma T, et al. Dichotomy in intrahepatic cholangiocarcinomas based on histologic similarities to hilar cholangiocarcinomas. Mod Pathol 2017;30:986-997.
14. Aishima S, Oda Y. Pathogenesis and classification of intrahepatic cholangiocarcinoma: different characters of perihilar large duct type versus peripheral small duct type. J Hepatobiliary Pancreat Sci 2015;22:94-100.
15. Chung YE, Kim MJ, Park YN, Choi JY, Pyo JY, Kim YC, et al. Varying appearances of cholangiocarcinoma: radiologic-pathologic correlation. Radiographics 2009;29:683-700.
16. Park HJ, Kim YK, Park MJ, Lee WJ. Small intrahepatic mass-forming cholangiocarcinoma: target sign on diffusion-weighted imaging for differentiation from hepatocellular carcinoma. Abdom Imaging 2013;38:793-801.
17. Jeong HT, Kim MJ, Kim YE, Park YN, Choi GH, Choi JS. MRI features of hepatocellular carcinoma expressing progenitor cell markers. Liver Int 2012;32:430-440.
18. Kim SA, Lee JM, Lee KB, Kim SH, Yoon SH, Han JK, et al. Intrahepatic Mass-forming Cholangiocarcinomas: Enhancement Patterns at Multiphasic CT, with Special Emphasis on Arterial Enhancement Pattern-Correlation with Clinicopathologic Findings. Radiology 2011;260:148-157.
19. Min JH, Kim YK, Choi SY, Kang TW, Lee SJ, Kim JM, et al. Intrahepatic Mass-forming Cholangiocarcinoma: Arterial Enhancement Patterns at MRI and Prognosis. Radiology 2019;290:691-699.
20. Rimola J, Forner A, Reig M, Vilana R, de Lope CR, Ayuso C, et al. Cholangiocarcinoma in cirrhosis: absence of contrast washout in delayed phases by magnetic resonance imaging avoids misdiagnosis of hepatocellular carcinoma. Hepatology 2009;50:791-798.
21. Choi SH, Lee SS, Kim SY, Park SH, Park SH, Kim KM, et al. Intrahepatic Cholangiocarcinoma in Patients with Cirrhosis: Differentiation from Hepatocellular Carcinoma by Using Gadoxetic Acid-enhanced MR Imaging and Dynamic CT. Radiology 2017;282:771-781.
22. Kim JH, Won HJ, Shin YM, Kim KA, Kim PN. Radiofrequency ablation for the treatment of primary intrahepatic cholangiocarcinoma. AJR Am J Roentgenol 2011;196:W205-209.
23. Takahashi K, Obeid J, Burmeister CS, Bruno DA, Kazimi MM, Yoshida A, et al. Intrahepatic Cholangiocarcinoma in

the Liver Explant After Liver Transplantation: Histological Differentiation and Prognosis. Ann Transplant 2016;21:208-215.
24. Korean Society of Abdominal R. Diagnosis of Hepatocellular Carcinoma with Gadoxetic Acid-Enhanced MRI: 2016 Consensus Recommendations of the Korean Society of Abdominal Radiology. Korean J Radiol 2017;18:427-443.
25. Fowler KJ, Sheybani A, Parker RA, 3rd, Doherty S, E MB, Chapman WC, et al. Combined hepatocellular and cholangiocarcinoma (biphenotypic) tumors: imaging features and diagnostic accuracy of contrast-enhanced CT and MRI. AJR Am J Roentgenol 2013;201:332-339.
26. Kang SH, Hwang S, Lee YJ, Kim KH, Ahn CS, Moon DB, et al. Prognostic comparison of the 7th and 8th editions of the American Joint Committee on Cancer staging system for intrahepatic cholangiocarcinoma. J Hepatobiliary Pancreat Sci 2018;25:240-248.
27. Lee AJ, Chun YS. Intrahepatic cholangiocarcinoma: the AJCC/UICC 8th edition updates. Chin Clin Oncol 2018;7:52.
28. Kim YY, Yeom SK, Shin H, Choi SH, Rhee H, Park JH, et al. Clinical Staging of Mass-Forming Intrahepatic Cholangiocarcinoma: Computed Tomography Versus Magnetic Resonance Imaging. Hepatol Commun 2021;5:2009-2018.
29. Lamarca A, Santos-Laso A, Utpatel K, La Casta A, Stock S, Forner A, et al. Liver Metastases of Intrahepatic Cholangiocarcinoma: Implications for an Updated Staging System. Hepatology 2021;73:2311-2325.
30. Fujita N, Asayama Y, Nishie A, Ishigami K, Ushijima Y, Takayama Y, et al. Mass-forming intrahepatic cholangiocarcinoma: Enhancement patterns in the arterial phase of dynamic hepatic CT - Correlation with clinicopathological findings. Eur Radiol 2017;27:498-506.
31. Rhee H, Choi SH, Park JH, Cho ES, Yeom SK, Park S, et al. Preoperative magnetic resonance imaging-based prognostic model for mass-forming intrahepatic cholangiocarcinoma. Liver Int 2022.

종괴 형성 간내 담관암에 대한 고찰

박미숙
연세대학교 세브란스병원 영상의학과

초 록

T간내 담관암은 대만, 대한민국, 중국 등 동아시아 지역에서 유병률이 높다. 최근에는 간문부와 간외 담관암의 유병률은 줄어들고 있으나 간내 담관암의 유병률과 치사율은 늘고 있다. 담관암의 형태는 종양의 위치에 따라 조금씩 다른 경향이 있다. 간내 담관암은, 종괴 형성, 담관주위 침윤성, 혹은 담관 내 종양의 세 가지 패턴을 주로 보여준다. 이러한 형태에 따라서 영상 소견이 다르고 그에 따라 다른 감별 진단을 하게 된다. 이 종설은 종괴 형성 간내 담관암에 대한 현재까지 알려진 사실에 대한 전반적인 고찰을 하고자 한다.

www.e-kjar.org
https://doi.org/10.52668/kjar.2022.00129

pISSN 2586-1719 / eISSN 2799-3299
Copyright © The Korean Society of Abdominal Radiology

Korean J Abdom Radiol 2022;6:12-21

Review Article

조영증강초음파의 원리와 간세포암 진단

강효진[1,2], 이재영[1,2], 이정민[1,2]
[1]*서울대학교병원 영상의학과*
[2]*서울대학교 의과대학 의학과*

The Principle of Contrast-enhanced Ultrasound and the Diagnosis of Hepatocellular Carcinoma

Hyo-Jin Kang[1,2], Jae Young Lee[1,2], Jeong Min Lee[1,2]
[1]*Department of Radiology, Seoul National University Hospital, Seoul, Korea*
[2]*Department of Radiology, Seoul National University College of Medicine, Seoul, Korea*

Contrast-enhanced ultrasound (CEUS) is a specialized ultrasound performed with microbubble contrast agents. It is valuable for characterizing hepatic lesions without renal toxicity or radiation hazard. This review provides up-to-date practical knowledge of CEUS to make the interpretation of CEUS more accurate and clinically relevant. It includes the principle of CEUS, comparison of two kinds of contrast agents (the pure blood-pool agent and the Kupffer agent), diagnostic criteria for hepatocellular carcinoma, and its role in the diagnostic algorithms.

Keywords: Hepatocellualr carcinoma; Contrast-enhanced ultrasound; Diagnosis; Microbubble

서론

조영증강초음파 (contrast-enhanced ultrasound)는 미세기포를 조영제로 사용하여 폐로 대사되는 특징이 있어 신기능 저하 환자에서 안전하게 사용할 수 있고, 방사선 노출이 없으며, 갑상선 기능에 방해가 없고, 조영제 과민반응이 요오드 보다 낮다는 장점이 있다 (1-3). 또한, 혈역학적 (hemodynamic) 정보를 실시간으로 평가할 수 있어 CT 혹은 MRI 검사에서 실제 동맥기 및 문맥기와 영상획득 시각의 차이로 발생하는 오류를 최소화 할 수 있다. 초음파 조영제는 혈관 내피 (vascular endothelium)를 통과하지 못하여 세포 간질로의 조영제 이동이 없어, 순수한 혈관 영상을 생성하므로, CT 혹은 MRI 검사와 차별화 되는 영상 소견을 보인다. 이러한 조영증강초음파의 고유한 특징들은 간세포암 진단에 유용하게 사용될 수 있다. 이 논문에서는, 조영증강초음파의 원리, 특징 및 간세포암의 진단 기준에 대해 논의하고자 한다.

조영증강초음파의 원리

초음파 조영제는 구형의 지질 혹은 알부민 외피 내부에 용해도가 낮은 기체를 포함하여 구성된 미세기포이

Received: March 7, 2022 **Revised:** May 19, 2022 **Accepted:** May 19, 2022
Correspondence: Hyo-Jin Kang, MD, PhD
Department of Radiology, Seoul National University College of Medicine, 101 Daehangno, Jongno-gu, Seoul, 03080, Korea
Tel: +82-2-2072-3107 Fax: +82-2-743-6385 E-mail: loveyoon@snu.ac.kr
This is an Open Access article distributed under the terms of the Creative Commons Attribution Non-Commercial License (http://creativecommons.org/licenses/by-nc/4.0/) which permits unrestricted non-commercial use, distribution, and reproduction in any medium, provided the original work is properly cited.

다. 일반적으로 초음파 영상은 probe에서 발생한 초음파가 조직에 도달하여 진동 (oscillation)을 만들고, 이때 반사되어 돌아오는 반사파를 영상화 하는 원리이다. 이 진동은 선형진동 (linear oscillation)으로 입사된 초음파와 선형 관계의 반사파를 발생시킨다. 반면 초음파 조영제의 경우, 미세기포에 초음파가 도달하면 공명 (resonance)을 통해 미세기포 자체에서 압축과 확장을 반복하며 비선형진동 (non-linear oscillation)이 발생하게 되어, 다른 주파수를 가진 반사파를 발생시킨다. 조영증강초음파 영상은 미세기포에서 발생하는 비선형 반사파에서 조직에서 발생하는 선형 반사파를 구분하여 시각화 한 영상이다 (4). 비선형 반사파를 구분하기 위해 선형 반사파를 상쇄시키는 방법은 pulse inversion 방식과 amplitude modulation 방식이 있다. Pulse inversion 방식은 입사파와 정반대의 극성 (polarity)을 가진 파를 이용하여 선형 반사파를 상쇄시키고 비선형 반사파의 진폭은 증가시키는 원리이다. Amplitude modulation 방식은 입사파의 정배수의 진폭을 가진 파를 이용하여 선형 반사파를 상쇄시키고 비선형 반사파의 진폭은 증가시키는 원리이다 (5).

조영증강초음파에 사용되는 Mechanical Index (MI) 값은 0.1-0.3 구간이다. 이는 일반적인 B-mode 초음파의 MI 값보다 낮은 값으로 조직에서 발생하는 선형 반사파를 최소화 하고, 미세기포의 파괴를 최소화 하기 위함이다. 반대로 너무 낮은 MI값을 사용하게 되면, 미세기포가 선형 진동을 보이게 되므로 적합하지 않다 (6). 일반적으로 초음파 기계 및 프로그램에서 사용하는 매개 변수 값에 따라 다르지만, 부드러운 외피로 이루어진 소노뷰는 주로 0.1 근처 MI 값을 사용하고, 비교적 경도가 높은 외피로 구성된 소나조이드는 0.15-0.2 정도의 MI값을 사용한다 (7).

초음파 조영제

간에 사용되는 초음파 조영제는 크게 두 종류로, 순수혈관조영제 (pure-vascular agent)와 Kupffer 조영제 (Kupffer agent)로 나뉜다. 순수 혈관 조영제 중 현재 전 세계적으로 가장 널리 쓰이는 초음파 조영제는 소노뷰 (SonoVue, Bracco)이다. 인지질 (phospholipid) 외피 내에 Sulfur Hexafluoride 가스를 포함하고 있다. 소노뷰의 직경은 1.5-2.5 ㎛로 적혈구와 비슷한 크기로 CT 혹은 MR 조영제보다 크고, 혈관 내피 (vascular endothelium)를 통과하지 못하여 세포 간질로의 조영제 이동이 없어, 순수한 혈관 영상을 생성한다 (7). 조영증강초음파 검사에서 간의 동문맥단락 (AP shunt) 같은 혈관가양성병변 (vascular pseudolesion)을 보이지 않는 것도 같은 이유에서이다.

Kupffer 조영제는 소나조이드 (Sonazoid, GE healthcare)가 대표적이며, 한국, 일본, 중국, 대만, 노르웨이에서 사용된다. 인지질 외피 내에 Perfluorobutane 가스를 포함하고 있다. 소나조이드의 직경은 2.1-2.9 ㎛로 소노뷰와 마찬가지로 혈관 내피를 통과하지 못하여 혈관 영상을 생성함과 동시에, 간 내 대식세포인 Kupffer 세포에 포식되어 간 실질에 수 십 분간 이상 지속되는 echogenicity를 나타내는 특징을 가지고 있다. Yanagisawa 등 (8)의 *In vitro* 실험에 따르자면 소나조이드 주입 후 1분 경과 후 Kupffer 세포가 위족 (pseudopodia)을 만들어 소나조이드 bubble을 둘러싸고, 5분 경과 후 소나조이드가 포식된 것을 관찰하여 보고한 바 있다. 따라서 소나조이드를 이용한 조영증강초음파 영상은, 혈관기 (vascular phase) 이후 Kupffer 세포 포식에 의해 echogenicity를 보이는 Kupffer기 (Kupffer phase)가 있으며, 통상 조영제 주입 후 10분 이후의 시기를 의미한다 (9).

조영증강초음파 검사 방법

조영제 종류에 상관없이 검사법은 유사하다. 준비물은 초음파 조영제, 생리식염수, 5 mL 및 10 mL 주사기, 조영제 주입을 도와줄 의료진 1인, 피검사자의 IV line이다. 조영제 제조사의 권고사항에 따라 조영제 용매와 용질을 혼합한다. 피검사자의 체중에 맞추어 적정 조영제양을 주사기 담고, 10 mL 주사기에 생리식염수를 담아 준비한다. B-mode 초음파로 대상 병변을 확인하고, 피검사자의 IV line을 확인한다. 이 때 IV line의 카테터와 약물 주입구가 너무 가까운 것은 되도록 피하는 것이 좋다. 피검사자는 안정된 상태에서 되도록 얕은 숨을 쉴 수 있도록 안내한다. 초음파 기계의 프로그램을 조영증강초음파 모드로 변경한 후, 대상 병변 관찰에 적합한 위치에 초음파 probe를 위치하고, 조영제 주입을 담당한 의료진이 IV line에 조영제를 채운다. 이후 생리식염수 10 mL를 빠르게 주입하며 (flushing), 이와 동시에 초음파 기계 패널의 timer를 시작한다. 처음 60-70초 간은 동영상으로 영상을 저장하며, 이후에는 15-30초 정도의 간격으로 간헐적 스캔을 한다. 순수혈관조영제의 경우 조영제가 대부분 파괴되는 5분까지 검사를 시행하며, Kupffer 조영제의 경우 Kupffer기 확인을 위해 10분 이후까지 검사를 시행한다.

조영증강초음파의 간세포암의 진단

(1) 순수혈관조영제를 이용한 간세포암 진단

CT, MRI와 마찬가지로 조영증강초음파 또한 간세포암 고위험군에서 특징적인 영상 소견을 바탕으로 간세포암을 비침습적으로 진단할 수 있다 (10). 2017년 American

College of Radiology에서 발표한 조영증강초음파 Liver Imaging Reporting and Data System (LI-RADS)에 따르면, 간세포암 고위험군에서 동맥기 조영증강 (arterial phase hyperenhancement, APHE)을 동반한 1 cm 이상의 결절에서 60초 이후에서 보이는 경도 (mild)의 씻김 (washout)이 있을 경우 LR-5 (definitely HCC) category로 분류하며 비침습적 간세포암 진단이 가능하다 (Fig. 1). 씻김의 정도 (degree)는 초음파 조영제 주입 2분에 평가한다.

초창기 조영증강초음파 연구들에서 간경화 환자에서 발생한 간내담도암의 50%가 동맥기 조영증강 및 씻김을 보여 간세포암으로 오진될 가능성이 높음을 보고한 바 있고, 이는 과거 간세포암 진단에 조영증강초음파가 활발히 사용되지 않은 이유 중 하나이다 (11, 12). 그러나 이후 연구에서 대부분의 간내담도암은 간세포암과 달리 동맥기에서 가장자리 주변으로 동맥기 조영증강이 보이거나 (rim APHE), 씻김이 조기에 일어나거나 (조영제 주입 후 60초 이전), 타공한 것 같은 (punched-out) 높은 강도의 씻김 (marked washout)이 보이는 것이 밝혀졌고, 이를 LR-M category (malignancy other than HCC)로 분

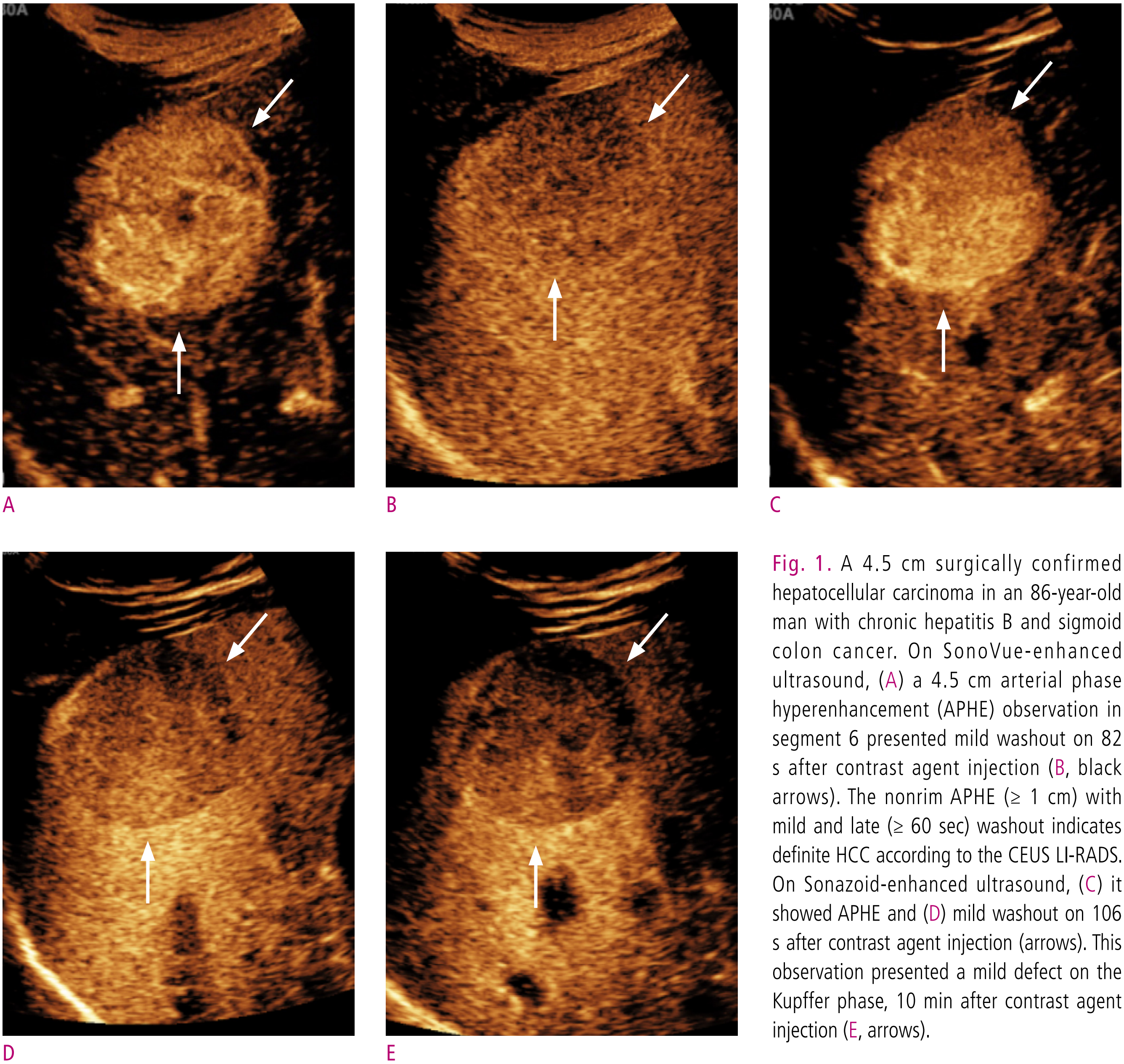

Fig. 1. A 4.5 cm surgically confirmed hepatocellular carcinoma in an 86-year-old man with chronic hepatitis B and sigmoid colon cancer. On SonoVue-enhanced ultrasound, (A) a 4.5 cm arterial phase hyperenhancement (APHE) observation in segment 6 presented mild washout on 82 s after contrast agent injection (B, black arrows). The nonrim APHE (≥ 1 cm) with mild and late (≥ 60 sec) washout indicates definite HCC according to the CEUS LI-RADS. On Sonazoid-enhanced ultrasound, (C) it showed APHE and (D) mild washout on 106 s after contrast agent injection (arrows). This observation presented a mild defect on the Kupffer phase, 10 min after contrast agent injection (E, arrows).

류하면서, 동맥기 조영증강 패턴 및 씻김의 시간과 강도를 반영한 현재의 간세포암 진단기준이 자리잡게 되었다 (13-15) (Fig. 2). 아울러 가장 흔한 고혈관성 병변 중 하나인 hemangioma의 경우 CT, MRI 소견과 유사하게 동맥기에서 peripheral globular enhancement pattern 및 구심성 조영증강을 보일 경우 혈관종으로 간주할 수 있고 (Fig. 3), 조영증강초음파 LI-RADS에서는 위 소견을 보일 경우 LR-1 (definitely benign)로 분류한다.

Terzi 등 (16)의 연구에 따르면 1006개의 고위험 결절에 대해 조영증강초음파 LI-RADS를 적용하였을 경우, LR-5 (definitely HCC)는 98.5%의 양성예측도 (positive predictive value)를 보였다. 간내담도암이 LR-5 category로 분류된 경우는 없었다. 대신 LR-M (probably or definitely malignancy but not HCC specific)의 경우 44%가 간세포암, 56%가 간세포암 이외의 악성종양이었다. 이 진단기준은 간세포암 진단에 특이도가 높은 것이 특징이며 (17), European Association for the Study of the Liver (EASL) 및 Korean Liver Cancer Association (KLCA)-National Cancer Center (NCC) 가이드라인에서도 동일 진단기준을 사용한다 (18, 19). 다만 이 진단 기

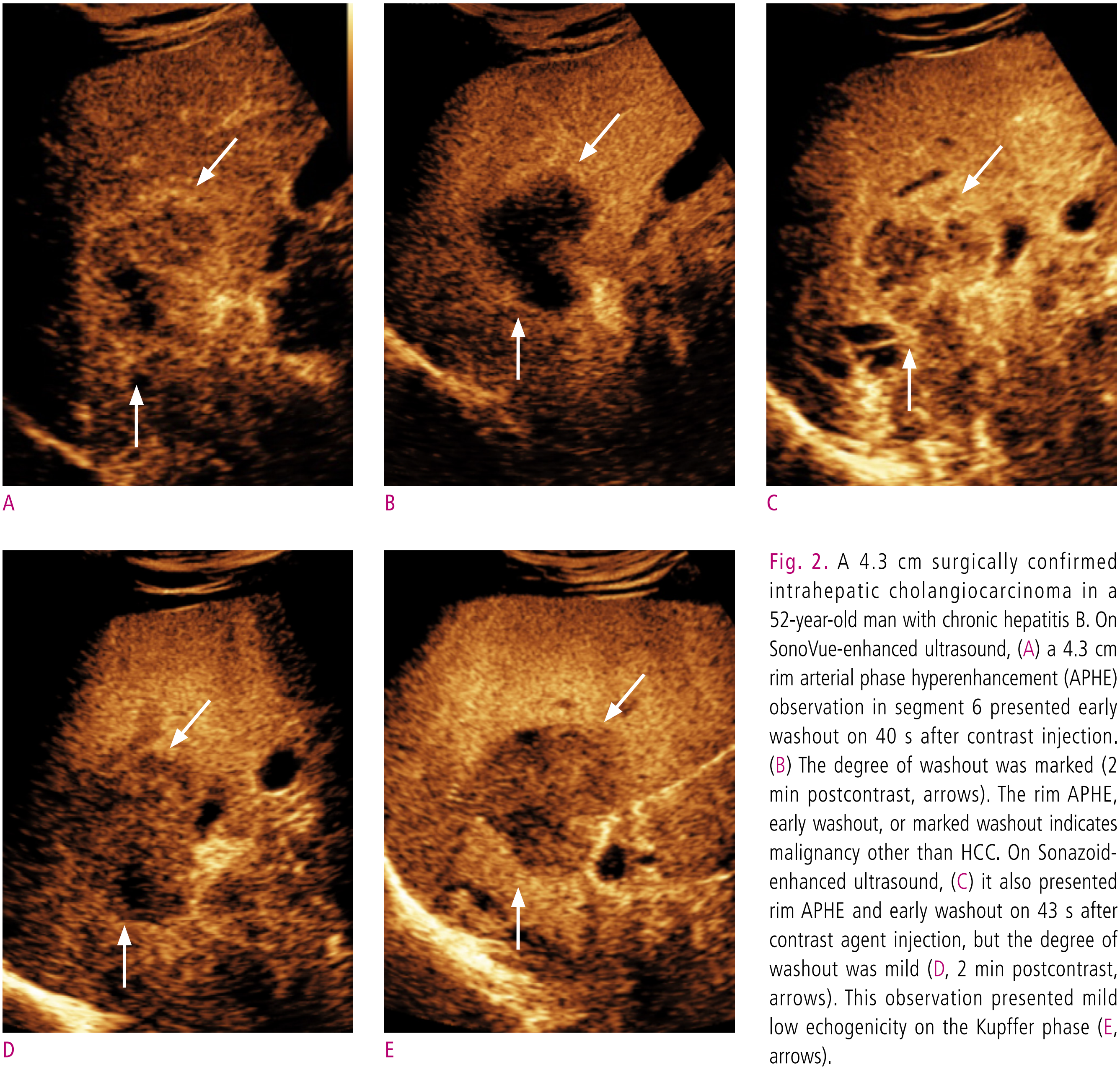

Fig. 2. A 4.3 cm surgically confirmed intrahepatic cholangiocarcinoma in a 52-year-old man with chronic hepatitis B. On SonoVue-enhanced ultrasound, (A) a 4.3 cm rim arterial phase hyperenhancement (APHE) observation in segment 6 presented early washout on 40 s after contrast injection. (B) The degree of washout was marked (2 min postcontrast, arrows). The rim APHE, early washout, or marked washout indicates malignancy other than HCC. On Sonazoid-enhanced ultrasound, (C) it also presented rim APHE and early washout on 43 s after contrast agent injection, but the degree of washout was mild (D, 2 min postcontrast, arrows). This observation presented mild low echogenicity on the Kupffer phase (E, arrows).

준은 순수혈관조영제 기준이다.

(2) Kupffer제를 이용한 간세포암 진단

소나조이드 조영증강 초음파의 간세포암 동맥기 영상소견은 소노뷰와 유사하다. 43개의 간세포암을 대상으로 두 조영제의 혈관기 영상소견을 비교한 연구에서, 동맥기 조영증강 패턴은 100% 일치하였다. 그러나 씻김이 처음 확인되는 시간과 씻김 정도에는 두 조영제 간 차이를 보였다 (17). 이는 동맥기 이후부터 Kupffer 세포의 소나조이드 포식이 영상에 영향을 미칠 가능성을 의미하기도 한다.

간세포암을 포함한 일부 종양에서 Kupffer 세포의 수의 감소로 Kupffer기에서 낮은 echogenicity를 보인다 (Figs.

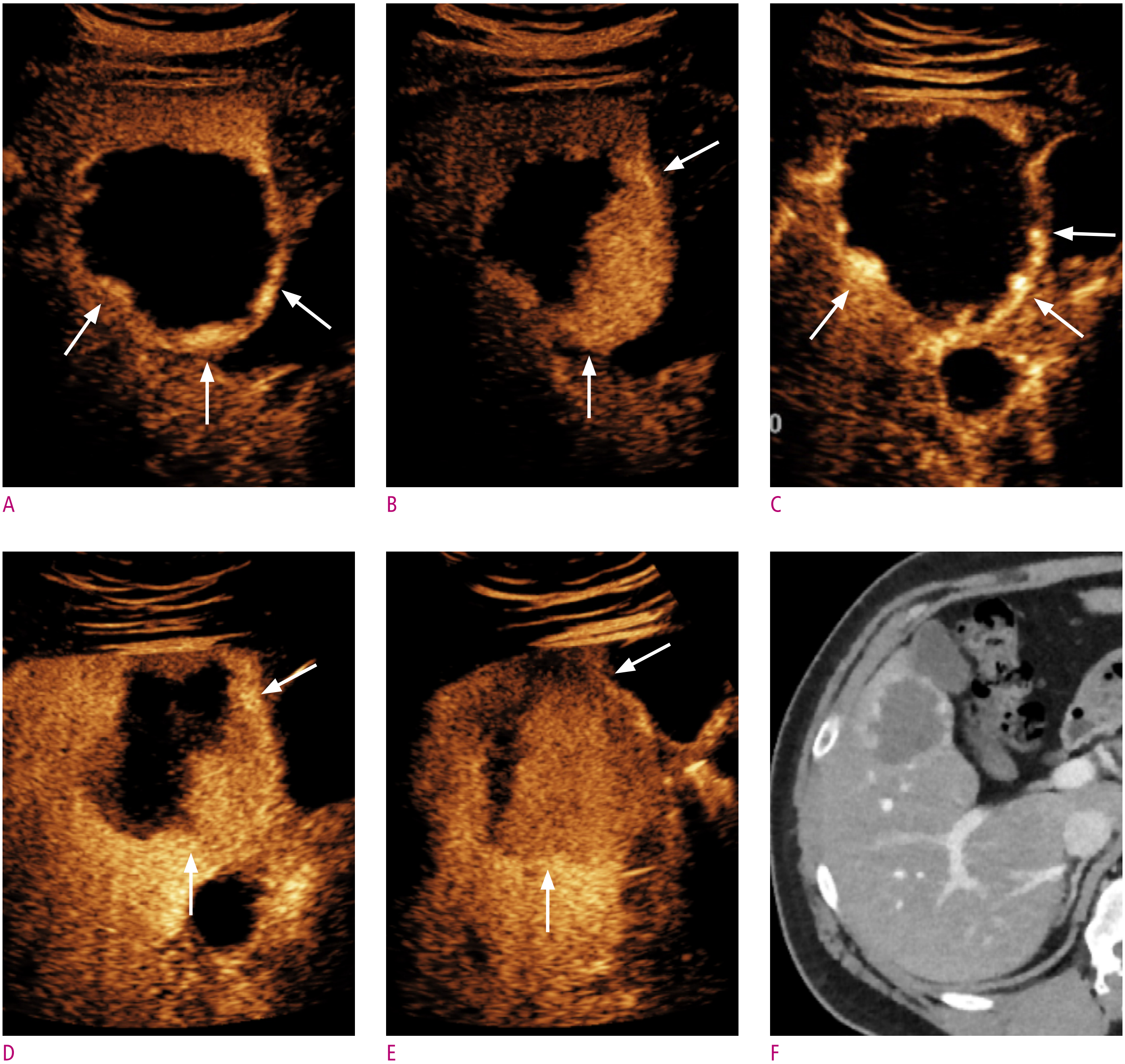

Fig. 3. A 5 cm typical hemangioma in a 44-year-old man with non-alcoholic steatohepatitis. On SonoVue-enhanced ultrasound, (A) a 5 cm peripheral globular enhancing observation in segment 5 was noted (arrows). (B) This observation showed centripetal enhancement in the vascular phase (arrows). On Sonazoid-enhanced ultrasound, this observation also showed peripheral globular enhancement in (C) arterial phase and (D) centripetal enhancement in vascular phase (arrows). On (E) Kupffer phase, this lesion presented mild low echogenicity (arrows). On (F) CT exam, the peripheral globular enhancement was also noted (arrows).

1-3). 이러한 특징으로 소나조이드 조영증강 초음파 검사가 간세포암 발견에 높은 민감도를 보이는 것으로 보고된 바 있다 (20, 21). Japan Society of Hepatology 가이드라인에 따르면 (22), MRI에서 동맥기 조영증강을 보이지 않은 결절의 2차 진단 검사로서 소나조이드를 사용할 때 동맥기 조영증강 혹은 Kupffer기의 낮은 echogenicity를 보이면 간세포암으로 진달할 수 있다. 그러나 Kang 등 (17)의 간세포암 고위험군 환자를 대상으로 한 연구에서 10개의 간세포암 이외의 악성종양 중 3개의 병변에서 동맥기 조영증강 및 Kupffer기의 낮은 echogenicity를 보였다. 또한 Sugimoto 등 (23)의 연구에 따르면, 73.9% (36/46)의 혈관종에서 Kupffer기의 낮은 echogenicity를 보였다. 가도제틱산 (Gadoxetic acid, Primovist, Bayer)를 이용한 간 MRI 검사에서, 간담도기 (hepatobiliary phase)에서 간세포암 이외의 국소 결절도 낮은 signal intensity를 보이는 원리와 같다 (24). 이는 Kupffer기의 낮은 echogenicity가 간세포암에 특이적인 소견이 아님을 반증한다. 한편 Hwang 등 (21)의 최근 연구에 따르면, Kupffer기의 낮은 echogenicity를 씻김의 대안으로 가정하였을 경우, 그렇지 않은 경우와 비교하여 특이도(63.6% vs. 69.7%, P = 0.5)에 통계적으로 유의미한 변화 없이 민감도(83.2% vs. 74.2%, P = 0.008)의 상승을 보이는 것으로 보고하였다. Inoue 등 (25)의 연구에서는 이형성결절과 초기 간세포암을 감별할 때, 두 병변 모두 Kupffer기에서 낮은 echogenicity를 보이는 경우가 흔하지 않지만, Kupffer기에서 낮은 echogenicity를 보이면 초기 간세포암으로 진단할 수 있음을 보고한 바 있다.

소나조이드를 이용한 조영증강 초음파 검사의 또 다른 고려점은, Kupffer세포의 조영제 포식으로 인한 가성씻김효과 (pseudowashout effect)와 이로 인한 위양성 (false-positive)이다 (24). 가도제틱산을 이용한 간 MRI 검사에서, 이행기 (transition phase)에 보이는 낮은 signal intensity를 씻김으로 인정하지 않는 이유와 같다. Kupffer 세포의 소나조이드 포식이 어느 시점부터 영상에 유의미한 영향을 미치는지에 대한 기준은 아직 더 많은 연구와 논의가 필요하다. 최근 Kang 등 (26)의 연구에 따르면, 소나조이드 주입 후 씻김을 평가하는 시기를 1분에서 10분까지 1분 간격으로 나누어 간세포암 진단능을 비교하였을 때, 조영제 주입 후 6분까지 씻김을 평가하였을 때 특이도의 유의미한 변화 없이 민감도의 상승을 보고한 바 있다.

(3) 초음파 조영제에 따른 진단능 비교

소노뷰와 소나조이드 조영증강 초음파의 간세포암 진단능을 비교하였을 때, Kang 등 (17)의 대상자내 (intraindivisual) 연구에 따르면, 고위험 군에서 소나조이드를 이용한 간세포암 진단시 소노뷰와 같은 진단기준 - 동맥기 조영증강 (≥ 1 cm) 및 60초 이후에서 보이는 경도의 씻김 (mild washout) - 을 적용하였을 경우, 특이도의 유의한 차이 없이 소나조이드가 더 높은 민감도를 보였다 (Figs. 1-3). 해당 논문에서, 간세포암의 동맥기 조영증강 패턴에는 유의미한 차이는 없었으나 소나조이드를 이용하였을 경우 소노뷰의 경우보다 평균적으로 씻김이 조금 더 늦게 관찰되며 (중위값, 101 ± 11초 vs. 84 ± 5초) 이로 인해 조기 씻김 (early washout) 현상이 소노뷰보다 낮은 빈도로 관찰되는 것이 진단능의 차이를 보이는 이유로 기술한 바 있다. Lv 등 (27)의 연구에서는 B-mode 초음파 검사에 조영증강초음파를 추가로 수행하였을 경우에 보이는 정확도 차이를 두 조영제 간 비교하였고, 3명의 판독자가 각각 평가하였을 시, 소나조이드를 사용하였을 경우 각각 17%, 20%, 16%의 정확도 향상을 보여 19%, 16%, 20%의 정확도 향상을 보였던 소노뷰와 비교시 비열등함을 보여주었다 (비열등성 한계: - 20%).

(4) CT 및 MRI와 진단능 비교

전술한 바와 같이 CT, MRI 조영제와 초음파 조영제는 생체학적 특징이 다를 뿐 아니라, 검사를 수행하는 기술적 측면에서도 차이가 있다. 조영증강초음파는 초음파 창의 제한이 있으므로, 미리 정해진 대상 병변에 대해서만 평가가 가능하고, CT 및 MRI에 비해서 병변의 위치나 환자 요소, 검사자의 숙련도에 의한 영향을 많이 받아 제한적인 검사가 되는 경우가 더 빈번하다. 실제 여러 연구에서 조영증강초음파 검사의 간세포암 진단 민감도는 40-65%로 CT (65-75%)나 MRI (70.6%-90%) 검사에 비해 낮다 (24, 28-30). 그러나 조영증강초음파는 특이도가 높은 검사로 (91.5-100%) (29, 30), 간질로의 조영제 이동이 없어 동문맥단락 같은 혈관가성병변이 없으며, 혈역학적 정보를 연속적으로 확인 가능한 것이 장점이다.

(5) 2차 영상 검사로써의 조영증강초음파의 역할

EASL 및 KLCA-NCC 가이드라인에 따르면, 조영증강초음파는 CT 혹은 MRI 검사에서 대상 병변이 간세포암의 영상 진단기준을 만족하지 못할 경우, 2차 검사로써 조영증강초음파를 고려해 볼 수 있다 (18, 19, 29, 31). 조영증강초음파는 혈역학적 정보를 실시간으로 평가할 수 있어 CT 혹은 MRI 검사에서 실제 동맥기 및 문맥기와 영상획득 시각의 차이로 발생하는 오류를 최소화 할 수 있다. 최근 한 연구에서는 CT, MRI 검사에서 동맥기 조영증강을 보이지 않는 국소 간병변에 조영증강초음파를 시행하였을 경우 43개 중 12개의 병변 (27.9%)에서 새롭게 동맥기 조영증강

이 확인된 것을 보고한 바 있다 (32). Aube 등 (30)의 연구에 따르자면, EASL 가이드라인을 적용하였을 경우, 10-20 mm 크기의 병변에서 MRI 검사 혹은 CT 검사 단독 보다, 조영증강초음파를 2차 검사로 사용하였을 경우, 유의한 민감도 (61.1% vs. 83.4%) 및 특이도 (55.6% vs. 76.8%)의 상승을 보였다 (Figs. 4 and 5). MRI 검사 후 2차 검사로 CT와 조영증강초음파를 비교하였을 때 민감도(44.2% vs. 34.6%, P = 0.36)에 유의한 차이를 보이지 않았고 CT검사보다 높은 특이도 (74.5% vs. 90.2%, P = 0.01)를 보였다. Kang 등 (29)의 연구에서도, 위 가이드라인에 따라 소노뷰를 이용한 조영증강초음파를 2차 검사로 시행하였을 경우, 간 MRI 단독 검사보다 가이드라인의 HCC 민감도 (EASL, 72.2% vs. 83.5%; KLCA-NCC 86.1% vs. 91.1%)가 특이도의 변화 없이 유의하게 상승한 것을 보고하였다.

결 론

이 논문은 조영증강초음파의 원리와 특징, 간세포암 진단 알고리즘의 적용대하여 최신 지견을 바탕으로 대표적인 영상 예시들과 함께 설명하였다. 초음파 조영제는 순수혈

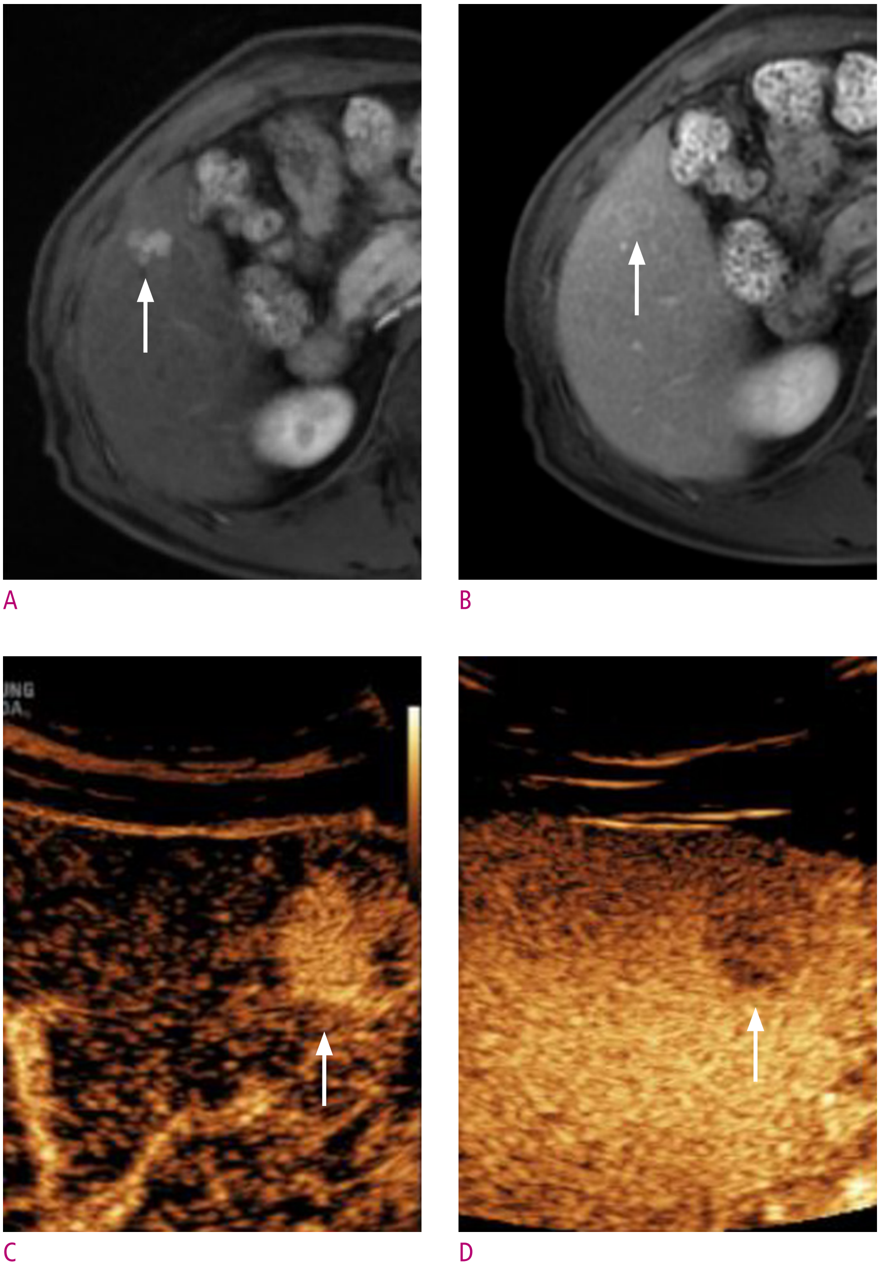

Fig. 4. A 61-year-old man with chronic hepatitis B. On Gadoxetic acid-enhanced MRI, (A) a 1.7 cm arterial phase hyperenhancement (APHE) observation (arrow) in segment 6 did not present washout in (B) portal venous phase (arrow). On SonoVue-enhanced ultrasound, (C) a 1.7 cm APHE observation (arrow) presented mild washout on 252 s after contrast agent injection (D, arrows). This lesion was pathologically confirmed as hepatocellular carcinoma.

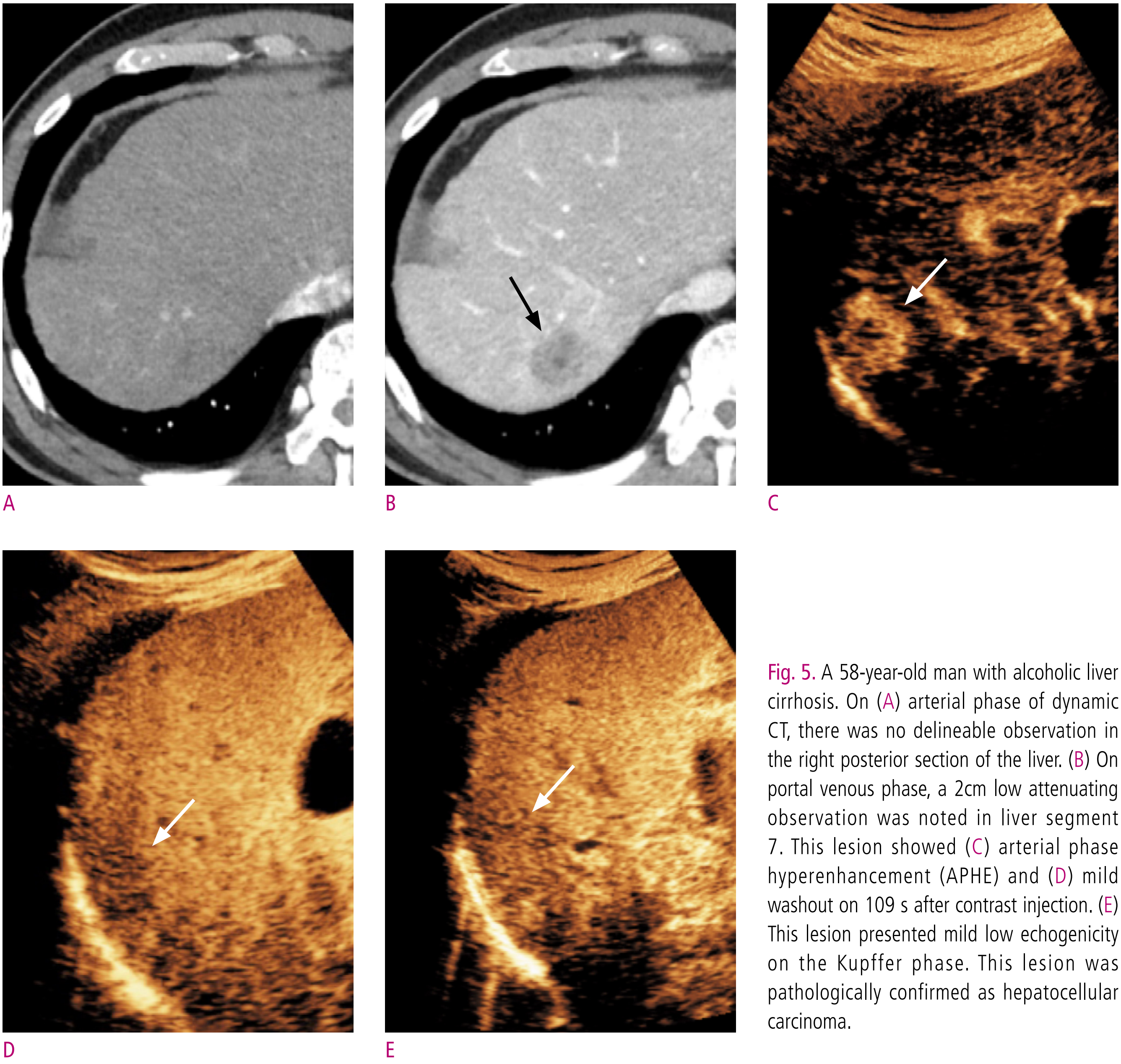

Fig. 5. A 58-year-old man with alcoholic liver cirrhosis. On (A) arterial phase of dynamic CT, there was no delineable observation in the right posterior section of the liver. (B) On portal venous phase, a 2cm low attenuating observation was noted in liver segment 7. This lesion showed (C) arterial phase hyperenhancement (APHE) and (D) mild washout on 109 s after contrast injection. (E) This lesion presented mild low echogenicity on the Kupffer phase. This lesion was pathologically confirmed as hepatocellular carcinoma.

관조영제와 Kupffer 조영제가 있다. 조영증강 초음파 검사는 신독성 및 방사선 노출이 없는 검사로 CT, MRI 검사에 비해 민감도는 낮지만 특이도가 높은 검사이며, 간세포암 진단 알고리즘에서 2차 검사로서의 역할이 기대된다.

References

1. Dietrich CF, Nolsøe CP, Barr RG, Berzigotti A, Burns PN, Cantisani V, et al. Guidelines and good clinical practice recommendations for contrast enhanced ultrasound (CEUS) in the liver–update 2020–WFUMB in cooperation with EFSUMB, AFSUMB, AIUM, and FLAUS. Ultraschall in der Medizin-European Journal of Ultrasound 2020;41:562-585.
2. Yusuf GT, Sellars ME, Deganello A, Cosgrove DO, Sidhu PS. Retrospective analysis of the safety and cost implications of pediatric contrast-enhanced ultrasound at a single center. American Journal of Roentgenology 2017;208:446-452.
3. Schwarze V, Marschner C, de Figueiredo GN, Rübenthaler J, Clevert D-A. Single-center study: evaluating the diagnostic performance and safety of contrast-enhanced ultrasound

(CEUS) in pregnant women to assess hepatic lesions. Ultraschall in der Medizin-European Journal of Ultrasound 2020;41:29-35.

4. Köse G, Darguzyte M, Kiessling F. Molecular ultrasound imaging. Nanomaterials 2020;10:1935.
5. Minami Y, Kudo M. Contrast-enhanced ultrasonography with Sonazoid in hepatocellular carcinoma diagnosis. Hepatoma Research 2020;6:46.
6. Greco A, Mancini M, Gargiulo S, Gramanzini M, Claudio P, Brunetti A, et al. Ultrasound biomicroscopy in small animal research: applications in molecular and preclinical imaging. Journal of Biomedicine and Biotechnology 2012;2012.
7. Barr RG, Huang P, Luo Y, Xie X, Zheng R, Yan K, et al. Contrast-enhanced ultrasound imaging of the liver: a review of the clinical evidence for SonoVue and Sonazoid. Abdominal Radiology 2020;45:3779-3788.
8. Yanagisawa K, Moriyasu F, Miyahara T, Yuki M, Iijima H. Phagocytosis of ultrasound contrast agent microbubbles by Kupffer cells. Ultrasound in medicine & biology 2007;33:318-325.
9. Lee JY, Minami Y, Choi BI, Lee WJ, Chou Y-H, Jeong WK, et al. The AFSUMB consensus statements and recommendations for the clinical practice of contrast-enhanced ultrasound using sonazoid. Journal of Medical Ultrasound 2020;28:59.
10. Quaia E. State of the Art: LI-RADS for Contrast-enhanced US. Radiology 2019;293:4-14.
11. Li R, Zhang X, Ma K-S, Li X-W, Xia F, Zhong H, et al. Dynamic enhancing vascular pattern of intrahepatic peripheral cholangiocarcinoma on contrast-enhanced ultrasound: the influence of chronic hepatitis and cirrhosis. Abdominal imaging 2013;38:112-119.
12. Vilana R, Forner A, Bianchi L, García-Criado Á, Rimola J, Rodríguez de Lope C, et al. Intrahepatic peripheral cholangiocarcinoma in cirrhosis patients may display a vascular pattern similar to hepatocellular carcinoma on contrast-enhanced ultrasound. Hepatology 2010;51:2020-2029.
13. Wildner D, Bernatik T, Greis C, Seitz K, Neurath M, Strobel D. CEUS in hepatocellular carcinoma and intrahepatic cholangiocellular carcinoma in 320 patients–early or late washout matters: a subanalysis of the DEGUM multicenter trial. Ultraschall in der Medizin-European Journal of Ultrasound 2015;36:132-139.
14. Wildner D, Pfeifer L, Goertz R, Bernatik T, Sturm J, Neurath M, et al. Dynamic contrast-enhanced ultrasound (DCE-US) for the characterization of hepatocellular carcinoma and cholangiocellular carcinoma. Ultraschall in der Medizin-European Journal of Ultrasound 2014;35:522-527.
15. Chen L-D, Xu H-X, Xie X-Y, Xie X-H, Xu Z-F, Liu G-J, et al. Intrahepatic cholangiocarcinoma and hepatocellular carcinoma: differential diagnosis with contrast-enhanced ultrasound. European radiology 2010;20:743-753.
16. Terzi E, Iavarone M, Pompili M, Veronese L, Cabibbo G, Fraquelli M, et al. Contrast ultrasound LI-RADS LR-5 identifies hepatocellular carcinoma in cirrhosis in a multicenter restropective study of 1,006 nodules. Journal of hepatology 2018;68:485-492.
17. Kang H-J, Lee JM, Yoon JH, Lee K, Kim H, Han JK. Contrast-enhanced US with sulfur hexafluoride and perfluorobutane for the diagnosis of hepatocellular carcinoma in individuals with high risk. Radiology 2020;297:108-116.
18. Association KLC. 2018 Korean Liver Cancer Association–National Cancer Center Korea practice guidelines for the management of hepatocellular carcinoma. Korean Journal of Radiology 2019;20:1042.
19. Liver EAFTSOT. EASL clinical practice guidelines: management of hepatocellular carcinoma. Journal of hepatology 2018;69:182-236.
20. Hatanaka K, Kudo M, Minami Y, Ueda T, Tatsumi C, Kitai S, et al. Differential diagnosis of hepatic tumors: value of contrast-enhanced harmonic sonography using the newly developed contrast agent, Sonazoid. Intervirology 2008;51:61-69.
21. Hwang JA, Jeong WK, Min JH, Kim Y-Y, Heo NH, Lim HK. Sonazoid-enhanced ultrasonography: comparison with CT/MRI Liver Imaging Reporting and Data System in patients with suspected hepatocellular carcinoma. Ultrasonography 2021;40:486.
22. Kudo M, Matsui O, Izumi N, Iijima H, Kadoya M, Imai Y, et al. JSH consensus-based clinical practice guidelines for the management of hepatocellular carcinoma: 2014 update by the Liver Cancer Study Group of Japan. Liver cancer 2014;3:458-468.
23. Sugimoto K, Moriyasu F, Saito K, Yoshiara H, Imai Y. Kupffer-phase findings of hepatic hemangiomas in contrast-enhanced ultrasound with sonazoid. Ultrasound in medicine & biology 2014;40:1089-1095.
24. Joo I, Lee JM, Lee DH, Jeon JH, Han JK. Retrospective validation of a new diagnostic criterion for hepatocellular carcinoma on gadoxetic acid-enhanced MRI: can hypointensity on the hepatobiliary phase be used as an

alternative to washout with the aid of ancillary features? European radiology 2019;29:1724-1732.

25. Inoue T, Hyodo T, Korenaga K, Murakami T, Imai Y, Higaki A, et al. Kupffer phase image of Sonazoid-enhanced US is useful in predicting a hypervascularization of non-hypervascular hypointense hepatic lesions detected on Gd-EOB-DTPA-enhanced MRI: a multicenter retrospective study. Journal of gastroenterology 2016;51:144-152.
26. Kang H-J, Kim JH, Yoo J, Han JK. Diagnostic criteria of perfluorobutane-enhanced ultrasonography for diagnosing hepatocellular carcinoma in high-risk individuals: how is late washout determined? Ultrasonography (Seoul, Korea).
27. Lv K, Zhai H, Jiang Y, Liang P, Xu H-X, Du L, et al. Prospective assessment of diagnostic efficacy and safety of SonazoidTM and SonoVue® ultrasound contrast agents in patients with focal liver lesions. Abdominal Radiology 2021;46:4647-4659.
28. Lee YJ, Lee JM, Lee JS, Lee HY, Park BH, Kim YH, et al. Hepatocellular carcinoma: diagnostic performance of multidetector CT and MR imaging—a systematic review and meta-analysis. Radiology 2015;275:97-109.
29. Kang H-J, Lee JM, Yoon JH, Han JK. Role of contrast-enhanced ultrasound as a second-line diagnostic modality in noninvasive diagnostic algorithms for hepatocellular carcinoma. Korean journal of radiology 2021;22:354.
30. Aubé C, Oberti F, Lonjon J, Pageaux G, Seror O, N'Kontchou G, et al. EASL and AASLD recommendations for the diagnosis of HCC to the test of daily practice. Liver International 2017;37:1515-1525.
31. Tan Z, Teoh WC, Wong KM, Wansaicheong GK-L, Sandrasegaran K. Analysis of comparative performance of CEUS and CECT/MR LI-RADS classification: Can CEUS dichotomize LI-RADS indeterminate lesions on CT or MRI? Clinical imaging 2020;62:63-68.
32. Kang H-J, Kim JH, Joo I, Han JK. Additional value of contrast-enhanced ultrasound (CEUS) on arterial phase non-hyperenhancement observations (≥ 2 cm) of CT/MRI for high-risk patients: focusing on the CT/MRI LI-RADS categories LR-3 and LR-4. Abdominal Radiology 2020;45:55-63.

조영증강초음파의 원리와 간세포암 진단

강효진[1,2], **이재영**[1,2], **이정민**[1,2]

[1]서울대학교병원 영상의학과
[2]서울대학교 의과대학 의학과

초 록

조영증강초음파 (contrast-enhanced ultrasound)는 미세기포 조영제를 이용하여 초음파로 대상체의 조영증강을 확인하는 검사이다. 신독성이나 방사선 노출 위험 없어 초음파 창이 확보 된다면 여러 장기에 적용해 볼 수 있고, 복부 장기 중에서는 간 및 간 병변을 평가하는데 유용하다. 이 종설에서는 조영증강초음파를 이용한 간 병변의 정확한 진단 및 적절한 임상적용을 위해 조영증강초음파의 최신 지식을 제공하고자 하였다. 조영증강초음파의 원리, 두 종류의 초음파 조영제 (순수혈관조영제와 Kupffer제)의 비교, 간세포암의 진단기준 및 진단 알고리즘에서의 역할을 다루고자 한다.

www.e-kjar.org
https://doi.org/10.52668/kjar.2022.00143

pISSN 2586-1719 / eISSN 2799-3299
Copyright © The Korean Society of Abdominal Radiology

Korean J Abdom Radiol 2022;6:22-36

Review Article

Friend or Foe: How to Suppress and Measure Fat During Abdominal Resonance Imaging?

Hokun Kim[1], Joon-Il Choi[1,2], Hyun-Soo Lee[3]

[1]*Department of Radiology, Seoul St. Mary's Hospital, College of Medicine, The Catholic University of Korea, Seoul, Korea*
[2]*Catholic Cancer Research Institute, College of Medicine, The Catholic University of Korea, Seoul, Korea*
[3]*Siemens Healthineers Ltd, Seoul, Korea*

The suppression of fat signals in abdominal magnetic resonance imaging has become a basic and routine practice in the diagnosis of pathologic conditions of abdominal organs in clinical settings. Many fat-suppression techniques have been developed in the past several decades, with fat-quantification methods introduced in response in more recent years. Fat-suppression techniques can be divided into two categories. Chemical shift-based techniques include chemical shift selective (CHESS), water excitation, and the Dixon method. CHESS is the most commonly used fat-suppression method, nulling the fat signal using a fat-selective radiofrequency pulse with a spoiler gradient. Water excitation employs a binomial pulse that excites only the water protons. Finally, the Dixon method involves using the in-phase/out-of-phase cycling of fat and water. An inversion-based technique, known as short tau inversion recovery (STIR), uses a pre-excitation inversion pulse that inverts the spin of all tissues. By selecting the appropriate MRI inversion time such that the longitudinal magnetization of fat is zero, fat protons will not contribute to the MRI signal. Also, spectral attenuated inversion recovery (SPAIR) is a hybrid technique that combines the characteristics of both CHESS and STIR. The most precise fat-quantification technique known to date is a complex-based multipoint Dixon method, with which the proton-density fat fraction (PDFF) can be obtained. Multiple confounding factors must be well-corrected for accurate fat quantification. Radiologists should be familiar with the various fat suppression and measurement methods during MRI and be able to apply them to enhance patient care.

Keywords: Magnetic resonance imaging; Steatosis; Liver

Introduction

Fat-suppression techniques are currently essential in almost all abdominal MRI examinations. The indication for fat-suppressed MRI images can be summarized in terms of three purposes. First, it is possible to significantly reduce chemical shift artifacts that have been increased as high magnetic field strength (3.0 Tesla or higher) instruments become increasingly common. It is also very useful for the visualization of contrast agents in soft tissues containing

Received: March 24, 2022 **Accepted:** April 19, 2022
Correspondence: Joon-Il Choi, MD, PhD
Department of Radiology, Seoul St. Mary's Hospital, School of Medicine, The Catholic University of Korea, 222 Banpo-daero, Seocho-gu, Seoul 06591, Korea
Tel: +82-2-2258-1431 Fax: +82-2-599-6771 E-mail: dumkycji@gmail.com
This is an Open Access article distributed under the terms of the Creative Commons Attribution Non-Commercial License (http://creativecommons.org/licenses/by-nc/4.0/) which permits unrestricted non-commercial use, distribution, and reproduction in any medium, provided the original work is properly cited.

adipose cells on contrast-enhanced MRI sequences. TP [The presence of fat components is often an important clue in the diagnosis of various pathological conditions in the abdomen and pelvis. Fat-suppressed MRI imaging is thus a valuable tool that can detect intracytoplasmic fat in tissues more sensitively as compared with other modalities such as computed tomography or ultrasound (1).] This is of great help in discriminating liver tumors and diagnosing hepatic steatosis; tumors of the adrenal gland, kidney, or retroperitoneal space; tumors of the ovary; and several hematologic diseases manifesting bone-marrow infiltrations. Lastly, certain fat-suppression techniques can be used to quantify fat, which is especially useful in noninvasive diagnosis and tracking the treatment effectiveness of hepatic steatosis (2). The article briefly reviews the basic physics needed to understand fat-suppression techniques, explains the background principles inherent with characteristics of several frequently used fat-suppression techniques, and reports a state-of-the-art fat quantification technique using a multipoint Dixon method.

Basic physics

One important cause of why fat and water display fundamentally different behaviors in response to an external magnetic field (e.g., MRI magnet) is that water and fat protons experience different local magnetic environments due to their different molecular structures. Fat protons within multiple long-chain triglycerides are located around electroneutral carbon atoms. This fact allows the electron cloud surrounding these protons to shield them from the full gyromagnetic effect of the external magnetic field, which means that the protons in the fat encounter a slightly weaker local magnetic field and have a relatively lower resonance frequency. On the other hand, the protons of water molecules are located around strong electronegative oxygen atoms, which forcefully pull the electron cloud covering the protons of the water molecules toward them, reducing its capacity to shield them from the gyromagnetic effect of an external magnetic field. This phenomenon is known as the deshielding effect. CME 1c [As a consequence, water protons have a relatively higher resonance frequency than that of fat protons, and the so-called chemical shift is a small difference in resonance frequency between fat and water protons produced by this principle (Fig. 1). However, the difference in frequencies is quite small, approximately 3.5 part per million (ppm). In a 3.0-T MRI machine, the difference can be calculated by multiplying 3.5 ppm with the Larmor frequency (128 MHz) and is about 450 Hz (3).]

Another physical background for fat-suppression techniques is that fat and water protons have different T1 relaxation times. To date, there is no perfect theory to accurately explain and predict the T1 relaxation time in a particular tissue, but several mechanisms known to affect the T1 relaxation time have been identified (4). These principal relaxation mechanisms include dipole–dipole interaction, chemical shift anisotropy, molecular translation, and chemical exchange. Dipole–dipole interactions are the most important single mechanism for proton relaxation in biological tissues. Among the factors that influence the dipole–dipole interactions, the one most closely related to the T1 relaxation time is the molecular rotational motion. This is usually referred to as the molecular tumbling rate and mathematically defined as the rotational correlation time, which is the time required for molecules to rotate by approximately 1 radian. Molecular rotational motion is faster for molecules that are smaller (due to their lower molecular weight), with less structured shapes (such as free water), and with higher temperatures. The Solomon–Bloembergen equations show

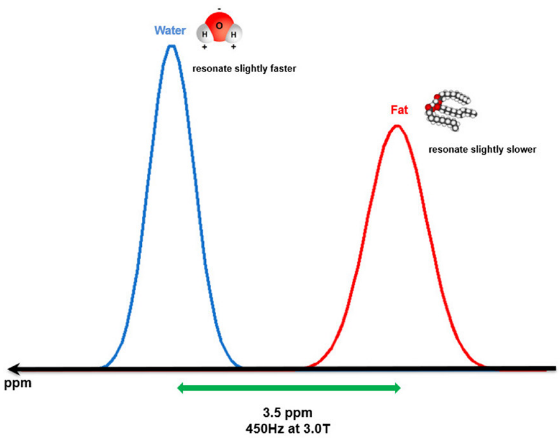

Fig. 1. Illustration of the water-fat chemical shift within 3.0-T strength magnetic field.
Water and fat protons show a spectral peak difference in the resonance frequency of about 450 Hz (3.5 ppm). Water protons resonate relatively faster than fat protons due to the deshielding effect.

that the T1 relaxation time is minimized whenever the molecular rotational motion (rotational correlation time) of a substance matches its Larmor frequency, suggesting that the dipole–dipole interactions are most optimized (5, 6). Fat molecules are relatively larger in molecular weight and more structured shape than water molecules, so they have a slower molecular rotational motion, which means that they have a rotational correlation time similar to that of the Larmor frequency, thus showing a shorter T1 relaxation time.

Overview of various fat-suppression techniques

A large number of techniques have been developed to suppress fat signals. Various fat-suppression techniques used for abdominal MRI can be classified into three categories: chemical shift-based, inversion-based, and hybrid forms that use both (Fig. 2). Chemical shift–based techniques include chemical shift selective (CHESS), water excitation, and Dixon methods. Among them, the Dixon method has the unique characteristic of that it can be used for fat quantification. CME 2d [Additionally, short tau inversion recovery (STIR) is an inversion-based technique and spectrally adiabatic inversion recovery (SPAIR) is a hybrid technique.]

Chemical shift-based techniques

CHESS

Because of the natural separation of the resonant frequencies of fat and water (i.e., chemical shift), it is possible to saturate fat protons only by applying a fat-selective 90° radiofrequency (RF) pulse with a narrow bandwidth tuned to the center of the fat resonance frequency. Following the application of a 90° fat-selective RF pulse, transverse magnetization of the fat protons is destroyed by a strong spoiler gradient. Eventually, these saturated fat protons are unable to generate MRI signals in subsequent imaging sequences such as spin-echo (SE) or gradient-echo (GRE) sequences (Fig. 3).

TP, CME 3d [CHESS, commonly called fat-saturation imaging (or "fat-sat") is easy to implement and is applicable to almost all imaging sequences (7). Also, CHESS is the most commonly used technique for suppressing fat signals in T1-weighted, contrast-enhanced MRI (8).] It does not change the T1 contrast of the tissue, unlike STIR, which will be discussed further later. CHESS requires additional preparatory steps, such as fat-selective saturation RF pulsation and the spoiler gradient, which increase the overall scan time. However, some MRI systems support the technique (e.g., Quick FatSat, Siemens Healthineers) in a manner that shortens the total scan time by applying it more sparsely instead of deploying a fat-selective RF pulse at every repetition time (TR) interval.

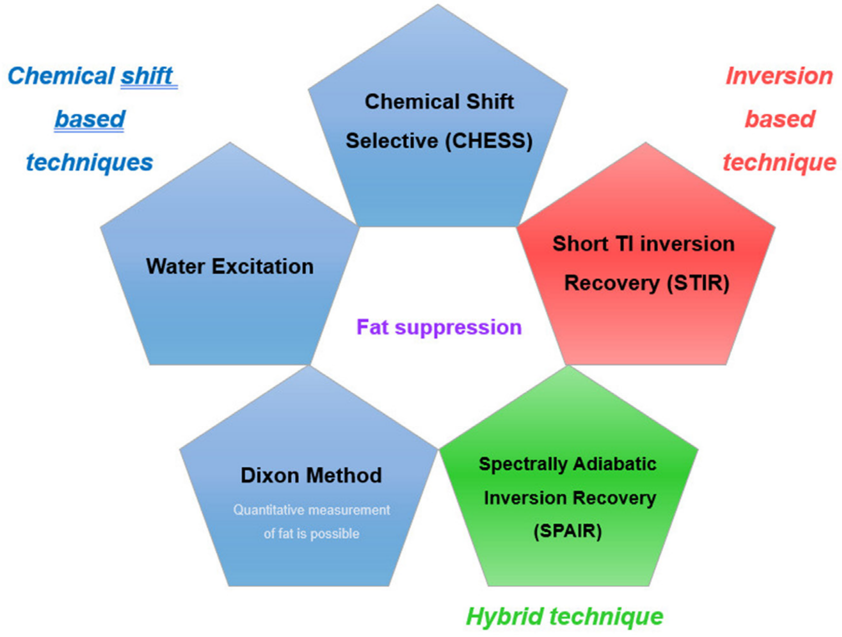

Fig. 2. Three categories of fat suppression techniques for abdominal MRI.
Blue pentagons represent chemical shift-based techniques, a red pentagon represents an inversion-based technique, and a green pentagon represents a hybrid technique.

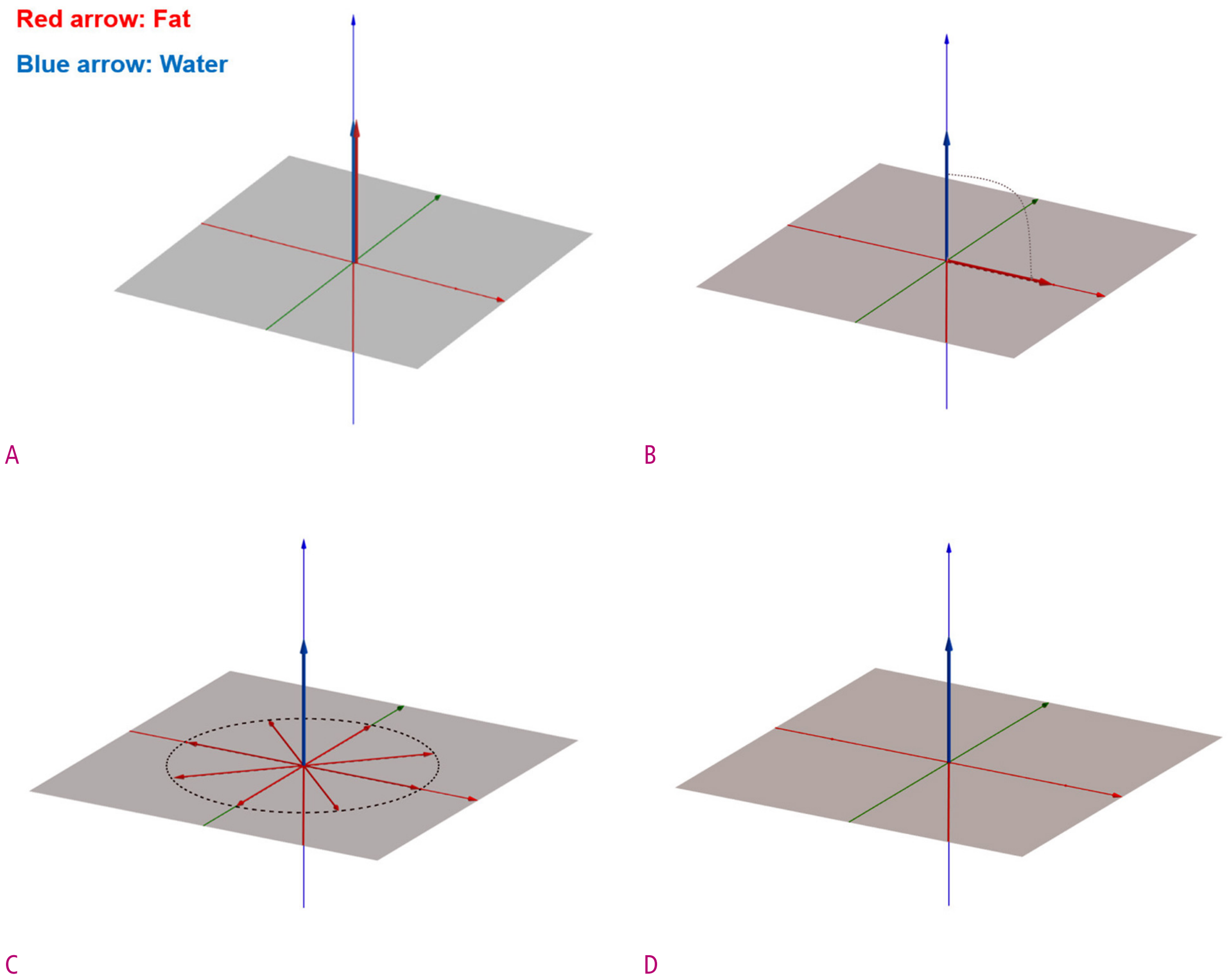

Fig. 3. Diagrams show the implementation of CHESS technique.
(A) Before any RF pulse is applied, both water and fat protons are aligned with only longitudinal magnetization components in the main magnetic field. (B) After applied a 90° fat-selective RF pulse, only fat protons are converted to transverse magnetization, and water protons remain unchanged. (C) The transverse magnetization of fat protons is destroyed by the dephasing spoiler gradient. (D) Finally, only the longitudinal magnetization of the water protons remains.

The biggest disadvantage of CHESS is that its performance is greatly influenced by the strength and homogeneity of the main magnetic field. As shown above, the difference in resonance frequency between water and fat protons is proportional to the strength of the main magnetic field. If the main magnetic field is too weak, then the efficiency of selectively saturating only fat protons using narrow bandwidth RF pulses markedly decreases or even becomes to do impossible. The main magnetic field homogeneity also influences successful fat suppression. On fat-suppressed MRI scans with CHESS, it is common to see that fat suppression has failed around metallic substances and at the tissue interfaces with large differences in magnetic susceptibility (Fig. 4). Strategies for limiting main magnetic field inhomogeneity include using a smaller field of view to exclude areas of inhomogeneity and altering the external magnetic field (i.e., shimming) to counteract internal field inhomogeneity. CHESS is also affected by the inhomogeneity of the RF pulse field, which is also known as B_1 field inhomogeneity. If the fat-selective RF pulse is inhomogeneous, poor fat suppression and even water suppression may result (8).

Water excitation

Based on the use of chemically selective RF pulses, water excitation is a method of selectively stimulating water

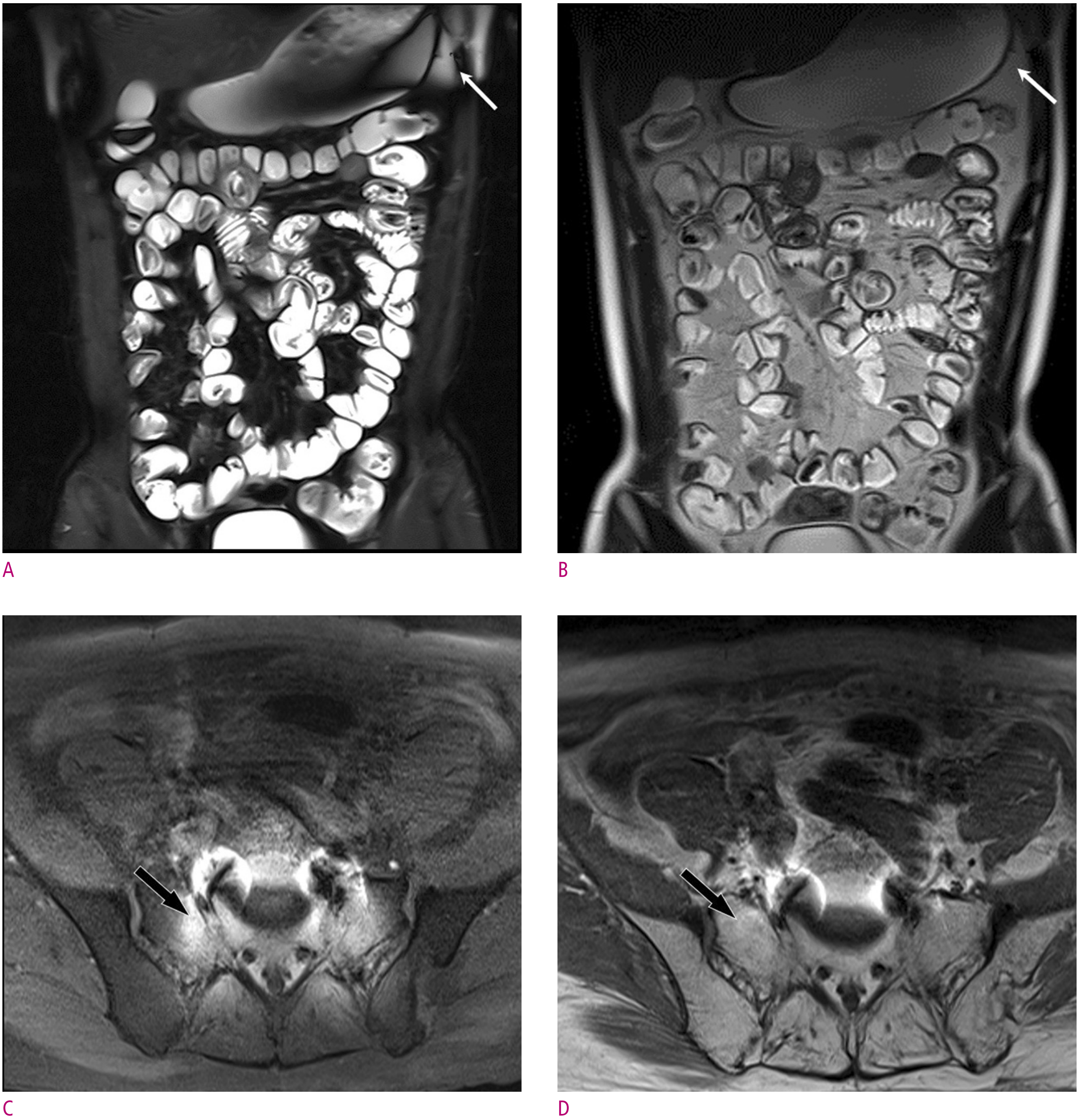

Fig. 4. Examples of failure to suppress fat using CHESS.
(A) and (B) T2-weighted HASTE abdominal coronal images of a 17-year-old man with Crohn's disease with (A) and without (B) fat saturation show poorly suppressed peritoneal fat signal on the left side of the stomach (arrow). This is due to magnetic susceptibility differences at the air-fluid interfaces in the stomach. (C) and (D) T1-weighted pelvic axial images of an 80-year-old man suffering from prostate cancer with (C) and without (D) fat saturation show failure of fat suppression in the sacrum and surrounding soft tissues (arrow), due to metallic implants inserted into the lumbosacral spine. Such metallic implants can induce strong main magnetic field inhomogeneities.

protons, unlike CHESS, which saturate fat protons only (9). Water excitation is also referred to as spectral–spatial imaging because it consists of selective excitations of both the spectral band and the spatial region (7). There are

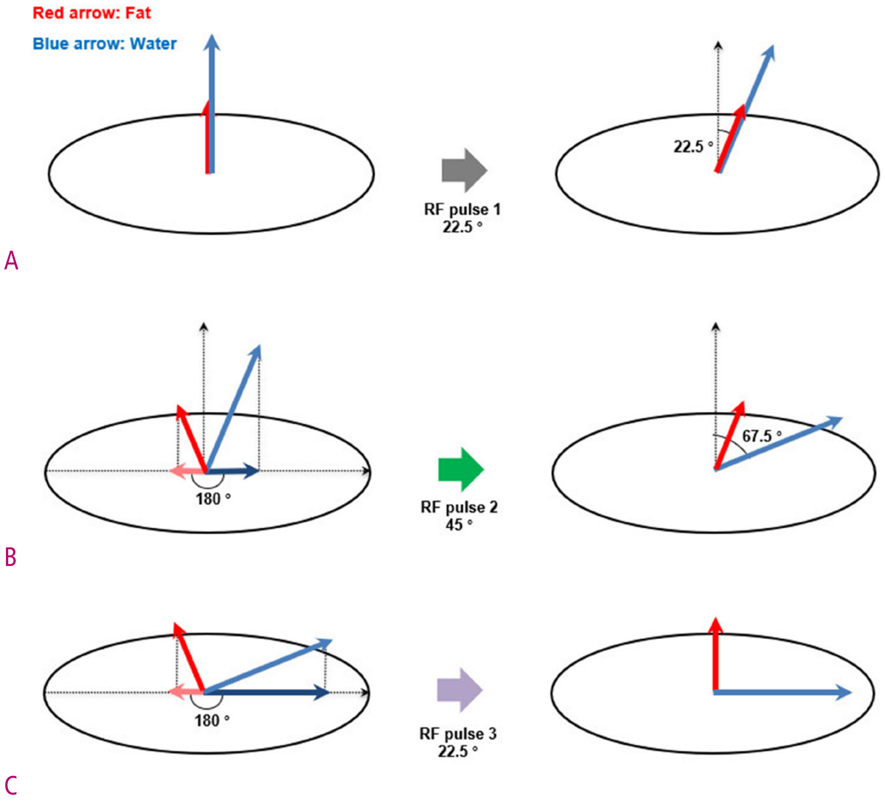

Fig. 5. Diagrams show the implementation of water excitation technique with 1-2-1 triplet binomial RF pulse.
(A) Initially, both water and fat protons have only a longitudinal magnetization in the main magnetic field. By the first RF pulse, the magnetization vector of water and fat protons forms an angle of 22.5° with the longitudinal axis. (B) Wait until the phase difference of the transverse magnetization component caused by the difference in the resonance frequency between water and fat protons becomes 180°. At this moment, a second RF pulse is applied and the magnetization vector of the water protons forms an angle of 67.5° with the longitudinal axis. (C) Again, wait until the phase difference of the transverse magnetization component between water and fat protons becomes 180°. The third RF pulse not only completes the 90° transverse magnetization of the water protons, but also the fat protons return to the initial longitudinal position.

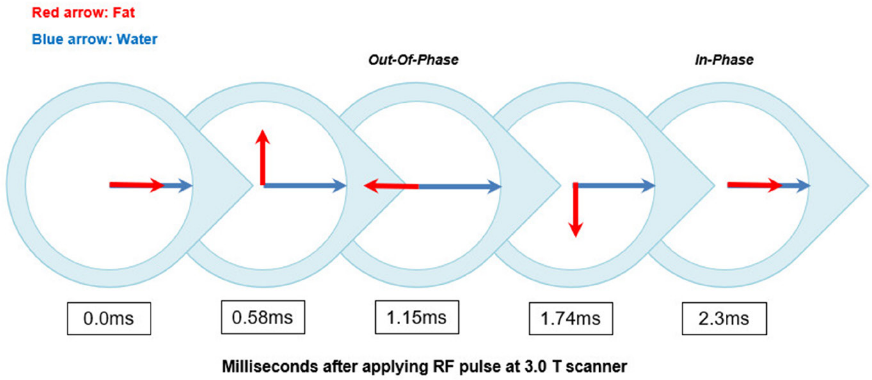

Fig. 6. Illustration of the phase difference cycling of water and fat protons at 3.0-T scanner.
1.15 milliseconds after the RF pulse is applied, the water and fat protons have a phase difference of exactly 180°. This moment is called out-of-phase (OP). After an additional 1.15 milliseconds, the phase difference between water and fat protons again becomes zero, and this moment is called in-phase (IP). At the 3.0 T scanner, the water and fat protons will be IP or OP every 2.3 milliseconds.

several interesting routes by which the water-excitation technique excites only water protons. It uses binomial pulses, which involve flipping the angles following the pattern of coefficients of the binomial expansion of $(a+b)^n$, instead of a 90° fat-selective RF pulse. Any combination whose ratios satisfy the binomial pattern and add up to 90° will operate to selectively excite water protons and leave the fat resonance unchanged. The most commonly used binomial pulse is a 1–2–1 triplet (22.5°–45°–22.5°). This does not require a spoiler gradient for dephasing the transverse magnetization of fat protons.

A detailed implementation is illustrated in Fig. 5. First, there is an initial excitation of 22.5° RF pulse applied to both the fat and water. After a short waiting period,

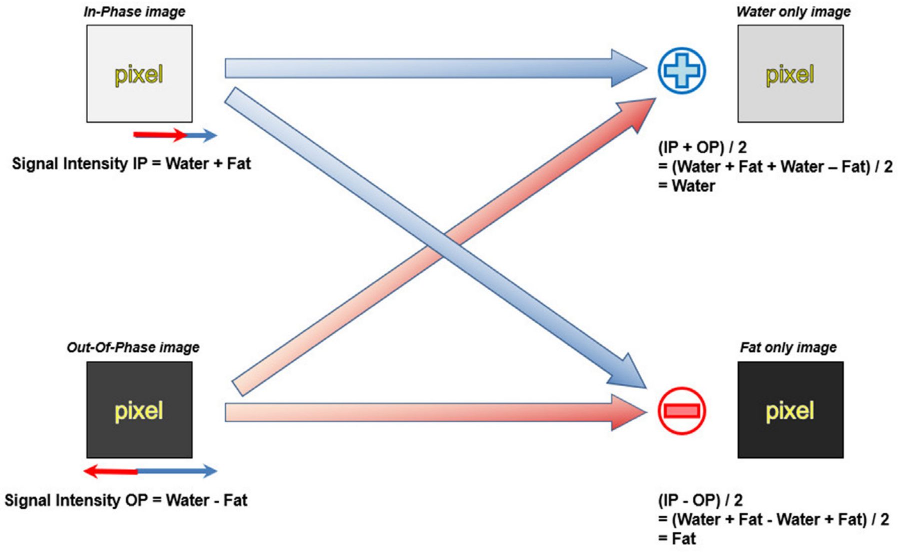

Fig. 7. Illustration of the basic idea of the two-point Dixon method.
The signal intensity of the IP image is the sum of water and fat, whereas the signal intensity of the OP image is the difference between water and fat. Water only image and fat only image can be calculated by intuitive postprocessing of the IP and OP image datasets. The water only image can be obtained by adding the IP and the OP image and dividing by 2, and the fat only image can be obtained by subtracting the OP image from the IP and dividing by 2.

there comes a point at which a phase difference of 180° occurs in the transverse magnetization due to the different resonant frequencies of fat and water. The 45° excitation angle then tips the magnetization of water protons to 67.5° with respect to the longitudinal direction, whereas the magnetization of fat protons is flipped to 22.5° in the same direction. After the second waiting time, a 22.5° RF pulse completes the 90° transverse magnetization of the water protons, and the fat protons return to the longitudinal position and thus do not contribute to the MRI signal. The water-excitation technique is also sensitive to the main magnetic field inhomogeneity, yet is strongly insensitive to B_1 field inhomogeneity because its nulling of fat signals is implemented by the timing of interpulse delays that allow it to avoid incomplete fat suppression linked to B1 field inhomogeneity (10).

The Dixon method

First proposed by Dixon in 1984 (11), the Dixon method encompasses a group of chemical shift–based techniques using the in-phase (IP)/out-of-phase (OP) cycling of fat and water. Water and fat protons have different resonance frequencies (i.e., chemical shift), and the phase difference of their transverse magnetization changes periodically over time. Hence, these two transverse magnetization vectors point in the same direction (IP, phase difference is 0°) or in the opposite direction (OP, phase difference is 180°) at each specific interval (Fig. 6). Given a water–fat resonance frequency difference of 450 Hz inherent with the 3.0-T machine, the water and fat protons will be IP every 2.3 ms. The basic idea of the Dixon method is straightforward: two separate sets of images—that is, water-only and fat-only images—can be calculated by intuitive postprocessing of the IP and OP image datasets. The IP and OP image datasets are summed to obtain water-only images, while the OP image dataset is subtracted from the IP image dataset to obtain fat-only images (Fig. 7).

In the early days, Dixon's original proposal (referred to as the two-point method) was not very successful due to the B_0 inhomogeneity that resulted in phase errors and water–fat swapping (10). Nowadays, however, it became one of the fat-suppression techniques supported by almost all MRI system manufacturers due to the advances in magnet design, the development of shimming techniques, and the evolution of correction and calculation algorithms.

TP [The modern modified Dixon method mainly employs a multipoint (three points or more) approach in which a third imaging phase is added to correct the phase error from the first two images. It is insensitive to both B_0 and B_1 magnetic field inhomogeneities.] Besides, the various types of modified Dixon methods that currently exist all deliver four image sets with different degrees of contrast during a single acquisition, between the IP and OP images, and between fat-only and water-only images (Fig. 8). This helps with image co-registration and simplification of imaging protocols (7). As will be explained below, fat-only images

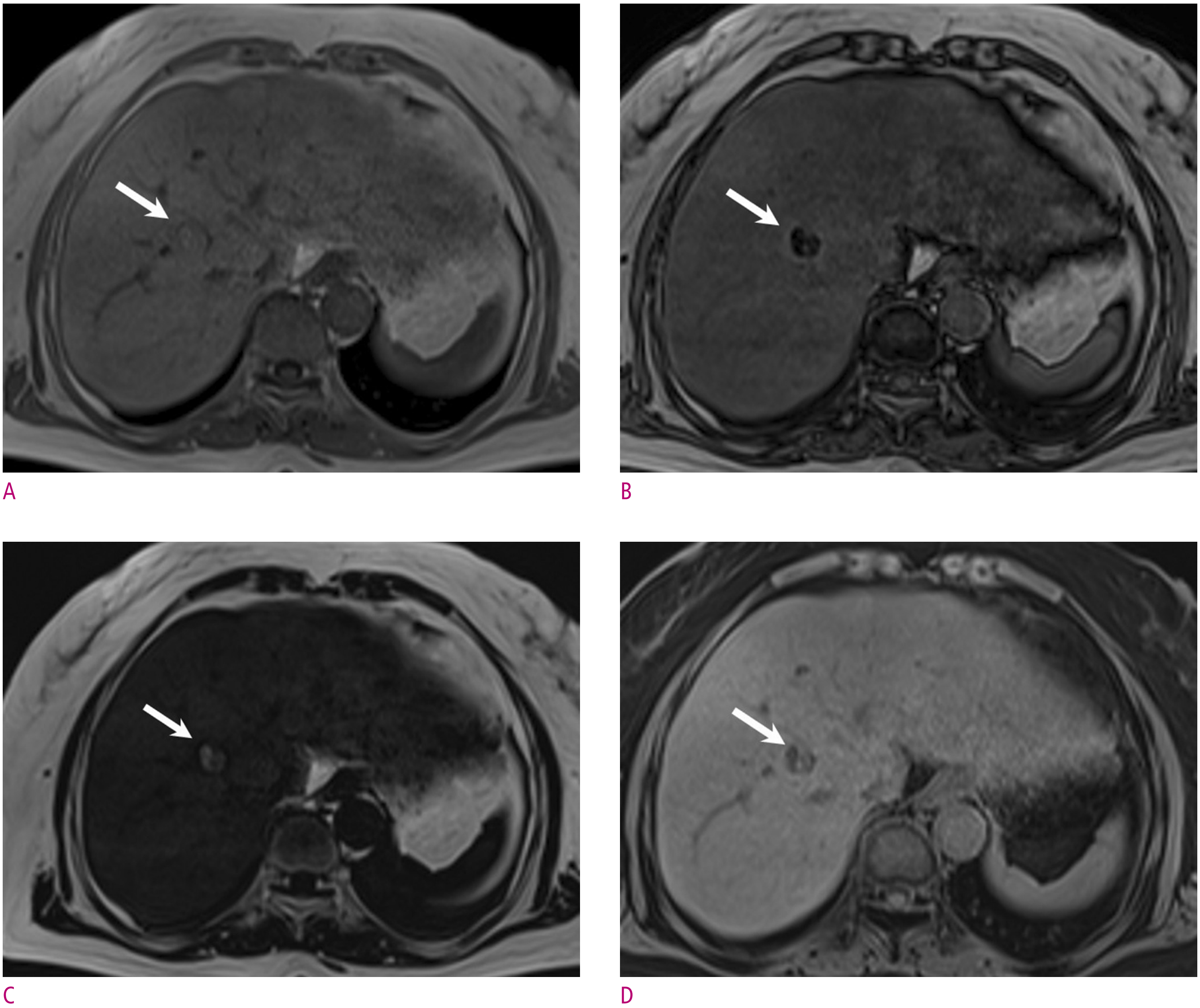

Fig. 8. Four different contrast image sets obtained by the Dixon method of an adenoma in the liver of a 37-year-old woman.
(A) and (B) The lesion shows iso-signal intensity on IP image (A), but OP image (B) shows that the lesion is depicted marked signal intensity drop than normal liver parenchyma. (C) and (D) The lesion (arrow) has a distinct portion that shows high signal intensity on fat only image (C) and low signal intensity (D) on water only image. This is an important clue to the diagnosis of hepatic adenoma.

can also be used for fat quantification. They can also be used in combination with almost any pulse sequences, including SE, GRE, and contrast-enhanced imaging. Many of these advantages make the modern modified Dixon method the most widely used fat-suppression technique in abdominal MRI. Although generally better than CHESS, the modern Dixon method also suffers from main magnetic field inhomogeneities around metal, which cause very strong susceptibility effects. Further, it also increases the overall scan time, but a few complementary methods have been suggested using optimized parallel imaging algorithms (12). CME 4a [Interestingly, the Dixon method has a signal swap artifact, which is a unique artifact that cannot be seen in other techniques (Fig. 9). It is a phenomenon in which the signals of water and fat are interchanged due to incorrect convergence in the process of mathematical computations caused by a natural ambiguity between fat and water when only one chemical species dominates the signal from the pixels (10).]

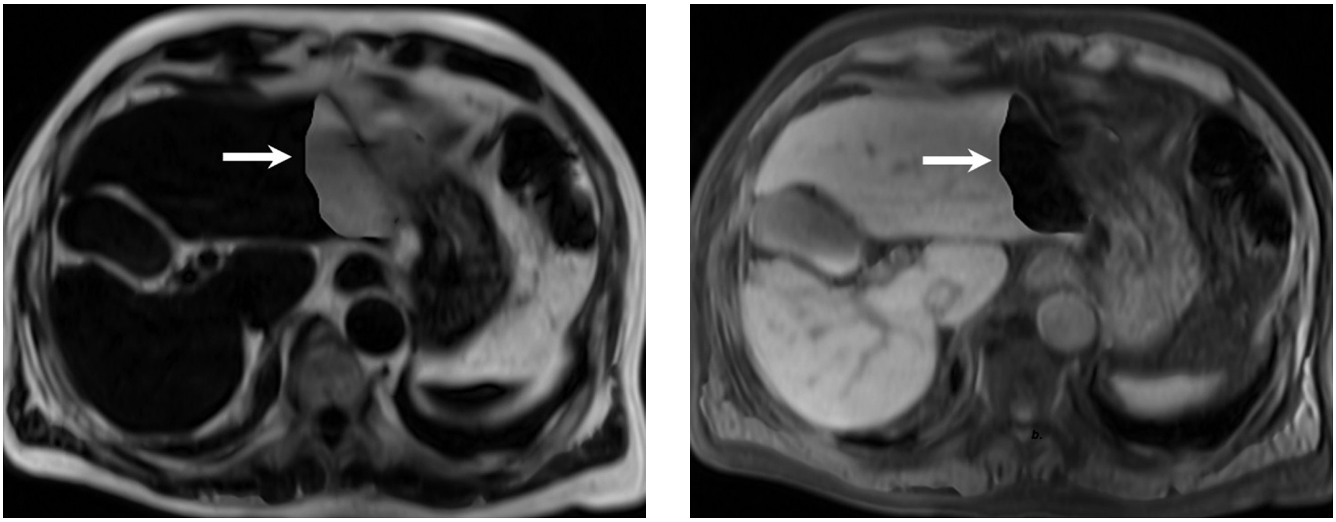

A

B

Fig. 9. An example of fat-water swap artifact of a 78-year-old man with a hepatocellular carcinoma (not shown).
In both the fat only image (A) and water only image (B) obtained by the Dixon method, a geographic region with incorrect signal intensity was seen in the left lateral section of the liver (arrow). Herein, the main cause of the swap artifact is thought to be the main magnetic field inhomogeneity caused by the heart.

Inversion-based and hybrid techniques

STIR

As mentioned earlier, fat protons have a shorter T1 relaxation time than water protons. After a 180° inversion RF pulse, the longitudinal magnetization of fat protons will be restored faster than that of water protons. If a 90° excitation RF pulse is applied at the time point at which the longitudinal magnetization of fat protons is zero (inversion time, TI_{null}), the fat protons will not contribute to the MRI signal, whereas water protons will still produce a signal (Fig. 10). The stronger the main magnetic field, the longer the T1 relaxation time; the TI_{null} value of 3.0-T MRI needed to nullify the fat signal is in the range of 205 to 225 ms as compared with 100 to 200 ms for 1.5-T MR imaging (13).

TP [The STIR method is relatively insensitive to B_0 inhomogeneity and can be used with permanent magnets of a low magnetic field strength, which have poor magnetic field homogeneity.] This approach is usually better than other fat-suppression methods (such as CHESS), especially around metallic substances (e.g., orthopedic implants or endoscopic/surgical clips), near tissue interfaces with high susceptibility differences (around a gaseous bowel), and across large body parts (even whole-body imaging). In addition, STIR has another advantage in terms of contrast—specifically, the capacity for additive T1 + T2 contrast. In general SE imaging, T1 and T2 contrast compete with each other. By applying a 180° inversion RF pulse, however, they instead adopt an

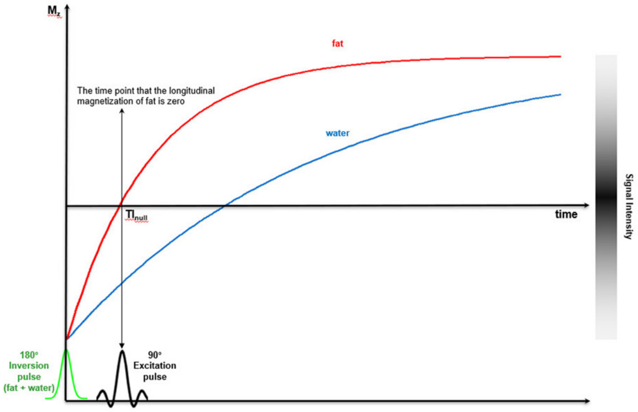

Fig. 10. Diagram of STIR technique. It is based on the different T1 relaxation time of water and fat.
A 180° inversion RF pulse inverts longitudinal magnetization of all tissues, including water and fat. The inverted magnetization of water and fat restored over time under T1 relaxation. During this process, because fat has a much shorter T1 relaxation time a time occurs where the inverted longitudinal magnetization of water and fat passes through zero. If that time (TI_{null}) is set to fat and then a 90° excitation RF pulse is applied, fat protons will not be able to contribute to the MR signal.

additive relationship. The image contrast may be increased and, in particular, tissues with long T1 and long T2 relaxation times appear very bright (14).

The first disadvantage of STIR is that the overall signal-to-noise ratio (SNR) of the images is low. When the imaging sequence starts at TI_{null}, most of the protons exhibit a reduced magnitude of longitudinal magnetization and, therefore, the magnitude of transverse magnetization induced by a 90° RF pulse is also reduced, which leads to a reduction in the overall SNR. CME 7b [Another serious drawback of STIR is that fat suppression is nonspecific. Signals from all tissues or substances with a T1 relaxation time similar to fat can be suppressed. These include mucus, hemorrhage, proteinaceous solutions, and even gadolinium for contrast enhancement (15). Hence, STIR cannot be used as a fat-suppression technique in images after contrast enhancement.] It is also difficult to find the optimal TI_{null} that varies depending on the anatomical location and individual. In terms of the image acquisition time and patient safety, additional inversion pulses significantly increase the total scan time and tissue heating.

SPAIR

SPAIR is a hybrid technique that combines features of both STIR (inversion recovery nulling) and CHESS (fat-selective RF pulse with spoiler gradient) for fat suppression. The technique begins with a 180° inversion fat-selective RF pulse (Fig. 11). Only fat protons are selectively inverted and water protons are not affected. This specially designed RF pulse is called an adiabatic pulse, meaning that both frequency and amplitude are modulated (16). CME 5d [The advantage of an adiabatic pulse is that it can accurately convert the longitudinal and transverse magnetization by exactly 180°, even if the B_1 field is not uniform.] Next, spoiler gradients are employed to ensure the destruction of any inadvertent transverse magnetization of fat protons created by the RF pulse. The subsequent steps are the same as those seen during usual inversion recovery techniques. An excitation RF pulse is applied at the time at which fat protons cross the null point of longitudinal magnetization; these fat protons will not contribute to the MRI signal.

Theoretically, SPAIR may be a very suitable technique for equipment of 3.0 T or higher because it can adopt both the advantages of a high main magnetic field strength that improve the spectral resolution of the chemical shift and the temporal resolution of the inversion recovery (7). SPAIR is not only relatively less sensitive to B_0 inhomogeneity like STIR but also insensitive to B_1 inhomogeneity and capable of selective fat supression by using an adiabatic pulse and spoiler gradient (17). However, there are penalties that occur on the image acquisition time and tissue heating relative to CHESS due to the use of 180° inversion RF pulse and, so, this approach is mainly preferred for T2-weighted imaging.

MRI techniques that quantify fat measurement

Fat signal fraction and proton-density fat fraction (PDFF)

The fat signal fraction is commonly used as an intuitive and simple metric for MRI-based fat-quantification techniques. It can be calculated by dividing the signal from the fat protons by the sum of the signal from the water protons and that from the fat protons. Most recent studies use PDFF as a metric, which can be considered as a standardized, accurate, objective, and reproducible biomarker. It was initially defined by Reeder et al. as the following: "the fraction of unconfounded proton signal

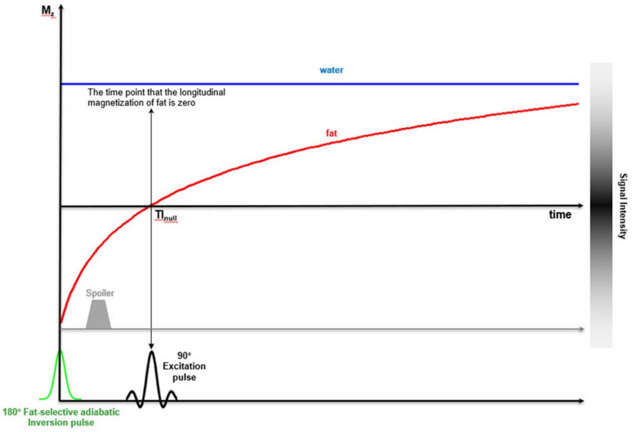

Fig. 11. Diagram of SPAIR technique.
It can be said to be the combination of STIR and CHESS. SPAIR uses a 180° inversion RF pulse like STIR, but instead of inverting the longitudinal magnetization of all tissues, it uses an adiabatic RF pulse that selectively inverts only fat with a spoiler gradient like CHESS. The use of adiabatic RF pulse makes SPAIR less sensitive to B_1 field inhomogeneity.

from mobile fat, normalized by the total hydrogen proton density from all mobile proton species" (2). PDFF has been proposed for the quantification of hepatic steatosis, but researchers are now expanding its application to fat quantification of the pancreas, adrenal glands, and fat-containing tumors (18). To accurately estimate PDFF, all multiple confounding factors described below must be corrected, and this applies to both magnetic resonance spectroscopy (MRS) and MRI-based fat-quantification techniques.

Fat quantification by MRS

MRS represents the type and content of molecules constituting a specific anatomical location (typically a single voxel) as a peak signal. The position of each peak listed on the horizontal axis of the MRS record represents the molecular species, while the size of each peak represents the quantity of the molecular species. Fat and water can be quantified directly from the areas under their corresponding peaks in the acquired spectrum, and the fat fraction can be subsequently calculated (18). If performed properly, this approach is the most accurate of the noninvasive fat-quantification methods known so far and can detect even very small amounts of fat (2). MRS has been used as a reference standard to verify accuracy in several MRI-based fat quantification studies (19–22). Unfortunately, MRS has a fatal drawback: the spatial coverage is extremely limited to only a single voxel and, as a consequence, some degree of sampling error is unavoidable. In addition, there are problems that a lot of time and specialized experts are required to perform MRS and analyze the results.

Chemical shift-based method for fat quantification

CME 6b [Several researchers have proposed fat-quantification techniques using chemical shift–based methods, especially based on the two- or multipoint Dixon method (21).] These chemical shift–based methods are classified into two categories as follows, depending on their use of phase data: magnitude-based and complex-based. In contrast, the magnitude-based method discards phase data, while the complex-based method uses it.

In the most widely used simple magnitude-based two-point Dixon method, the fat signal fraction can be obtained by dividing the difference between the IP and OP signal intensities by double the IP signal intensity (Fig. 7). Recall that IP is the sum of the signals from water and fat protons, and OP is the difference between the signals of water and fat protons. However, the fat signal fraction acquired by the calculation presented above does not reflect the true fat fraction (i.e. PDFF) because of multiple confounding factors (e.g., T1-weighting bias, T2* decay, spectral complexity of the fat, noise bias, and eddy currents) that corrupt the ability of the technique to quantify fat (22). PDFF can be accurately measured only by removing the effects of these multiple confounding factors. It is also important to note that using a magnitude-based approach is only possible to achieve a dynamic range of 0% to 50% of the fat signal fraction (2). This limitation can only be resolved with additional phase information (23), so the complex-based method is necessary to quantify tissues composed mostly of fat, such as adipose tissue.

T1-weighting bias as a confounding factor

Most MRI methods used to acquire fat fraction images use T1-weighted GRE methods. In this context, T1-weighting bias occurs because these T1-weighted sequences artificially amplify the relative signal of the shorter T1 proton species, which will result in a measured fat fraction that is greater than the true fat fraction (i.e., overestimation). The use of low-flip-angle GRE imaging to avoid T1-weighting is the strategy generally adopted by most emerging approaches that attempt to avoid the T1-weighting bias (24).

T2 decay as a confounding factor*

MRI methods used to quantify fat employ multiple different echo times from one another. Regardless, however, during that time, T2* decay is ongoing and corrupts estimates of the fat fraction. This process is especially amplified in iron-overload conditions (which produce T2* shortening), and the measured fat fraction can be markedly underestimated. The confounding effect of T2* can be removed by either incorporating T2* into the signal model used to separate water and fat, thereby correcting for T2* decay as part of the fitting (27, 28), or by measuring T2* separately and correcting for the effects of T2* (29, 30).

Spectral complexity of fat as a confounding factor

Usual chemical shift–based fat quantification methods assume the signal from fat exists as a single spectral peak at ~3.5 ppm upfield from that of water. Unfortunately, this assumption is not true. At clinical magnetic field strengths, fat protons have at least six distinct spectral peaks at different resonance frequencies. This will lead to significant quantification errors (29). A method called "spectral modeling" was proposed to correct the error due to the additional peaks of the fat. It is based on the biochemical structure of human liver triglycerides and has been devised independently by several researchers (27, 32) based on an algorithm for chemical shift species separation for hyperpolarized ^{13}C imaging (31).

Noise bias as a confounding factor

Noise bias occurs if the magnitude of water and fat images have low signal intensities (i.e., values near 0). In these areas, most of the acquired signals contain almost only the magnitude of noise. Consqeuncely, the signal intensities of the decomposed fat images with low fat content and water images with low water content will be artifactually increased by the noise. Phase-constrained reconstruction or magnitude-discrimination methods can be ways to eliminate noise bias (24). For images with high SNR, the former is preferred, while, in the opposite case, the latter method is preferred.

Eddy currents as a confounding factor

Rapidly switching gradients make loops of electrical current, known as eddy currents, which lead to phase shift in complex images acquired at different echo times. Eventually, these currents induce errors in the fat fraction estimation of techniques using phase information. There are two main ways to correct these eddy currents. The first is to use magnitude-based techniques (34, 35), which do not use any phase information and are naturally immune to eddy currents, but, as mentioned above, their dynamic range is limited to 0% to 50%. As such, a hybrid complex–magnitude approach using magnitude fitting has also been proposed to correct the eddy currents while maintaining the full dynamic range (34).

Complex-based technique with confounding factor correction

CME 6b [The iterative decomposition of water and fat with echo asymmetry and least-squares estimation (IDEAL) is an algorithm based on GRE imaging and the multipoint Dixon method (35).] IDEAL begins by gaining multi-echo (at least three) magnitude and phase image pairs. Collected multi-echo signals can be formulated in a matrix form as follows:

$$S=A\cdot\begin{bmatrix} water \\ fat \end{bmatrix}+n$$

where S denotes the acquired signals, the matrix A is considered known, and n is the variance of noise (36). Water and fat components can be calculated from a weighted least-squares inversion as follows:

$$\begin{bmatrix} water \\ fat \end{bmatrix}=(A^{T}\cdot W\cdot A)^{-1}\cdot A^{T}\cdot W\cdot S$$

where the weights are given by W. This equation can be solved using a modified Gauss–Newton algorithm iteratively (37). Finally, by adding algorithms (e.g., low flip angle, T2* correction, spectral modeling of fat, magnitude discrimination, and magnitude fitting) that correct the multiple confounding factors shown above, it is possible to accurately calculate PDFF while having a full dynamic range (Fig. 12).

Conclusion

The detection and quantification of fat in abdominal MRI is an important part of diagnosis and research. Recent fat-suppression techniques can be divided into chemical shift–based and inversion-recovery techniques, and are continuously developing rapidly. Each technique has its own strengths and limitations. TP [The most recent proposed fat-quantification techniques are based on the modern modified Dixon method and algorithms for correcting multiple confounding factors have been added to it. These techniques can accurately and noninvasively measure PDFF.] For radiologists, good understanding and proper application of these techniques are undoubtedly important and helpful in identifying and analyzing abdominal pathologic conditions such as tumor or chronic parenchymal disease.

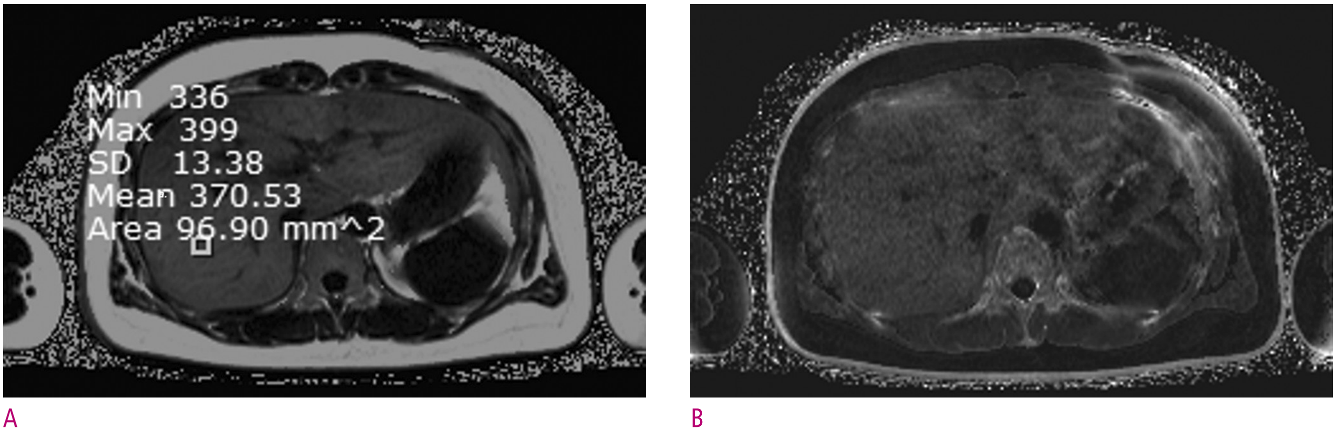

Fig. 12. An example of quantitative hepatic steatosis assessment of a 34-year-old-female who will be a living donor for liver transplantation. Images were obtained using a 3.0-T MRI machine (Verio, Siemens Healthineers, Germany) and commercial software (LiverLab, Siemens Healthineers, Germany). (A) The PDFF map image shows the fat signal fraction of the entire liver. The fat signal fraction of the square-shaped region of interest (ROI) in the image was measured to be about 37.1 %. Make sure that the PDFF map has a dynamic range from 0 to 100 %. (B) The estimated R2* map is shown, in order to the correction of T2* decay effect. Noting that R2* is the inverse of T2* value. A higher R2* value correlates with a faster T2* decay.

Funding

This work was supported by a National Research Foundation of Korea (NRF) grant funded by the Korean government (MSIT) (no. 2019R1F1A1060566).

References

1. Kramer H, Pickhardt PJ, Kliewer MA, Hernado D, Chen GH, Zagzebski JA, et al. Accuracy of liver fat quantification with advanced CT, MRI, and ultrasound techniques: Prospective comparison with MR spectroscopy. Am J Roentgenol 2017;208:92-100.
2. Reeder SB, Sirlin CB. Quantification of liver fat with magnetic resonance imaging. Magn. Reson. Imaging Clin. N. Am 2010. p. 337-357.
3. Merkle EM, Dale BM. Abdominal MRI at 3.0 T: The Basics Revisited. Am J Roentgenol 2006;186:1524-1532.
4. Bloembergen N, Purcell EM, Pound R V. Relaxation effects in nuclear magnetic resonance absorption. Phys Rev 1948;73:679-712.
5. Bloembergen N. Spin relaxation processes in a two-proton system. Phys Rev 1956;104:1542-1547.
6. Bloembergen N, Morgan LO. Proton relaxation times in paramagnetic solutions. Effects of electron spin relaxation. J Chem Phys 1961;34:842-850.
7. Pokharel SS, Macura KJ, Kamel IR, Zaheer A. Current MR imaging lipid detection techniques for diagnosis of lesions in the abdomen and pelvis. Radiographics 2013;33:681-702.
8. Delfaut EM, Beltran J, Johnson G, Rousseau J, Marchandise X, Cotten A. Fat suppression in MR imaging: Techniques and pitfalls. Radiographics 1999;19:373-382.
9. Hauger O, Dumont E, Chateil JF, Moinard M, Diard F. Water excitation as an alternative to fat saturation in MR imaging: Preliminary results in musculoskeletal imaging. Radiology 2002;224:657-663.
10. Bley TA, Wieben O, François CJ, Brittain JH, Reeder SB. Fat and water magnetic resonance imaging. J Magn Reson Imaging 2010;31:4-18.
11. Dixon WT. Simple proton spectroscopic imaging. Radiology. Radiology; 1984;153:189-194.
12. Pruessmann KP, Weiger M, Scheidegger MB, Boesiger P. SENSE: Sensitivity encoding for fast MRI. Magn Reson Med 1999;42:952-962.
13. Gold GE, Han E, Stainsby J, Wright G, Brittain J, Beaulieu C. Musculoskeletal MRI at 3.0 T: Relaxation times and image contrast. Am J Roentgenol 2004;183:343-351.
14. Bydder GM, Young IR. MR imaging: clinical use of the inversion recovery sequence. J Comput Assist Tomogr 1985;9:659-675.
15. Krinsky G, Rofsky NM, Weinreb JC. Nonspecificity of short inversion time inversion recovery (STIR) as a technique of fat suppression: Pitfalls in image interpretation. Am. J.

Roentgenol 1996;166:523-526.

16. Tannús A, Garwood M. Adiabatic pulses. NMR Biomed 1997;10:423-434.
17. Hardy CJ, Edelstein WA, Vatis D. Efficient adiabatic fast passage for NMR population inversion in the presence of radiofrequency field inhomogeneity and frequency offsets. J Magn Reson 1986;66:470-482.
18. Hong CW, Fazeli Dehkordy S, Hooker JC, Hamilton G, Sirlin CB. Fat Quantification in the Abdomen. Top. Magn. Reson. Imaging 2017;26: 221-227.
19. Yokoo T, Shiehmorteza M, Hamilton G, Wolfson T, Schroeder ME, Middleton MS, et al. Estimation of hepatic proton-density fat fraction by using MR imaging at 3.0 T. Radiology 2011;258:749-759.
20. Zhong X, Nickel MD, Kannengiesser SAR, Dale BM, Kiefer B, Bashir MR. Liver fat quantification using a multi-step adaptive fitting approach with multi-echo GRE imaging. Magn Reson Med 2014;72:1353-1365.
21. Reeder SB, Cruite I, Hamilton G, Sirlin CB. Quantitative assessment of liver fat with magnetic resonance imaging and spectroscopy. J Magn Reson Imaging 2011;34:729-749.
22. Kim H, Taksali SE, Dufour S, Befroy D, Goodman TR, Petersen KF, et al. Comparative MR study of hepatic fat quantification using single-voxel proton spectroscopy, two-point Dixon and three-point IDEAL. Magn Reson Med 2008;59:521-527.
23. Ma J. Breath-hold water and fat imaging using a dual-echo two-point dixon technique with an efficient and robust phase-correction algorithm. Magn Reson Med 2004;52:415-419.
24. Liu CY, McKenzie CA, Yu H, Brittain JH, Reeder SB. Fat quantification with IDEAL gradient echo imaging: Correction of bias from T1 and noise. Magn Reson Med 2007;58:354-364.
25. Yu H, Shimakawa A, McKenzie CA, Brodsky E, Brittain JH, Reeder SB. Multiecho water-fat separation and simultaneous R*2 estimation with multifrequency fat spectrum modeling. Magn Reson Med 2008;60:1122-1134.
26. O'Regan DP, Callaghan MF, Wylezinska-Arridge M, Fitzpatrick J, Naoumova RP, Hajnal JV, et al. Liver fat content and T2*: Simultaneous measurement by using breath-hold multiecho MR imaging at 3.0 T - Feasibility. Radiology 2008;247:550-557.
27. Guiu B, Petit JM, Loffroy R, Salem DB, Aho S, Masson D, et al. Quantification of liver fat content: Comparison of triple-echo chemical shift gradient-echo imaging and in vivo proton MR spectroscopy. Radiology 2009;250:95-102.
28. d'Assignies G, Ruel M, Khiat A, Lepanto L, Chagnon M, Kauffmann C,et al. Noninvasive quantitation of human liver steatosis using magnetic resonance and bioassay methods. Eur Radiol 2009;19:2033-2040.
29. Reeder SB, Robson PM, Yu H, Shimakawa A, Hines CDG, McKenzie CA, et al. Quantification of hepatic steatosis with MRI: The effects of accurate fat spectral modeling. J Magn Reson Imaging 2009;29:1332-1339.
30. Bydder M, Yokoo T, Hamilton G, Middleton MS, Chavez AD, Schwimmer JB, et al. Relaxation effects in the quantification of fat using gradient echo imaging. Magn Reson Imaging 2008;26(3):347-359.
31. Reeder SB, Brittain JH, Grist TM, Yen YF. Least-squares chemical shift separation for 13C metabolic imaging. J Magn Reson Imaging 2007;26:1145-1152.
32. Qayyum A, Coh JS, Kakar S, Yeh BM, Merriman RB, Coakley F V. Accuracy of liver fat quantification at MR imaging: Comparison of out-of-phase gradient-echo and fat-saturated fast spin-echo techniques - Initial experience. Radiology 2005;237:507-511.
33. Hussain HK, Chenevert TL, Londy FJ, Gulani V, Swanson SD, McKenna BJ, et al. Hepatic fat fraction: MR imaging for quantitative measurement and display - Early experience. Radiology 2005;237:1048-1055.
34. Yu H, Shimakawa A, Reeder SB, Mckenzie CA, Brittain JH. Magnitude Fitting Following Phase Sensitive Water-Fat Separation to Remove Effects of Phase Errors [Internet]. Concord (CA): International Society for Magnetic Resonance in Medicine [cited 2021 Mar 1]. Availabel from: https://cds.ismrm.org/protected/09MProceedings/files/00461.pdf
35. Reeder SB, McKenzie CA, Pineda AR, Yu H, Shimakawa A, Brau AC, et al. Water-fat separation with IDEAL gradient-echo imaging. J Magn Reson Imaging 2007;25:644-652.
36. Yu H, McKenzie CA, Shimakawa A, Vu AT, Brau ACS, Beatty PJ, et al. Multiecho reconstruction for simultaneous water-fat decomposition and T2* estimation. J Magn Reson Imaging 2007;26:1153-1161.
37. Chebrolu V V., Hines CDG, Yu H, Pineda AR, Shimakawa A, McKenzie CA, et al. Independent estimation of T*2 for water and fat for improved accuracy of fat quantification. Magn Reson Med 2010;63:849-857.

친구인가 원수인가: 복부 자기공명영상에서 지방 신호를 억제하고 측정하는 방법

김호군[1], 최준일[1,2], 이현수[3]

[1]가톨릭대학교 의과대학 서울성모병원 영상의학과,
[2]가톨릭대학교 의과대학 암연구소,
[3]지멘스 헬시니어스

초 록

복부자기공명영상에서 지방 신호를 억제하는 것은, 복부 장기의 병적 상태를 진단하는 임상적 상황에서 기본적이고 일상적으로 이루어지고 있다. 과거 수십년간 다양한 지방억제 기법이 개발되었고 최근에는 지방의 정량적 측정 기법 역시 개발되었다. 지방억제기법은 화학변이를 이용하는 화학변이선택(CHESS) 기법과 물분자 자극을 이용하는 화학변이에 기반을 둔 방법과 딕슨(Dixon) 방법의 두가지로 크게 나눌 수 있다. CHESS 기법은 가장 흔히 사용되는 지방억제기법으로 지방만을 선택하는 고주파펄스를 이용하여 지방의 신호를 없애는 방법이다. 물분자 자극은 물분자만을 자극하는 이항펄스를 이용한다. 딕슨기법은 지방과 물의 신호 벡터가 정위상과 역위상을 반복하는 것을 이용한다. STIR라고 불리는 반전을 이용하는 기법은 사전에 모든 조직의 신호를 반전시키는 자극펄스를 이용하며 적절한 반전시간을 선택함으로서 지방의 종축자기화를 없애 지방양성자가 MRI 신호를 내지 못하게 한다. SPAIR 기법은 CHESS와 STIR를 혼합한 기법이다. 지방의 정량적 측정을 위한 가장 정확한 방법은 다점 딕슨기법을 이용한 복잡한 방법이며 PDFF라고 불린다. 지방의 정확한 정량적 측정을 위해서는 여러가지 교란변수가 교정되어야 한다. 영상의학과 의사는 MRI의 다양한 지방 억제 및 정량적 측정 기법에 익숙해져야 하며 환자 진료에 이들을 적절히 적용시킬 수 있어야 한다.

www.e-kjar.org
https://doi.org/10.52668/kjar.2022.00136

pISSN 2586-1719 / eISSN 2799-3299
Copyright © The Korean Society of Abdominal Radiology

Korean J Abdom Radiol 2022;6:37-50

Original Article

Important CT Findings for Prediction of Incomplete (R1 or R2) Resection and Poor Survival of Perihilar Cholangiocarcinoma after Curative-Intent Surgery

Hyo-Jin Kang[1,2], Jung Hoon Kim[1,2], Ijin Joo[1,2], Won Chang[2,3]
[1]*Department of Radiology, Seoul National University Hospital, Seoul, Korea*
[2]*Department of Radiology, Seoul National University College of Medicine, Seoul, Korea*
[3]*Department of Radiology, Seoul National University Bundang Hospital, Sungmam-si, Korea*

Purpose: To evaluate CT findings to predict incomplete (R1 or R2) resection and poor survival in patients with perihilar cholangiocarcinoma using pre-operative CT.

Materials and Methods: From 2006 to 2012, a total of 139 patients with perihilar cholangiocarcinoma who underwent pre-operative multiphase CT and subsequent curative-intent surgery were included. After two radiologists independently reviewed CT findings including the likelihood of bile duct (BD) involvement from intrapancreatic common bile duct (CBD) to bilateral second-order branches and peritumoral fat stranding using a 5-point scale, vessel involvement (no, abutment, encasement), and LN involvement, imaging findings were finalized by a consensus of two radiologists. When the likelihood scale of 4 or more on preoperative CT was regarded as BD involvement, the diagnostic ability of CT was analyzed by the receiver operating curve using histopathologic results as a reference standard. Residual tumor categorized into no residual tumor (R0) and residual tumor (R+; R1 or R2). Predictive factors of R+ resection on pre-operative CT were analyzed by logistic regression. Cox proportional hazard model was used to determine the prognostic factor for overall survival by using pre-operative CT findings and laboratory results.

Results: Seventy-one patients were R0 and sixty-eight patients were R+ resection. For resectability evaluation, mid-CBD involvement (score ≥ 4) in pre-operative CT was significant factor for R+ resection in multivariable analysis ($P < 0.01$) with substantial interobserver agreement. In multivariable Cox regression, intrapancreatic CBD involvement (score ≥ 4, hazard ratio [HR] = 1.81, $p < 0.01$) as well as elevated total bilirubin (HR = 1.53, $p = 0.04$) and CA 19-9 level (HR = 1.75, $p < 0.01$) were significant predictors for poor survival. Diagnostic ability to predict mid-CBD and intrapancreatic CBD involvement on pre-operative CT were 0.71 and 0.72 (AUC values).

Conclusions: Distal longitudinal extent of perihilar cancer on pre-operative CT is a significant factor for margin positive resection and poor survival on curative-intent surgery.

Keywords: Perihilar; Computed tomography; Prognosis; Resection

Received: March 7, 2022 **Revised:** May 18, 2022 **Accepted:** May 19, 2022
Correspondence: Jung Hoon Kim, MD, PhD
Department of Radiology, Seoul National University College of Medicine, 101 Daehangno, Jongno-gu, Seoul, 03080, Korea
Tel: +82-2-2072-3107 Fax: +82-2-743-6385 E-mail: loveyoon@snu.ac.kr
This is an Open Access article distributed under the terms of the Creative Commons Attribution Non-Commercial License (http://creativecommons.org/licenses/by-nc/4.0/) which permits unrestricted non-commercial use, distribution, and reproduction in any medium, provided the original work is properly cited.

Introduction

Perihilar cholangiocarcinoma (PHC) is the most common malignancy of the bile duct, accounting for more than half of all cholangiocarcinoma (1). Prognosis of PHC is grim with a median survival of 6 months without any treatment (2). At present, complete surgical resection offers only a chance for cure and long term survival with a reported median survival of 19 to 39 months (3) in patients without distant metastasis. Many studies have been identified poor prognostic factors after curative-intent surgery of PHC, such as a positive resection margin, moderate to poor tumor differentiation, and perineural invasion (4-6). Among them, tumor-free surgical margin is the most important and well known prognostic factor for PHC (6, 7). However, tumor-positive surgical margin is frequently observed in resected PHC due to its anatomic location, which can spread longitudinally (intrahepatic or intrapancreatic bile duct) and/or transversely (hepatic artery, portal vein, perineural tissue or lymphatics) (8, 9). Thus, many surgeons reported that extended surgery based on meticulous pre-operative evaluation is warranted to avoid incomplete resection, which undoubtedly leads to poor overall survival (10-13).

To determine resectability, contralateral hepatic artery or portal vein invasion, main portal vein invasion longer than 2 cm, small remnant liver volume, biliary extension to the contralateral secondary confluence with farther than 2cm from hepatic hilum on pre-operative cross-sectional images are the well known predictable factors for unresectability (14, 15). However, even with meticulous pre-operative evaluation, there is still considerable margin positive resection on curative intend surgery (8, 9). Recent advances in CT technology, such as multidetector CT (MDCT) and iterative reconstruction, enabled to achieve improved spatial and temporal resolution (16-18). Indeed, recent studies have reported the substantial predictability of MDCT to determine resectability for gallbladder cancer (19) or pancreas cancer (20).

Herein, with a propounding development of CT and image reconstruction technology, we surmised that predicting resectability of PHC using pre-operative CT has become more accurate, and also it offers more information regarding resectability assessment and survival. Therefore, the purpose of our study is to reveal CT findings to predict margin positive resection (R1 or R2) and poor survival in patients who underwent curative-intent surgery of perihilar cholangiocarcinoma using pre-operative CT.

Materials and Methods

This study was approved by our institutional review board, and the requirement for informed consent was waived.

Patients

From 2006 to 2012, we searched electronic medical record in our hospital consecutively to identify eligible patients who met following criteria: i) adult patient (≥ 18 years), ii) pathologically confirmed perihilar cholangiocarcinoma, iii) who underwent curative-intent surgery and iv) pre-operative multiphase abdominal CT. Exclusion criteria were as follows: history of other malignancy including perihilar or elsewhere, no recent CT within 4 weeks before surgery, or suboptimal CT image quality. According to the criteria, a total of 139 patients (82 men and 57 women; mean age, 66.9 years, age range, 42-75 years) were selected for this study (Fig. 1). All 139 patients underwent curative-intent surgery by one of two pancreatobiliary surgeons with 27 and 18 years of experience in pancreatobiliary surgery in the same institute. The extent of surgery were preoperatively discussed with board certified surgeons, radiologists and internists in a multidisciplinary team meeting The mean interval (± standard deviation) between last CT examination and surgery was 17.5 days ± 11.0 (range,

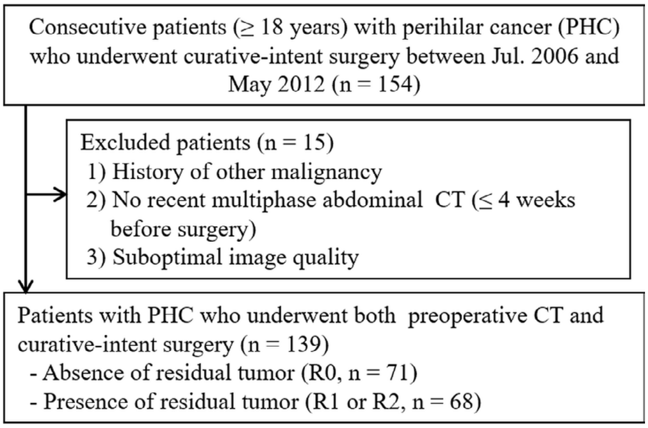
Consecutive patients (≥ 18 years) with perihilar cancer (PHC) who underwent curative-intent surgery between Jul. 2006 and May 2012 (n = 154)

Excluded patients (n = 15)
1) History of other malignancy
2) No recent multiphase abdominal CT (≤ 4 weeks before surgery)
3) Suboptimal image quality

Patients with PHC who underwent both preoperative CT and curative-intent surgery (n = 139)
- Absence of residual tumor (R0, n = 71)
- Presence of residual tumor (R1 or R2, n = 68)

Fig. 1. Flow diagram of patient population.

0 to 28 days). Patients underwent extended right hepatectomy (n = 48), extended right hepatectomy with pancreaticoduodenectomy (n = 2), extended left hepatectomy (n = 26), extended left hepatectomy with pancreaticoduodenectomy (n = 1), hilar resection (n = 56), hilar resection with pancreaticoduodenectomy (n = 2), bypass or open and closure (n = 4). Detailed patient demographics are summarized in Table 1.

CT technique

All patients underwent four-phase multidetector CT (MDCT) (n=96) consisting of pre-contrast, early arterial, late arterial and venous phase, or three-phase MDCT (n=43) consisting of pre-contrast, arterial and venous phase before curative-intent surgery. Owing to retrospective nature of this study, various CT scanner were used. Detail parameters of each CT scanner were noted in Appendix 1. Contrast media was injected at a rate of 2.0 to 3.0 mL/sec using a power injector with a total volume of 1.5 mL per kilogram of the patient body weight followed by flushing with 20 mL normal saline. After contrast media injection, an automatic bolus tracking technique was used for image acquisition. The trigger threshold was 100 HU at the abdominal aorta. Early arterial phase was obtained 6 seconds after the trigger threshold and pancreatic phase was obtained 5 to 9 seconds after the early arterial phase. Venous phase was obtained 40 to 50 seconds after early arterial phase.

Image analysis

Two board-certified radiologists (I.J. and W.C, with 12- and 9-years of experience in abdominal imaging) independently reviewed all pre-operative MDCT images. They were blinded to patients' histological or operative results, but were aware that this study population had PHC. Reviewers were requested to determine the likelihood of tumor involvement of bile duct (BD) in longitudinal and transverse plane. For longitudinal plane assessment, the likelihood of tumor involvement from intrapancreatic common bile duct (CBD) to bilateral second order branches of intrahepatic bile duct (IHD) using 5-point scale as follows: score 1, definitely no, no significant image findings; 2, probably no, presenting only short stricture with smooth transition; 3, indeterminate, one positive image finding suggestive of malignancy; 4, probably yes, two positive image findings suggestive of malignancy; 5, definitely yes, more than three positive image suggestive of malignancy. The positive image findings suggestive of malignancy are long-segmental involvement (> 12 mm), a thickened (> 1.5 mm) wall, luminal irregularity or asymmetry, and incremental enhancement may favor a malignant stricture (21, 22). For evaluating tumor involvement in the transverse plane to BD, following 5-point scale was used: score 1, definitely no, no significant image findings; 2, probably no, minimally increased attenuation in peritumoral fat; 3, indeterminate, increased attenuation with ground-glass like pattern in peritumoral fat; 4, probably yes, increased attenuation with reticular pattern in peritumoral fat; 5, definitely yes, obviously increased attenuation as much as BD wall (23). The cutoff for tumor involvement was determined by cutoff values from the receiver operating curve analysis. Mid-CBD was defined as CBD below cystic duct or more than 2 cm away from 1st bifurcation of CBD.

Also, the relation between tumor and vessels (proper, left and right hepatic artery [PHA, LHA, and RHA]; main, left and right portal vein [MPV, LPV, RPV]) was evaluated using three categories: no relation, abutment (180 degrees or less of a vessel's circumference), encasement (more than 180 degrees of tumor involvement of a vessel's circumference). In artery evaluation, abutment or encasement classified as tumor involvement. While vein evaluation, encasement, change caliber of vessels in the region of contact, or irregularity of vessel margin were assessed as tumor involvement (24). Furthermore, the anatomy type of BDs were assessed according to the five anatomy types reported by Huang et al. (25) namely, normal, trifurcation, right posterior BD draining to the left hepatic duct, right posterior BD draining to the common BD, and right posterior BD draining to the cystic duct. The conventional BD anatomy was defined as the right posterior BD draining to the right hepatic duct, with the right and left hepatic ducts joining the common hepatic duct. In addition, Bismuth type (26), and LN involvement (no significant LN enlargement, indeterminate LN, highly suspected metastatic LN) were also assessed. When LNs larger than 10 mm in short diameter, central necrosis or hyper-attenuating than liver in portal venous phase were considered highly suspected metastatic LN (14, 27). Indeterminate LN was defined when only one positive

Table 1. Summary of patient's demography, clinical characteristics, and histopathological findings according to resection margin

Parameter	Total (n = 139)	R0 (n = 71)	R+ (n = 68)	p
Age* (years)	66.9 (42-75)	64.7 (42-74)	69.2 (48-75)	0.11
Sex (%)				
M : F	82 : 57	43 : 28	39 : 29	0.25
Type of surgery				
Extended left hepatectomy	23 (16.5)	18 (25.4)	5 (7.4)	0.06
with PD	1 (0.7)	1 (1.4)	0 (0.0)	n/a
Extended right hepatectomy	52 (37.4)	29 (40.8)	23 (33.8)	0.10
with PD	2 (1.4)	0 (0.0)	2 (1.4)	n/a
Hilar resection	53 (38.1)	21 (29.6)	32 (47.1)	<0.01
with PD	4 (2.9)	2 (2.8)	2 (1.4)	n/a
Bypass or open and closure	4 (2.9)	0 (0.0)	4 (2.9)	n/a
Bismuth type				0.52
1	14 (10.1)	6 (8.5)	8 (11.8)	0.61
2	31 (22.3)	13 (18.3)	18 (12.9)	0.13
3a / 3b	61 (43.9) / 10 (7.2)	32 (45.1) / 7 (9.9)	29 (42.6) / 3 (4.4)	0.20 / 0.07
4	23 (16.5)	13 (18.3)	10 (14.7)	0.15
Histologic results				
Tumor length (cm)	2.97 ± 1.2	2.93 ± 1.1	3.01 ± 1.34	0.44
T stage				
1	13 (9.4)	8 (11.3)	5 (7.4)	0.10
2	87 (62.6)	39 (54.9)	48 (70.6)	0.04
3	34 (24.5)	24 (33.8)	10 (14.7)	0.03
4	1 (0.7)	0 (0.0)	1 (1.5)	n/a
N/A	4 (2.8)	0 (0.0)	4 (5.9)	n/a
LN				0.80
Negative	83 (59.7)	47 (66.2)	36 (52.9)	0.45
Positive	52 (37.4)	22 (31.0)	30 (44.1)	0.71
N/A	4 (2.9)	2 (2.8)	2 (2.9)	
Angiolymphatic invasion				0.15
Negative	84 (60.4)	48 (67.6)	36 (52.9)	
Positive	46 (33.1)	22 (30.9)	24 (35.3)	
N/A	9 (6.5)	1 (1.4)	8 (11.8)	
Perineural invasion				0.58
Negative	28 (20.1)	18 (25.4)	10 (14.7)	
Positive	107 (76.9)	53 (74.6)	54 (79.4)	
N/A	4 (2.8)	0 (0.0)	4 (5.9)	
Laboratory results*				
Total bilirubin (mg/dL)	3.1 (0.4 - 34.8)	2.4 ± 2.6	3.7 ± 4.9	0.06
Albumin (g/dL)	3.8 (2.7 – 4.7)	3.8 ± 0.4	3.8 ± 0.4	0.94
Alkaline phosphatase (IU/L)	247.1 (1.4 –1646)	201.8 ± 120.9	294.5 ± 235.4	0.01
CEA (ng/mL)	61.0 (0.6 – 5690)	5.5 ± 17.9	111.9 ± 702.4	0.21
CA19-9 (U/mL)	86248.0 (1.0 – 7200000)	127281.7 ± 865209	41470.6 ± 160165	0.42
AST (IT/L)	63.5 (12.0 – 397.0)	53.9 ± 31.3	73.5 ± 70.9	0.04
ALT (IU/L)	89.5 (7.0 – 770.0)	73.4 ± 61.0	106.3 ±124.1	0.06

Note.- Values in parentheses are percentages unless indicated otherwise; * values are mean and range; PD, pancreaticoduodenectomy, CEA, carcinoembryonic antigen; CA19-9, Carbohydrate antigen 19-9; AST, aspartate aminotransferase; ALP, alkaline phosphatase.

findings of metastatic LN was noted.

Laboratory and histologic analysis

The pre-operative level of total bilirubin, albumin, alkaline phosphatase, carcinoembryonic antigen (CEA), carbohydrate antigen 19-9 (CA 19-9) have been routinely checked for pre-operative planning of perihilar cancer in our hospital. When the patients received a biliary intervention to decompress the bile duct before surgery (n = 25, 18.0%), the laboratory results after biliary intervention were used for analysis.

For histologic analysis, all surgical specimens were reviewed by an experienced pathologist (K.L. with more than 17 years' experience in pancreaticobiliary pathology). Information of tumor location, tumor size, depth of invasion, lymph node involvement, angiolymphatic, venous, or perineural invasion, and surgical margin were routinely reported in the pathologic reports at our hospital. After curative-intent surgery, microscopically (R1) or marcroscopically (R2) residual tumor was noted in 68 patients, while 71 patients did not (R0). The survival data were obtained from the official death reports issued by the government.

Statistical analysis

To determine predictive factor for margin positive resection (R1 or R2) on pre-operative CT, a chi-square test was used for univariable analysis (likelihood of BD involvement from intrapancreatic CBD to bilateral second-order branches, peritumoral fat infiltration, the relation between tumor and vessels, and LN involvement). The parameters that proved to be significant on the univariable analysis (tail p-values less than 0.1) were then subsequently tested with the multivariable using logistic regression. The survival rate during the follow-up period was reported with a 95% confidence interval using the Kaplan-Meier method. After univariable analysis of each parameter (pre-operative image findings, laboratory results, and extent of surgery) using a log-rank test, the parameters that proved to be significant (tail p-values less than 0.1) were then subsequently tested with the multivariable analysis using Cox proportional hazard model. Interobserver agreement was assessed using weighted κ statistics for noncontinuous scale and intraclass correlation coefficient (ICC) for continuous scale. The strength of agreement was evaluated as follows: a κ value and ICC value of less than 0.20 indicated poor agreement; 0.21-0.40, fair agreement; 0.41-0.60, moderated agreement; 0.61-0.80, good agreement; and 0.81-1.0, excellent agreement. The analysis were performed using commercial statistical softwares (SPSS version 23, IBM Corporation, Armonk, NY or MedCalc ver. 16.4, MedCalc software, Marikerkem Belgium). For all statistical analysis, P value less than 0.05 were considered statistically significant.

Results

After curative-intent surgery, microscopically (R1, n = 44) or marcroscopically residual tumor (R2, n = 24) were noted in 68 patients. Of 68 patients, 45 (66.2%) were involving proximal margin, 29 (42.6%) were distal margin, 10 (14.7%) were radial margin, and 2 (2.9%) were presenting seeding nodules. Eighteen patients (12.9%) were showing surgical margin positive at more than two site. T stage of PHC were as follows: T1, n = 13 (9.4%); T2, n = 87 (62.6%); T3, n = 34 (24.5%); T4, n = 1 (0.7%). Four patients (2.8%) were not applicable for T stage due to receive bypass or open and closure surgery. Fifty-two patents (37.4%) presented pathologically proven LN metastasis, and there is no significant difference between R0 and R+ group. More patient (n = 26, 38.2%) underwent hilar resection in R+ group ($p < 0.01$) than R0 group. Thirty-eight patients (28.5%) presented anatomic variation of bile duct: trifurcation (n = 13), right posterior bile duct drains to common hepatic duct (n=13), and right posterior bile duct drains to left hepatic duct (n = 12). There is no variation showing and right posterior bile duct drains to cystic duct. Table 1 summarized patient's demography, clinical and histopathological features.

Important CT findings for complete resection of perihilar cancer

Table 2 summarized important CT findings according to the resection margin status in perihilar cancer. By comparing histopathologic results, the AUC value of mid CBD involvement on pre-operative CT was 0.71 (cutoff score ≥ 4; sensitivity, 87.2%; specificity of 55.5%) and intrapancreatic CBD involvement was 0.72 (cutoff score ≥ 4; sensitivity, 60.0%; specificity of 91.6%). On univariable

Table 2. Summary of important CT findings according to resection margin in perihilar cancer

	Univariable					Multivariable		Accuracy
	Image findings	Involvement	R0	R+	P	Odds ratio	P	
Tumor extent	Hilum	(–)	65 (46.8)	60 (43.2)	0.516			
		(+)	6 (4.3)	8 (5.8)				
	BD 2nd order	(–)	19 (13.7)	26 (18.7)	0.204			
		(+)	52 (37.4)	42 (30.2)				
	Mid CBD	(–)	30 (21.6)	13 (9.4)	0.045	3.09 (1.44, 6.67)*	0.004	0.71 (0.63, 0.78)
		(+)	41 (29.5)	55 (39.6)				
	Intrapancreatic CBD	(–)	67 (48.2)	57 (41.0)	0.045	2.28 (0.68, 7.75)*	0.118	0.72 (0.63, 0.79)
		(+)	4 (2.9)	11 (7.9)				
Vessel involvement	RHA	(–)	42 (30.2)	33 (23.7)	0.209			
		(+)	29 (20.9)	35 (25.2)				
	LHA	(–)	64 (46.0)	64 (46.0)	0.385			
		(+)	7 (5.0)	4 (2.9)				
	RPV	(–)	71 (51.1)	67 (48.2)	0.489			
		(+)	0 (0.0)	1 (0.7)				
	LPV	(–)	64 (46.0)	67 (48.2)	0.063	0.24 (0.03, 2.10)*	0.194	0.88 (0.80, 0.94)
		(+)	7 (5.0)	1 (0.7)				
	MPV	(–)	67 (48.2)	59 (42.4)	0.124			
		(+)	4 (2.9)	9 (6.5)				
Others	LN	(–)	67 (48.2)	63 (45.3)	0.741			
		(+)	4 (2.9)	5 (3.6)				
	Peritumoral fat infiltration	(–)	55 (39.6)	54 (38.8)	0.78			
		(+)	16 (11.5)	14 (10.1)				

Note.- Values in parentheses are percentages unless indicated otherwise. * Values in parentheses are 95%CI.

analysis, mid-CBD (score ≥ 4) or intrapancreatic CBD (score ≥ 4) involvement on pre-operative CT were significant factors for margin positive resection (*p* = 0.045 and 0.045, respectively). None of the vessel involvement, peritumoral fat infiltration, or lymphadenopathy on pre-operative CT were presented significant differences in resectability. On multivariable analysis, mid CBD involvement (score ≥ 4) on pre-operative CT (odds ratio = 3.09, 95% CI 1.44-6.67, *p* = 0.004) remained significant factor for margin positive resection (Table 2, Fig. 2). The mid CBD involvement (score ≥ 4) on pre-operative CT predicted 92.9% (26/28) of distal margin positive resection (*p* = 0.002), but did not associated with proximal margin (*p* = 0.254) or radial margin positive resection (*p* = 0.435).

In assessment of tumor extent, good to excellent interobserver agreement were found: intrapancreatic CBD (ICC = 0.83), mid-CBD (ICC = 0.73), first order of IHD (κ = 0.63) and second order of IHD (κ = 0.67) involvement. Regarding vessel relation assessment (κ = 0.32, 0.52 and 0.74 for RPV, LPV and MPV, κ = 0.35 and 0.52 for RHA and LHA, respectively) and peritumoral fat infiltration (ICC = 0.47), fair to good agreement were found.

Important clinical and CT findings for overall survival after curative intent surgery

Of 139 patients, 112 patients (80.6 %) were deceased owing to the following cause: progression of PHC (n = 101), pneumonia (n = 5), progression of other malignancies (n = 3), and sepsis (n = 3). The mean follow up time was 37.8 ± 34 months (95% confidence interval [CI], 19.2 – 31.4 months). The median survival was 25.3 ± 3.12 months (interquartile range, 11.5 – 55.9 months). The mean survival was 24.8 ± 19.5 months, and mean follow-up period for survivor was 92.0 ± 27.8 months.

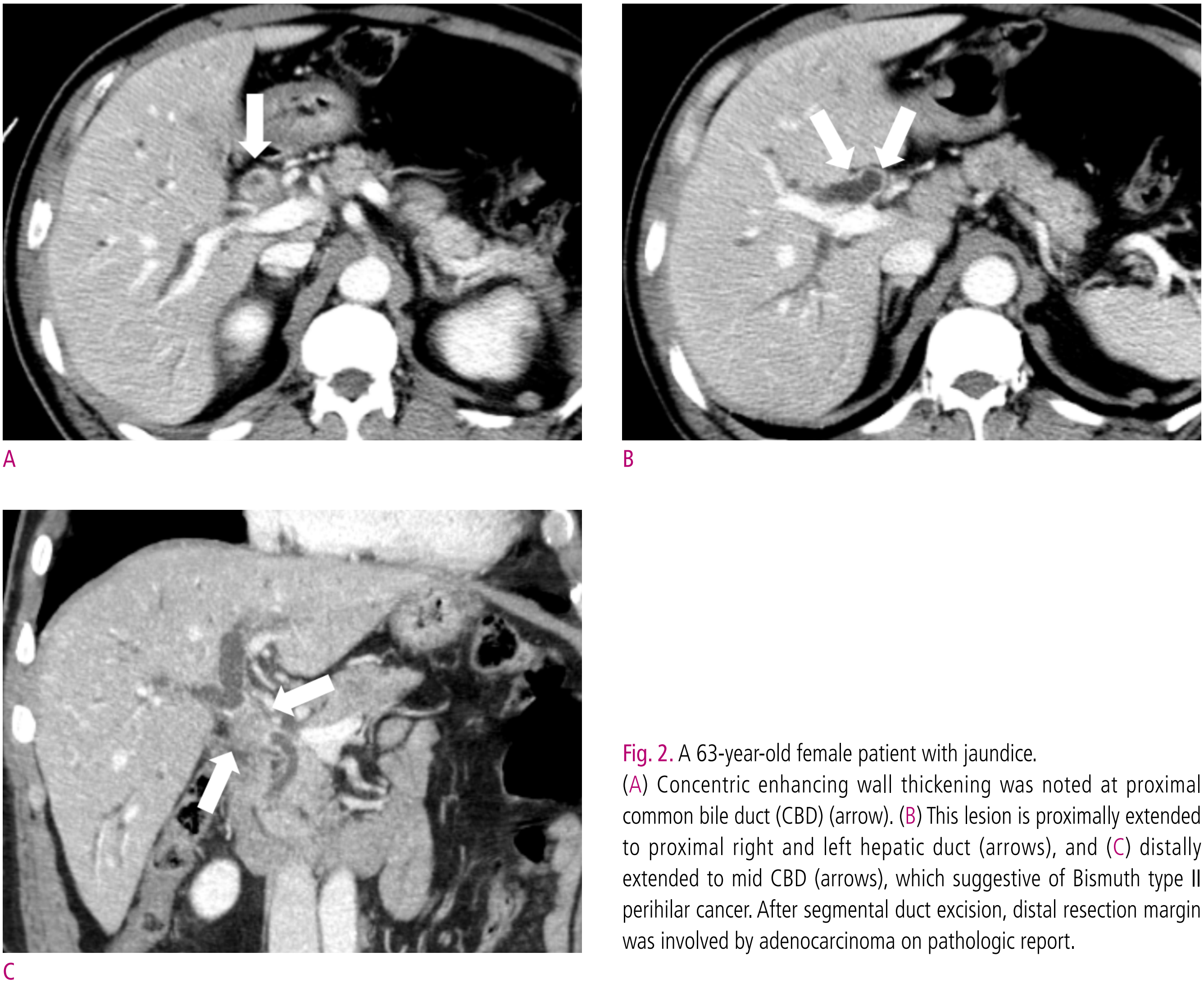

Fig. 2. A 63-year-old female patient with jaundice.
(A) Concentric enhancing wall thickening was noted at proximal common bile duct (CBD) (arrow). (B) This lesion is proximally extended to proximal right and left hepatic duct (arrows), and (C) distally extended to mid CBD (arrows), which suggestive of Bismuth type II perihilar cancer. After segmental duct excision, distal resection margin was involved by adenocarcinoma on pathologic report.

Table 3 summarized important clinical and CT findings for overall survival after curative intent surgery in perihilar cancer. In univariable analysis, elevated level of total bilirubin ($p = 0.03$) and CA 19-9 ($p = 0.02$), intrapancreatic CBD ($p < 0.01$) and second order branches of IHD involvement ($p = 0.07$) on pre-operative CT were significant risk factor for survival. On multivariable analysis, increased level of total bilirubin (> 1.2 mg/dL , hazard ratio [HR] = 1.53, $p = 0.04$), CA 19-9 (> 37 U/mL, HR = 1.75, $p < 0.01$), and intrapancreatic CBD involvement (score ≥ 4, HR = 1.81, $p < 0.01$) on pre-operative CT were the significant predictor for poor overall survival (Figs. 3 and 4).

Discussion

In our study, we found that mid-CBD involvement in pre-operative CT imaging was a significant factor for margin positive resection. In survival analysis, intrapancreatic CBD involvement in pre-operative CT was a significant factor for poor survival (HR = 1.81, $p < 0.01$). Even though there have been many studies that stated a significant relationship between vascular involvement and resectability (28-30), there are limited studies for the relationship between the distal extent of tumor and resectability. Also, it is notable that high interobserver agreements in evaluating intrapancreatic CBD (ICC = 0.83) and mid-CBD (ICC = 0.73) involvement, which are crucial for consistent pre-operative planning.

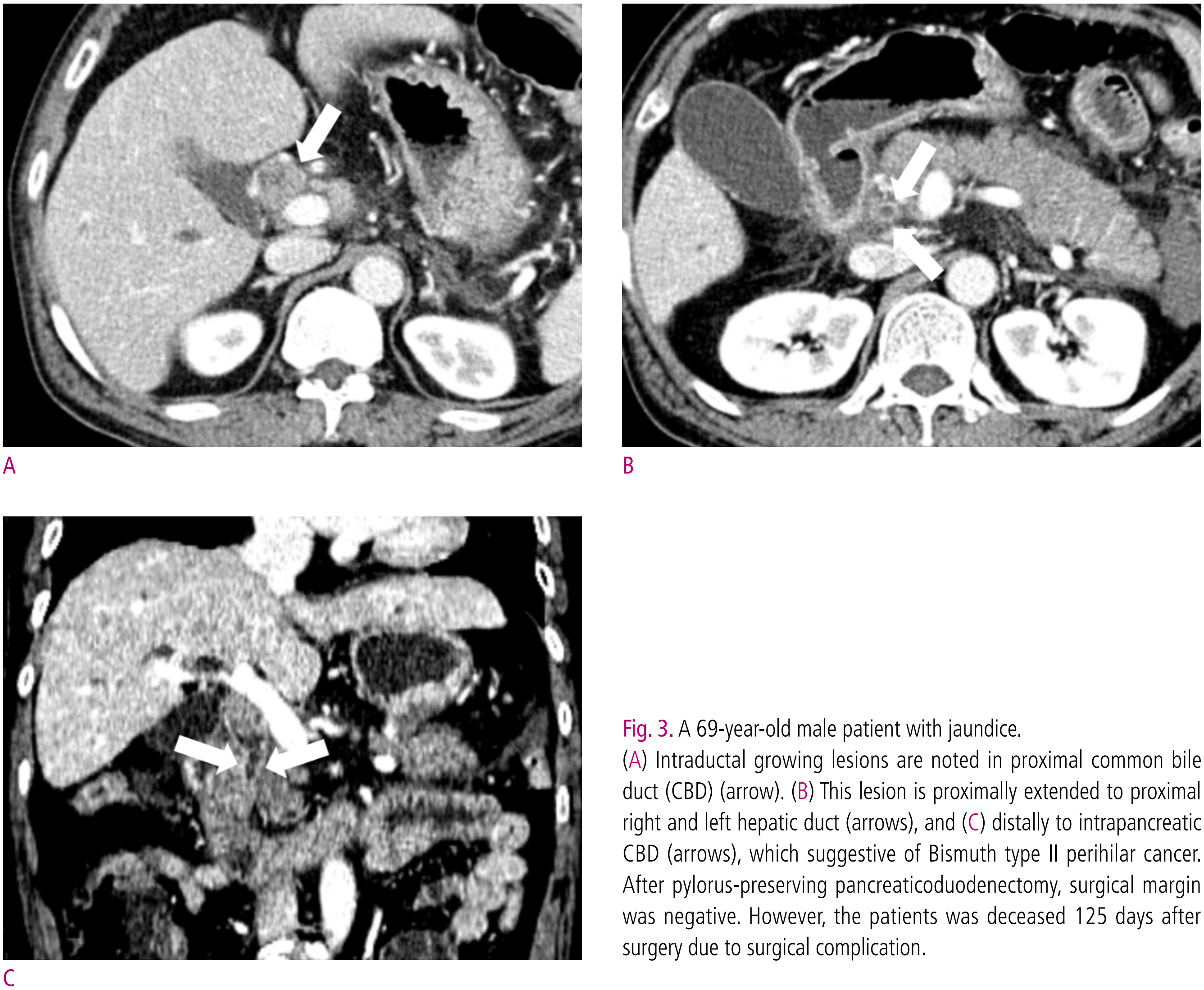

Fig. 3. A 69-year-old male patient with jaundice.
(A) Intraductal growing lesions are noted in proximal common bile duct (CBD) (arrow). (B) This lesion is proximally extended to proximal right and left hepatic duct (arrows), and (C) distally to intrapancreatic CBD (arrows), which suggestive of Bismuth type II perihilar cancer. After pylorus-preserving pancreaticoduodenectomy, surgical margin was negative. However, the patients was deceased 125 days after surgery due to surgical complication.

We also found that the diagnostic ability of pre-operative CT for mid-CBD involvement was 0.71 (AUC value) with 87.2% sensitivity and 55.5% specificity. In addition, a likelihood score of 4 or 5 for mid-CBD involvement on pre-operative CT predicts 92.9% of distal margin positive resection. These results are easily explainable as when the tumor involves distally, the surgeon have to decide whether undergo pancreaticoduodenectomy together or not. However, combining operation of pancreaticoduodenectomy and hilar resection, the one of major surgery, may not easy to determine due to increased morbidity and mortality of operation. Thus, only some patients are allowed to undergo combining pancreaticoduodenectomy.

For survival analysis, intrapancreatic CBD involvement was the independent predictor for poor survival. Our hypothesis of this result is the intrapancreatic CBD involvement in pre-operative CT relates to high tumor burden. Another possible hypothesis is that broad surgery extent such as pancreaticoduodenectomy when intrapancreatic CBD involvement is suspected, increase mortality and morbidity of the surgery. However, in our study, extended surgery is not a significant factor for overall survival.

The diagnostic ability of pre-operative CT for intrapancreatic CBD involvement was 0.72 (AUC value) with 60.0% sensitivity and 91.6% specificity. These results were in good agreement with the results of a previous study showing the 82% accuracy to assess the distal border of the tumor using pre-operative CT examination

Table 3. Summary of important clinical and CT findings for overall survival after surgery in perihilar cancer

	Univariable analysis				Multivariable analysis	
	No.	Median survival (mo)	P	Interobserver agreement	Hazard ratio	P
Sex			0.42	N/A		
Men	82	25.4 (17.4, 35.0)				
Women	57	24.7 (13.9, 32.1)				
T.bil			0.03	N/A	1.53 (1.02, 2.29)[†]	0.04
≤ 1.2 mg/dL	50	34.3 (15.4, 53.2)				
> 1.2 mg/dL	89	21.5 (14.9, 28.2)				
CEA			0.62	N/A		
< 5 ng/mL	124	24.5 (17.1, 31.8)				
> 5 ng/mL	15	27.0 (18.0, 35.9)				
CA 19-9			0.02	N/A	1.75 (1.12, 2.65)[†]	<0.01
≤ 37 U/mL	54	39.0 (19.7, 58.2)				
> 37 U/mL	84	21.9 (17.5, 26.3)				
Operation extent						
Hepatic resection	74	24.5 (19.7, 31.6)	0.34	N/A		
Pancreaticoduodenectomy	7	53.2 (9.44, 70.3)	0.16	N/A		
Radiologic variables						
BD 1st order			0.37	0.63		
Negative	14	31.8 (21.8, 41.8)				
Positive	125	24.8 (19.7, 29.9)				
BD 2nd order			0.07	0.67	1.18 (0.77, 1.82)[†]	0.45
Negative	45	35.7 (19.4, 52.0)				
Positive	94	21.9 (17.2, 26.6)				
Mid CBD			0.32	0.73*		
Negative	43	27.0 (18.4, 35.6)				
Positive	96	23.7 (14.8, 32.6)				
Intrapancreatic CBD			<0.01	0.83*	1.81 (1.03, 3.16)[†]	0.04
Negative	124	26.2 (20.2, 32.3)				
Positive	15	11.4 (2.0, 20.9)				
RHA			0.09	0.35	1.34 (0.91, 1.96)[†]	0.14
Negative	75	29.7 (21.8, 37.5)				
Positive	64	20.0 (12.8, 27.2)				
LHA			0.32	0.52		
Negative	128	26.2 (19.7, 32.8)				
Positive	11	18.5 (7.7, 29.4)				
RPV			0.90	0.21		
Negative	138	25.0 (18.5, 31.4)				
Positive	1	43.9 (N/A)				
LPV			0.22	0.74		
Negative	107	25.0 (18.4, 31.6)				
Positive	5	33.4 (0.1, 70.5)				

Continued

Table 3. Continued

	Univariable analysis				Multivariable analysis	
	No.	Median survival (mo)	P	Interobserver agreement	Hazard ratio	P
LN			0.54	0.35		
Negative	71	31.8 (22.2, 41.4)				
Indeterminate	59	3.3 (17.9, 31.0)				
Positive	9	3.7 (7.5, 21.9)				
Peritumoral fat infiltration			0.19	0.47*		
Negative	109	27.0 (20.2, 33.8)				
Positive	30	16.4 (10.8, 22.1)				

Note.- Values in parentheses are 95%CI; * indicate ICC values. † Values in parentheses are 95%CI.

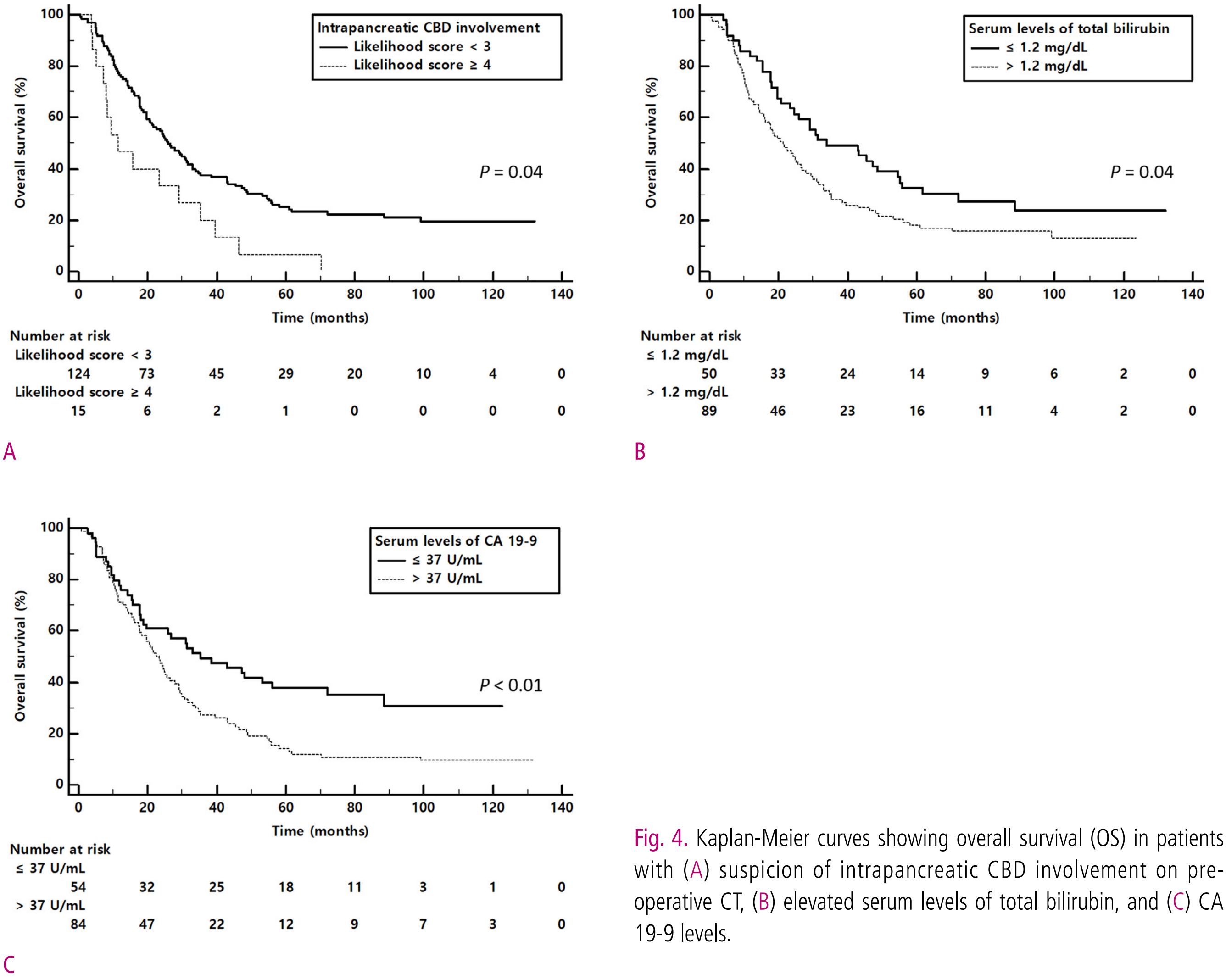

Fig. 4. Kaplan-Meier curves showing overall survival (OS) in patients with (A) suspicion of intrapancreatic CBD involvement on preoperative CT, (B) elevated serum levels of total bilirubin, and (C) CA 19-9 levels.

(31). In addition, the interobserver agreements of intrapancreatic CBD (ICC = 0.83) and mid-CBD (ICC = 0.73) on pre-operative CT were high which are crucial for consistent pre-operative planning. Thus, we cautiously suggest that evaluating the distal extent of perihilar cholangiocarcinoma using pre-operative CT is feasible for resectability evaluation and patient's survival.

In our study, elevated serum levels of CA 19-9 (> 37U/mL $p < 0.01$) and total bilirubin (> 1.2 mg/dL, $p = 0.04$) were the independent prognostic factors for poor overall survival. Although CA 19-9 is a well known diagnostic marker for cholangiocarcinoma, whether it can be used as a prognostic marker has not been studied. Recently, however, a few studies have been reported CA 19-9 as a potential prognostic marker. Chaiteerakij et al. (32) proposed the CA 19-9 level of 1000 U/mL or more as the variables in perihilar cancer staging system. Oguro et al. (33) reported that CA 19-9 level of 64 U/mL or more was the significant factor for poor overall survival with hazard ratio of 1.9. Also in our study revealed that the elevated serum level of total bilirubin in pre-operative period was an independent predictor for poor survival. Our results are well in line with a previous study of Koerkamp et al. (34) which had reported the total bilirubin level of 2 mg/dL or more was the significant factor for poor 5-year recurrence free survival. One of plausible explanation of this results is that the pre-operative level of total bilirubin may reflect the severity of disease, even with the appropriate intervention to lower bilirubin level.

In our study, vascular invasion is not a significant factor for resectability assessment. This results are not consistent with previous studies stated vascular invasion as a poor prognostic factor (4, 29). The discrepancy is explainable as our study population are limited for those who are possible curative-intent surgery and well-known contraindicated cases such as contralateral artery or portal vein invasion (29) were excluded. When the vessel involvement is in the operable ranges for curative intent surgery, vascular involvement did not influence resectability and patient's survival.

There are several limitations in our study. First, owing to the nature of single center based retrospective study, selection bias was not avoidable. Second, their resectability might be influenced by surgeon's propensity. However, as one of big centers undergoing operation for perihilar cholangiocarcinoma about 50 cases per year, our hospital have followed standard treatment strategy based on multi-disciplinary approach. Thus, the effect of surgeon's propensity would be minimized.

In conclusion, mid-CBD involvement on pre-operative CT is significant factor for margin positive resection on curative intent surgery and intrapancreatic CBD involvement is significant factor for poor survival. Therefore, distal longitudinal extent of perihilar cancer on pre-operative CT would be an important factor for margin positive resection and poor survival on curative intent surgery.

References

1. Nakeeb A, Pitt HA, Sohn TA, Coleman J, Abrams RA, Piantadosi S, et al. Cholangiocarcinoma. A spectrum of intrahepatic, perihilar, and distal tumors. Annals of surgery 1996;224:463.
2. Park J, Kim M-H, Kim K-p, Park DH, Moon S-H, Song TJ, et al. Natural history and prognostic factors of advanced cholangiocarcinoma without surgery, chemotherapy, or radiotherapy: a large-scale observational study. Gut and liver 2009;3:298.
3. Popescu I, Dumitrascu T. Curative-intent surgery for hilar cholangiocarcinoma: prognostic factors for clinical decision making. Langenbeck's archives of surgery 2014;399:693-705.
4. Klempnauer J, Ridder GJ, Von Wasielewski R, Werner M, Weimann A, Pichlmayr R. Resectional surgery of hilar cholangiocarcinoma: a multivariate analysis of prognostic factors. Journal of Clinical Oncology 1997;15:947-954.
5. Lee SG, Song GW, Hwang S, Ha TY, Moon DB, Jung DH, et al. Surgical treatment of hilar cholangiocarcinoma in the new era: the Asan experience. Journal of hepato-biliary-pancreatic sciences 2010;17:476-489.
6. Nuzzo G, Giuliante F, Ardito F, Giovannini I, Aldrighetti L, Belli G, et al. Improvement in perioperative and long-term outcome after surgical treatment of hilar cholangiocarcinoma: results of an Italian multicenter analysis of 440 patients. Archives of surgery 2012;147:26-34.
7. Neuhaus P, Jonas S, Settmacher U, Thelen A, Benckert C, Lopez-Hanninen E, et al. Surgical management of proximal bile duct cancer: extended right lobe resection increases resectability and radicality. Langenbeck's archives of surgery

2003;388:194-200.

8. de Wilde RF, Koerkamp BG. Radial margin status should be determined in resected perihilar cholangiocarcinoma. Hepatobiliary surgery and nutrition 2019;8:557.
9. Shinohara K, Ebata T, Shimoyama Y, Mizuno T, Yokoyama Y, Yamaguchi J, et al. A Study on Radial Margin Status in Resected Perihilar Cholangiocarcinoma. Annals of surgery 2019.
10. Mizuno T, Ebata T, Nagino M. Advanced hilar cholangiocarcinoma: An aggressive surgical approach for the treatment of advanced hilar cholangiocarcinoma: Perioperative management, extended procedures, and multidisciplinary approaches. Surgical oncology 2019.
11. Bednarsch J, Czigany Z, Lurje I, Tacke F, Strnad P, Ulmer TF, et al. Left-versus right-sided hepatectomy with hilar en-bloc resection in perihilar cholangiocarcinoma. HPB 2019.
12. Nagino M, Ebata T, Yokoyama Y, Igami T, Sugawara G, Takahashi Y, et al. Evolution of surgical treatment for perihilar cholangiocarcinoma: a single-center 34-year review of 574 consecutive resections. Annals of surgery 2013;258:129-140.
13. Peng D-Z, Lu J, Li B, Hu H-J, Ye X-W, Xiong X-Z, et al. A simple scoring system to predict early recurrence of Bismuth-Corlette type IV perihilar cholangiocarcinoma. Gastroenterology report 2019;7:345-353.
14. Lee HY, Kim SH, Lee JM, Kim S-W, Jang J-Y, Han JK, et al. Preoperative assessment of resectability of hepatic hilar cholangiocarcinoma: combined CT and cholangiography with revised criteria. Radiology 2006;239:113-121.
15. Kambakamba P, DeOliveira ML. Perihilar cholangiocarcinoma: paradigms of surgical management. The American Journal of Surgery 2014;208:563-570.
16. Millon D, Vlassenbroek A, Van Maanen AG, Cambier SE, Coche EE. Low contrast detectability and spatial resolution with model-based Iterative reconstructions of MDCT images: a phantom and cadaveric study. European radiology 2017;27:927-937.
17. Solomon J, Marin D, Roy Choudhury K, Patel B, Samei E. Effect of radiation dose reduction and reconstruction algorithm on image noise, contrast, resolution, and detectability of subtle hypoattenuating liver lesions at multidetector CT: filtered back projection versus a commercial model-based iterative reconstruction algorithm. Radiology 2017;284:777-787.
18. McCollough CH, Yu L, Kofler JM, Leng S, Zhang Y, Li Z, et al. Degradation of CT low-contrast spatial resolution due to the use of iterative reconstruction and reduced dose levels. Radiology 2015;276:499-506.
19. Choi S-Y, Kim JH, Park HJ, Han JK. Preoperative CT findings for prediction of resectability in patients with gallbladder cancer. European radiology 2019;29:6458-6468.
20. Bae JS, Kim JH, Joo I, Chang W, Han JK. MDCT findings predicting post-operative residual tumor and survival in patients with pancreatic cancer. European radiology 2019;29:3714-3724.
21. Choi SH, Han JK, Lee JM, Lee KH, Kim SH, Lee JY, et al. Differentiating malignant from benign common bile duct stricture with multiphasic helical CT. Radiology 2005;236:178-183.
22. Joo I, Lee JM, Yoon JH. Imaging diagnosis of intrahepatic and perihilar cholangiocarcinoma: recent advances and challenges. Radiology 2018;288:7-13.
23. Thornton E, Mendiratta-Lala M, Siewert B, Eisenberg RL. Patterns of fat stranding. American Journal of Roentgenology 2011;197:W1-W14.
24. Tamm EP, Balachandran A, Bhosale PR, Katz MH, Fleming JB, Lee JH, et al. Imaging of pancreatic adenocarcinoma: update on staging/resectability. Radiologic Clinics 2012;50:407-428.
25. Huang T. Variants of the bile ducts: clinical application in the potential donor of living related hepatic transplantation. Transplant Proc 1996;28:1669-1670.
26. Bismuth H, Nakache R, Diamond T. Management strategies in resection for hilar cholangiocarcinoma. Annals of surgery 1992;215:31.
27. Engels JT, Balfe DM, Lee J. Biliary carcinoma: CT evaluation of extrahepatic spread. Radiology 1989;172:35-40.
28. Boudjema K, Sulpice L, Garnier S, Bretagne JF, Gandon Y, Rohou T. A simple system to predict perihilar cholangiocarcinoma resectability. J Gastrointest Surg 2013;17:1247-1256.
29. DeOliveira ML, Schulick RD, Nimura Y, Rosen C, Gores G, Neuhaus P, et al. New staging system and a registry for perihilar cholangiocarcinoma. Hepatology 2011;53:1363-1371.
30. Miyazaki M, Kato A, Ito H, Kimura F, Shimizu H, Ohtsuka M, et al. Combined vascular resection in operative resection for hilar cholangiocarcinoma: does it work or not? Surgery 2007;141:581-588.
31. Senda Y, Nishio H, Oda K, Yokoyama Y, Ebata T, Igami T,

et al. Value of multidetector row CT in the assessment of longitudinal extension of cholangiocarcinoma-correlation between MDCT and microscopic findings. World journal of surgery 2009;33:1459-1467.

32. Chaiteerakij R, Harmsen WS, Marrero CR, Aboelsoud MM, Ndzengue A, Kaiya J, et al. A new clinically based staging system for perihilar cholangiocarcinoma. The American journal of gastroenterology 2014;109:1881.
33. Oguro S, Esaki M, Kishi Y, Nara S, Shimada K, Ojima H, et al. Optimal indications for additional resection of the invasive cancer-positive proximal bile duct margin in cases of advanced perihilar cholangiocarcinoma. Annals of Surgical Oncology 2015;22:1915-1924.
34. Koerkamp BG, Wiggers JK, Allen PJ, Besselink MG, Blumgart LH, Busch OR, et al. Recurrence rate and pattern of perihilar cholangiocarcinoma after curative intent resection. Journal of the American College of Surgeons 2015;221:1041-1049.

Appendix 1. CT parameters

Parameters	Brilliance (n=63)	Sensation (n=35)	Definition (n=18)	Lightspeed ultra (n=10)	Discovery (n=10)	Aquilion one (n=3)
No. of channels	64	16	64	16	64	320
Section thickness (mm)	2.5-3.0	3	2.5-3.0	2.5	2.5	3
Reconstruction interval (mm)	2.0-3.0	2.0-3.0	2.0-3.0	2.0	2.5	2
Pitch	0.9-1.2	1.0-1.5	2.0	0.75-0.88	2.0	0.813
Rotation time (sec)	0.75	0.5	0.5	0.5-0.6	0.35	0.5
Tube current (mAs)	180	160	160	180	285	150
Tube voltage (kVp)	120	120	120	120	120	120
Matrix	512 x 512	512 x 512	512 x 512	512 x 512	512 x 512	512 x 512

Note.—The following CT machines were used: Brilliance (Philips Healthcare, Best, the Netherlands), Sensation (Siemens Healthcare, Erlangen, Germany), Somatom Definition (Siemens Healthcare), Lightspeed ultra (GE Healthcare, Milwaukee, WI), Discovery CT750 (GE Healthcare), and Aquilion One (Canon Medical Systems, Otawara, Japan).

완치 목적의 perihilar cholangiocarcinoma 수술 전 불완전 절제 및 불량한 예후 예측을 위한 CT 소견

강효진[1,2], 김정훈[1,2], 주이진[1,2], 장원[2,3]

[1]서울대학교병원 영상의학과, [2]서울대학교 의과대학 영상의학교실, [3]분당서울대학교병원 영상의학과

목 적: Perihilar cholangiocarcinoma의 불완전 절제 (R1 혹은 R2) 및 불량한 예후 예측을 위한 수술 전 CT 영상 소견을 평가하고자 한다.

방 법: 2006에서 2012년까지 완치 목적의 수술을 받은 총 139명의 perihilar cholangiocarcinoma 환자의 수술 전 다중 CT 영상을 분석하였다. 두 명의 영상의학의사가 췌장 내 담도에서 담도 2차 분지지점까지 각 구간 별 종양의 침범 여부 및 병변 주변 지방 침범 가능성 (likelihood)를 5점 기준으로 평가하였고, 혈관 침범 (없음, 닿음, 둘러쌈), 및 림프절 침범 여부도 평가하였다. 각 영상 소견은 독립적으로 검토 후 합의 과정을 통해 최종 결정하였다. 수술 전 CT 상의 담도 침범 소견을 likelihood 점수 4점이상으로 하였을 때, 이 기준의 진단능을 병리 소견과 비교하여 receiver operating curve로 분석하였다. 절제 후 병리는 완전 절제 (R0)와 불완전 절제 (R+; R1 혹은 R2)로 분류하였다. 수술 전 CT 영상에서 불완전 절제의 예측 인자 확인을 위해 로지스틱 회귀분석이 사용되었다. 수술 전 CT 영상 및 혈액검사 소견을 통한 생존율 예측 인자 확인을 위해 Cox의 비례위험모형을 사용하였다.

결 과: 71명의 환자는 완전 절제, 68명의 환자는 불완전 절제가 되었다. 절제 가능성 평가에서는, 다변수 로지스틱 회귀분석에서 수술 전 영상에서 총 담관 중간부 침범 (likelihood score ≥ 4)이 불완전 절제의 유의한 소견이었다 ($p < 0.01$). 다변수 Cox 비례위험모형 분석에서는, 췌장 내 담도 침범 (likelihood score ≥ 4, hazard ratio = 1.81, $p < 0.01$), 총 빌리루빈 상승 (hazard ratio = 1.53, $p < 0.04$), CA19-9 (hazard ratio = 1.75, $p < 0.01$)가 불량한 예후를 예측하는 유의미한 인자였다. 수술 전 CT를 이용한 총 담관 중간부 침범과 췌장 내 담도 침범 정확도는 각각 0.71과 0.72 (AUC 값) 이다.

결 론: 수술 전 CT에서 perihilar cholangiocarcinoma의 원위부 침범 소견은 불완전 절제 및 불량한 예후를 예측하는데 유의미한 소견이다.

www.e-kjar.org
https://doi.org/10.52668/kjar.2022.00164

pISSN 2586-1719 / eISSN 2799-3299
Copyright © The Korean Society of Abdominal Radiology

Korean J Abdom Radiol 2022;6:51-56

Case Report

Hepatic and Extrahepatic Fascioliasis Mimicking Colon Cancer with Hepatic Metastasis

Youe Ree Kim, Young Hwan Lee, Kwon-Ha Yoon
Department of Radiology, Wonkwang University College of Medicine and Hospital, Iksan, Korea

Fascioliasis hepatica is a rare parasitic infection affecting the hepatobiliary system. On the imaging examination, it presents as multiple hepatic abscesses and bile duct dilatation. Extrahepatic fascioliasis of the gastrointestinal tract is a rare condition, resulting from the duodenal migration of fasciola flukes. The current case showed both hepatic and colonic masses, mimicking colon cancer with hepatic metastasis. However, diagnostic clues from multimodality approaches, especially in combination with magnetic resonance imaging, led to an accurate diagnosis of hepatic and extrahepatic fascioliasis.

Keywords: Liver; Colon; Fascioliasis; Parasitic Diseases; Magnetic resonance imaging

Introduction

Fascioliasis is a rare parasitic infection of the hepatobiliary system caused by *Fasciola hepatica* and *Fasciola gigantica*. Symptoms include abdominal pain in the right upper quadrant, obstructive jaundice, and cholangitis (1, 2). Extrahepatic manifestations are rare and have been reported in the subcutaneous tissue, brain, lungs, epididymis, and colon (3-6). When extrahepatic fascioliasis appears as a tumor in the colon, malignancy can be mimicked, making it difficult to diagnose preoperatively (5, 6). Herein, we report a case of hepatic and extrahepatic fascioliasis mimicking colon cancer with hepatic metastasis, in the form of multiple masses in the transverse colon and liver.

Case Report

A 60-year-old man visited our hospital for the evaluation of malignancy. He had experienced vague abdominal pain for 20 days. Laboratory findings showed elevated C-reactive protein (34.97 mg/L), normal white blood cell count (9450/μL), and eosinophilia (3450/μL, 36.5%). Tumor markers of carbohydrate antigen (CA) 19-9 and carcinoembryonic antigen (CEA) levels were within the normal range (CA 19-9, 4.0 U/mL; CEA, 0.61 ng/mL).

Abdominal computed tomography (CT) axial (Fig. 1A) and coronal (Fig. 1B) portal phase images showed irregular circumferential edematous wall thickening at the hepatic flexure of the colon. Extensive fat infiltration and edema were noted in the transverse mesocolon and greater omentum, and a small amount of ascites was observed. An axial CT portal image of the caudal

Received: March 31, 2022 **Revised:** May 11, 2022 **Accepted:** May 11, 2022
Correspondence: Young Hwan Lee, MD, PhD
Department of Radiology, Wonkwang University College of Medicine and Hospital, 895 Muwang-ro, Iksan, Jeollabuk-do, 54538, Korea
Tel: +82-63-859-1920 Fax: +82-63-851-4749 E-mail: yjyh@wku.ac.kr
This is an Open Access article distributed under the terms of the Creative Commons Attribution Non-Commercial License (http://creativecommons.org/licenses/by-nc/4.0/) which permits unrestricted non-commercial use, distribution, and reproduction in any medium, provided the original work is properly cited.

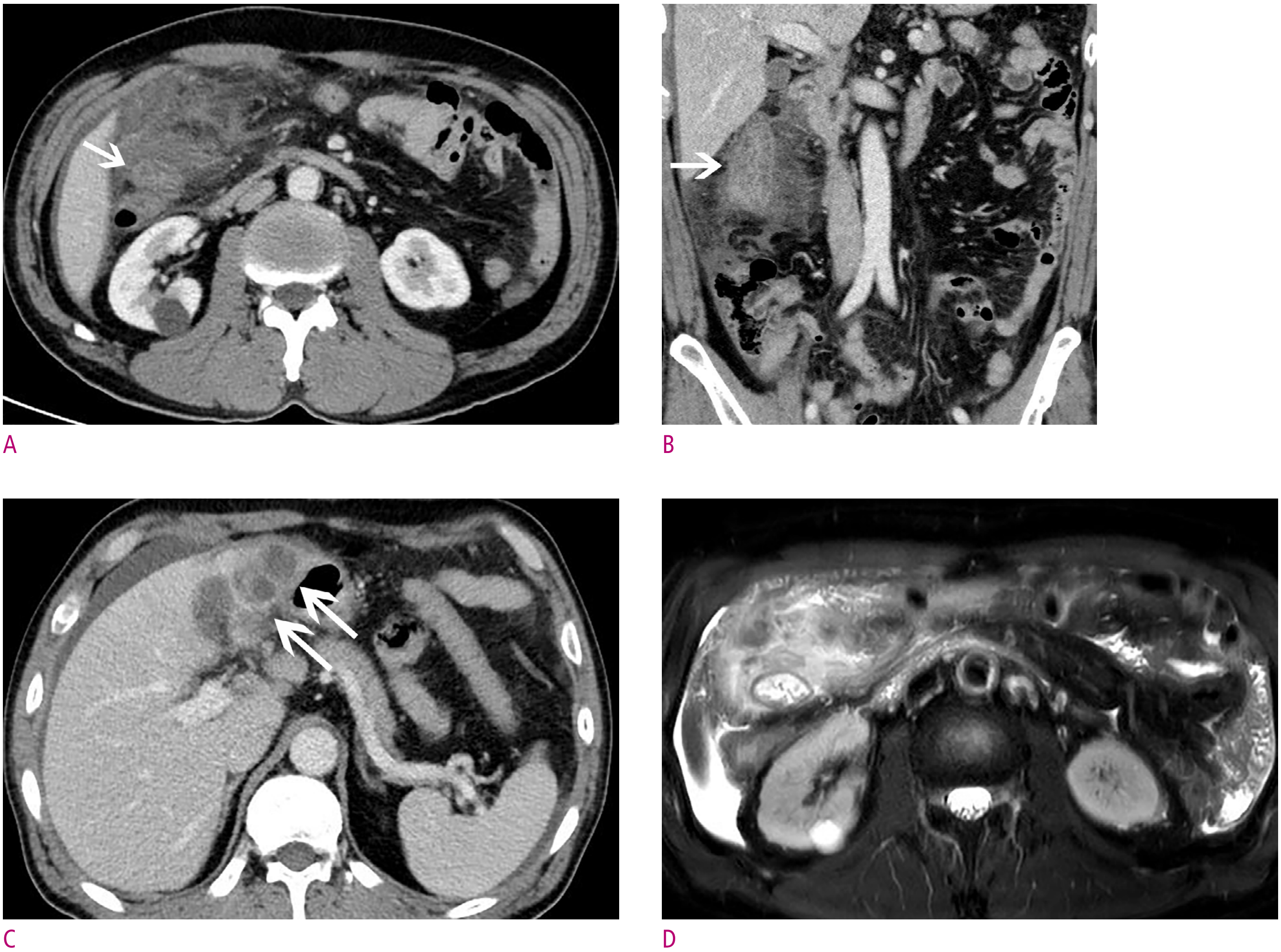

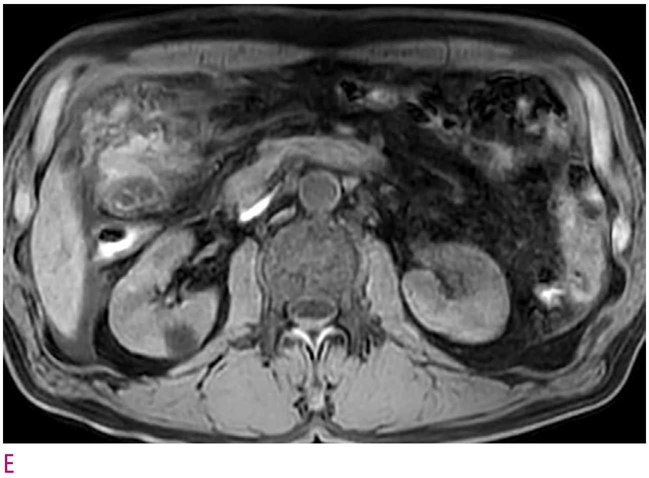

Fig. 1. A 60-year-old male patient with hepatic and extrahepatic fascioliasis.

A, B. Axial (A) and coronal (B) computed tomography (CT) portal phase images showing irregular circumferential edematous wall thickening at the hepatic flexure of the colon (arrow). Extensive infiltration and edema were noted in the transverse mesocolon and greater omentum, and a small amount of ascites were observed. C. Axial CT portal image showing multiple hypodense hepatic masses with an enhancing solid portion (arrows) at the left hepatic lobe and the fissure for ligamentum teres. D. Magnetic resonance imaging (MRI) revealed axial fat-suppressed T2-weighted images showing circumferential T2 hyperintense wall thickening of the transverse colon and diffuse hyperintensity and fluid at the omentum and transverse mesocolon. E. Axial fat-suppressed T1-weighted image showing diffuse hyperintensity in the omentum and transverse mesocolon, suggesting a hemorrhage.

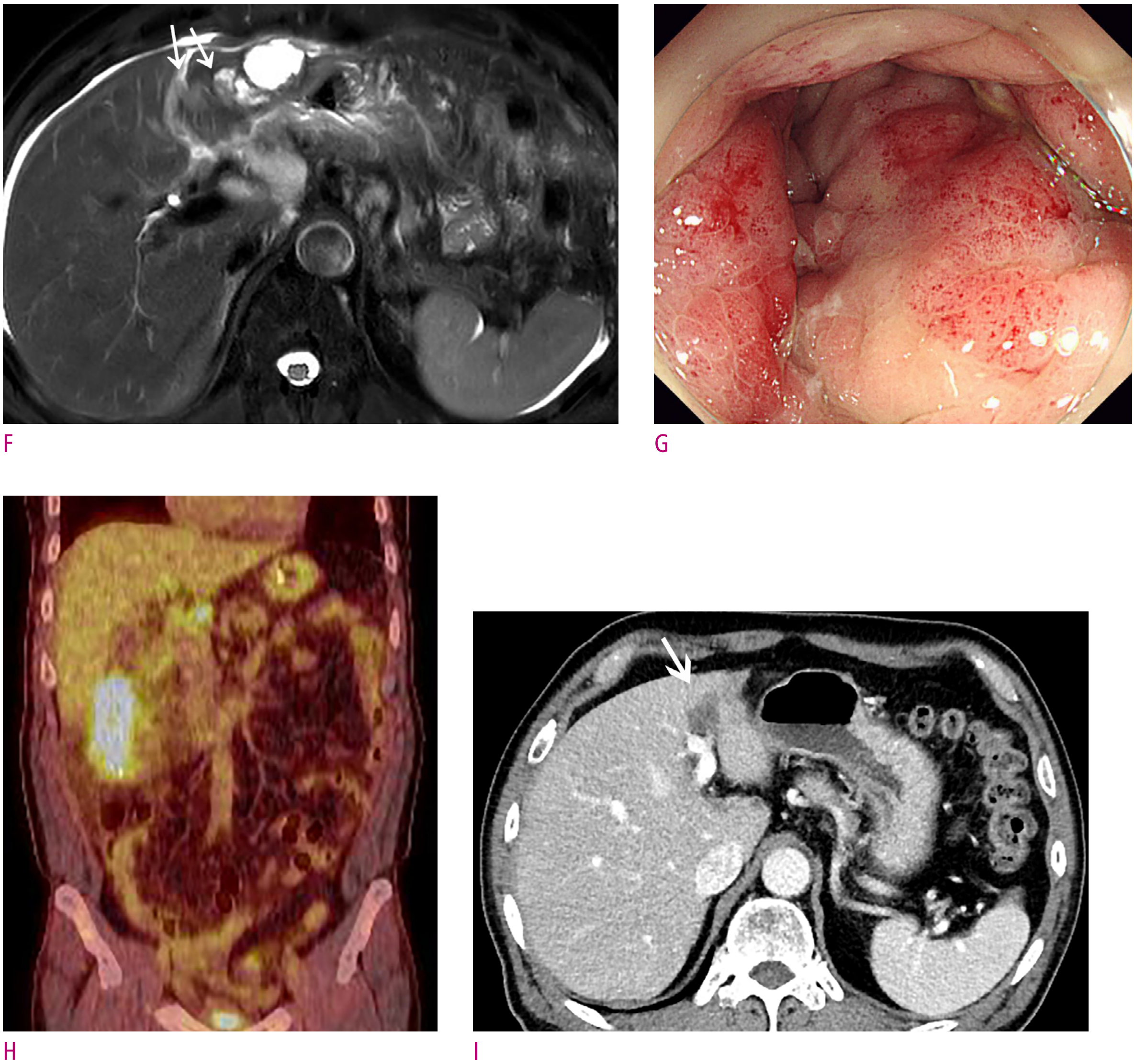

Fig. 1. F. Axial fat-suppressed T2-weighted image showing multiple T2 bright hyperintense masses with internal intermediate signal intensity nodules in the left lobe of the liver and the fissure of the ligamentum teres (arrows). G. Colonoscopy image revealed a large infiltrative mass with ulcer and luminal obstruction. H. Positron emission tomography/computed tomography revealed a high standardized uptake value (maximum 6.9) for both the colon and liver lesions. I. Axial CT portal phase image showing disappearance of hepatic lesions and remaining periportal hypointense lesions without enhancement at the fissure for the ligamentum teres (arrow). J. Coronal CT portal phase image showing improved wall thickening of the transverse colon.

side (Fig. 1C) showed multiple hypodense masses with an enhancing solid portion in the left hepatic lobe. The lesions were clustered in segment 3 and the fissure for the ligamentum teres. The initial diagnosis was mucinous colon cancer with microperforation and cystic hepatic metastasis. The differential diagnosis was severe colitis and hepatic abscess. On further evaluation using magnetic resonance imaging (MRI), the axial fat-suppressed T2 weighted image (Fig. 1D) showed circumferential T2 hyperintense wall thickening with a uniform layer of the transverse colon. Diffuse T2 hyperintense fat and perilesional fluid in the omentum and transverse mesocolon were noted, suggesting extensive edema and inflammation. Axial fat-suppressed T1 weighted image (Fig. 1E) showed a diffuse hyperintense signal of the omentum and transverse mesocolon, suggesting hemorrhage. Axial fat-suppressed T2 weighted image (Fig. 1F) showed multiple T2 bright hyperintense masses with internal intermediate signal intensity nodules in the left hepatic lobe. Tiny cystic lesions were observed along the fissure of the ligamentum teres. Linear elongated hyperintense foci along the periportal area and tram-track sign were observed. A tentative diagnosis from CT and MRI was parasitic infection with liver and colon involvement.

Colonoscopy (Fig. 1G) revealed a large infiltrative mass with ulceration and luminal obstruction, suggesting colon cancer. However, the biopsy result after pathological review revealed nonspecific inflammation. Positron emission tomography/computed tomography (PET/CT) imaging (Fig. 1H) revealed a high standardized uptake value (SUV) (maximum 6.9) in both colon and liver lesions, suggesting colon cancer with liver metastasis. Owing to the discordant workup results, a multidisciplinary approach was employed. Using ultrasound-guided aspiration of the liver lesion, a yellowish material was aspirated. A *Fasciola hepatica* eggs was detected. The serum *Fasciola hepatica* antibody test results were positive. After treatment with triclabendazole, the treatment of choice for fascioliasis, colon and liver lesions were improved by a follow-up abdominal CT scan (Fig. 1I, J).

Discussion

Fascioliasis is a zoonotic trematode infection caused by *Fasciola hepatica* and *Fasciola gigantica*, with *Fasciola hepatica* infection being the most common type of infection (7). The endemic areas of human fascioliasis are South America, North Africa, and the Middle East, and cases are sporadically reported in Korea (2, 7, 8). Freshwater snails are intermediate hosts, and mammals, including humans, are definitive hosts (1). When encysted larvae from contaminated water are ingested by humans, the larvae penetrate the duodenal wall, enter the liver through the peritoneum and Glisson's capsule, and settle in the bile duct or gallbladder (1, 10).

The two stages in which the larvae infect the liver and cause symptoms are broadly divided into hepatic (acute) and biliary (chronic) (8, 9). In the hepatic stage, the main symptoms are urticaria, abdominal pain, and fever, and in the biliary stage, intermittent abdominal pain and cholangitis or cholestasis are accompanied (9, 10). Similarly, it is divided into the parenchymal and ductal phases in radiology (1). In the parenchymal phase, multiple microabscesses are seen at the migration site of the larva, and a tunnel-like tract is seen at the entry site of Glisson's capsule (8, 10). Upon penetration of the parenchyma, clustered abscesses appear as caves with a serpentine pattern. The 'tunnels and caves' sign observed on CT can be a characteristic sign of hepatic fascioliasis (9, 10). In the ductal phase, at 8 weeks, a dilated biliary duct with portal tract thickening is observed. Calcifications of the subcapsular area can be observed after 10 weeks (1).

There have been reports of extrahepatic fascioliasis in the GI tract, including the colon, cecum, and transverse mesocolon (2, 5, 6, 11, 12). Colon involvement is thought to be caused by the migration of penetrating larvae through the duodenal wall to a location other than the liver through the peritoneum or mesentery (1). In this case, a mass in the proximal transverse colon was formed, accompanied by severe inflammation in the surrounding transverse mesocolon and greater omentum. CT showed increased fat density, fascial thickening, and perilesional fluid, and MRI showed T2 hyperintensity and bright high-signal intensity lesions, suggesting fluid collection and edema. One of the interesting points in this case was the T1 hyperintensity of the omentum and transverse mesocolon, suggesting hemorrhage. To the best of our knowledge, there are no reports of MRI findings of extrahepatic fascioliasis or T1 hyperintensity of the omentum and mesentery. However, there is a study reporting an MRI finding of T1 hyperintensity caused by larval penetration of the liver capsule, therefore we believe that the hyperintensity of peritoneal fat is likely due to the migration of the Fasciola larvae (1).

Even when only the liver lesion exists, malignancy such as cholangiocarcinoma can be mimicked (13), but it is relatively easy to diagnose hepatic fascioliasis through clinical symptoms, eosinophilia, and serum antibody (1, 8). However, in this case, the diagnosis of colon cancer with hepatic metastasis was considered the initial differential CT diagnosis due to the simultaneous involvement of hepatic and extrahepatic fascioliasis, showing liver and colon lesions simultaneously. In particular, CT, endoscopy, and PET/CT showed diagnostic findings mimicking malignancy, such as colon mass with multiple liver masses, infiltrative colon mass with obstruction, and high F18-fluorodeoxyglucose uptake of those lesions, respectively. However, the MRI findings were helpful in the differential diagnosis. T2 bright high-signal intensity microabscesses in the liver parenchyma, 'Tunnels and caves' sign in the subcapsular and peribiliary areas, T2 hyperintense wall thickening with a uniform layered pattern of the colon, severe edematous changes, and hemorrhage of the omentum and transverse mesocolon helped diagnose hepatic and extrahepatic fascioliasis. In the previous case reports, there were cases in which colon cancer was mimicked, and surgical excision was performed (5, 6). The combination of multimodality imaging helped diagnose the disease, and unnecessary surgical intervention was prevented in this case.

In conclusion, in cases of multiple cystic masses in the liver, a colon mass with poor enhancement, and severe inflammation in the surrounding omentum and mesentery, parasitic infection, specifically hepatic and extrahepatic fascioliasis, should be considered as the first diagnostic impression.

References

1. Dusak A, Onur MR, Cicek M, Firat U, Ren T, Dogra VS. Radiological Imaging Features of Fasciola hepatica Infection - A Pictorial Review. J Clin Imaging Sci 2012;2:2.
2. Kim AJ, Choi CH, Choi SK, Shin YW, Park YK, Kim L, et al. Ectopic Human Fasciola hepatica Infection by an Adult Worm in the Mesocolon. Korean J Parasitol 2015;53:725-730.
3. Aguirre Errasti C, Merino Angulo J, Flores Torres M, de los Rios A. Unusual forms of Fasciola hepatica infestation. Report of two cases. Med Clin (Barc) 1981;76:125-128.
4. Ruggieri F, Correa AJ, Martinez E. Cerebral distomiasis. Case report. J Neurosurg 1967;27:268-271.
5. Makay O, Gurcu B, Caliskan C, Nart D, Tuncyurek M, Korkut M. Ectopic fascioliasis mimicking a colon tumor. World J Gastroenterol 2007;13:2633-2635.
6. Akbulut S, Ozdemir E, Samdanci E, Unsal S, Harputluoglu M, Yilmaz S. Fascioliasis presenting as colon cancer liver metastasis on 18F-fluorodeoxyglucose positron emission tomography/computed tomography: a case report. World J Hepatol 2019;11:656-662.
7. Nyindo M, Lukambagire AH. Fascioliasis: an Ongoing Zoonotic Trematode Infection. Biomed Res Int 2015;2015:786195.
8. Cantisani V, Cantisani C, Mortelé K, Pagliara E, D'Onofrio M, Fernandez M, et al. Diagnostic imaging in the study of human hepatobiliary fascioliasis. Radiol Med 2010;115:83-92.
9. Ünal E, Arslan S, Onur MR, Akpinar E. Parasitic diseases as a cause of acute abdominal pain: imaging findings. Insights Imaging 2020;11:86.
10. Salahshour F, Tajmalzai A. Imaging findings of human hepatic fascioliasis: a case report and review of the literature. J Med Case Rep 2021;15:324.
11. Lee SH, Cho SY, Seo BS, Choe KJ, Chi JG. A human case of ectopic fascioliasis in Korea. Korean J Parasitol 1982;20:191-200.
12. Park CI, Kim H, Ro JY, Gutierrez Y. Human ectopic fascioliasis in the cecum. Am J Surg Pathol 1984;8:73-77.
13. Kim YH, Kang KJ, Kwon JH. Four cases of hepatic fascioliasis mimicking cholangiocarcinoma. Korean J Hepatol 2005;11:169-175.

대장암과 간전이암을 모방한 간내 및 간외 간질증

김유리, 이영환, 윤권하

원광대학교 의과대학, 원광대학교병원 영상의학과

초 록

Fascioliasis hepatica는 간담도계의 감염을 일으키는 드문 기생충으로, 이에 감염될 경우 영상 검사에서 다발성 간 농양과 담관 확장 등을 보인다. 위장관의 간외 간질증은 드물며 fasciola 흡충이 십이지장을 뚫고 결장 또는 결장간막 등의 주변조직으로 이동하여 발생한다. 본 증례는 간내 및 간외 간질증이 영상검사에서 간 및 결장 종괴로 보여 간 전이가 있는 결장암을 모방한 증례이다. 다양한 영상검사 소견을 바탕으로 간내 및 간외 간질증의 정확한 진단이 가능하며, 특히 자기공명영상 소견이 도움을 준다.

www.e-kjar.org
https://doi.org/10.52668/kjar.2022.00157

pISSN 2586-1719 / eISSN 2799-3299
Copyright © The Korean Society of Abdominal Radiology

Korean J Abdom Radiol 2022;6:57-62

Case Report

A Curious Peripancreatic Mass: A Case of an Exophytic Pancreatic Neuroendocrine Tumor

Bohyun Kim[1], Younghoon Kim[2]
[1]Department of Radiology and [2]Department of Pathology, Seoul St. Mary's Hospital, College of Medicine, The Catholic University of Korea, Seoul, Korea

---

Pancreatic neuroendocrine tumors (PanNETs) are usually located entirely within the pancreatic parenchyma. However, unusual exophytic or pedunculated PanNETs are sometimes discovered in imaging studies, requiring differential diagnosis with various peripancreatic tumors and non-tumors. Herein, an exophytic PanNET whose origin was identified only after the surgical exploration is presented along with the potential radiologic differential diagnosis.

Keywords: Neuroendocrine tumor; Pancreas; Magnetic resonance imaging; Computed tomography; Ultrasonography

---

Introduction

Pancreatic neuroendocrine tumors (PanNETs) are uncommon tumors responsible for up to 2% of clinically detected pancreatic tumors. Although anatomic imaging modalities including the US, multidetector CT, and MRI are helpful for the initial diagnosis by revealing typical radiologic appearances of PanNET, several other lesions can mimic PanNET, especially when the tumor is exophytic or pedunculated. Herein, an exophytic PanNET that complicated the radiologic diagnosis is presented.

Case Report

A 51-year-old female patient was referred to our hospital for the evaluation of a pancreatic mass incidentally detected during a screening US. The patient was asymptomatic, and physical examination showed no abnormality. Routine laboratory tests and the level of tumor markers were all within the normal range, including the carbohydrate antigen 19-9 of 14 U/mL.

Multiphasic CT showed a 3.5-cm sized well-defined enhancing mass (arrows) on the peripancreatic area, enclosed by the pancreas, stomach, and the left lateral section of the liver (Fig. 1). On non-contrast scan (Fig. 1A), a homogeneous mass with a tiny calcification was appreciated. In axial pancreatic (Fig. 1B) and portal venous (Fig. 1C) phases, the mass enhanced well and had internal cystic components. At the posteromedial aspect of the mass, an elongated-shaped cystic lesion that abutted

Received: March 28, 2022 **Revised:** May 10, 2022 **Accepted:** May 11, 2022
Correspondence: Bohyun Kim, MD, PhD
Department of Radiology, Seoul St. Mary's Hospital, College of Medicine, The Catholic University of Korea, 222 Banpo-daero, Seocho-gu, Seoul, 06591, Korea.
Tel: +82-2-2258-5793 Fax: +82-2-599-6771 E-mail: kbh@catholic.ac.kr
This is an Open Access article distributed under the terms of the Creative Commons Attribution Non-Commercial License (http://creativecommons.org/licenses/by-nc/4.0/) which permits unrestricted non-commercial use, distribution, and reproduction in any medium, provided the original work is properly cited.

the anterior surface of the pancreas was attached to the mass (asterisks). The coronal portal venous phase (Fig. 1D) showed the cystic lesion surrounding the posterior surface of the mass. No enlarged lymph nodes were found in the abdomen and pelvis.

On axial (Fig. 2A) and coronal T2-weighted images (Fig. 2B, C), the mass (arrows) showed heterogeneously hyperintense T2 signal with tiny cystic components. An elongated-shaped cystic lesion (asterisks) attached to the pancreas and the mass was also well appreciated. Dynamic enhancement study using extracellular gadolinium-based contrast media (Fig. 2D-F) revealed heterogeneously enhancing mass abutting the liver. There was mild diffusion restriction (Fig. 2G, H).

The mass was predominantly solid and contained cystic components based on these findings. Thought to have originated from the liver or the mesentery, preliminary diagnosis of benign liver mass such as adenoma or atypical hemangioma was given along with neurogenic tumor from the mesentery. For the pathologic diagnosis, a percutaneous biopsy was planned. The US during the biopsy (Fig. 3A) revealed a well-circumscribed and heterogeneously echogenic mass abutting the liver and stomach. The anechoic cystic component was evident at

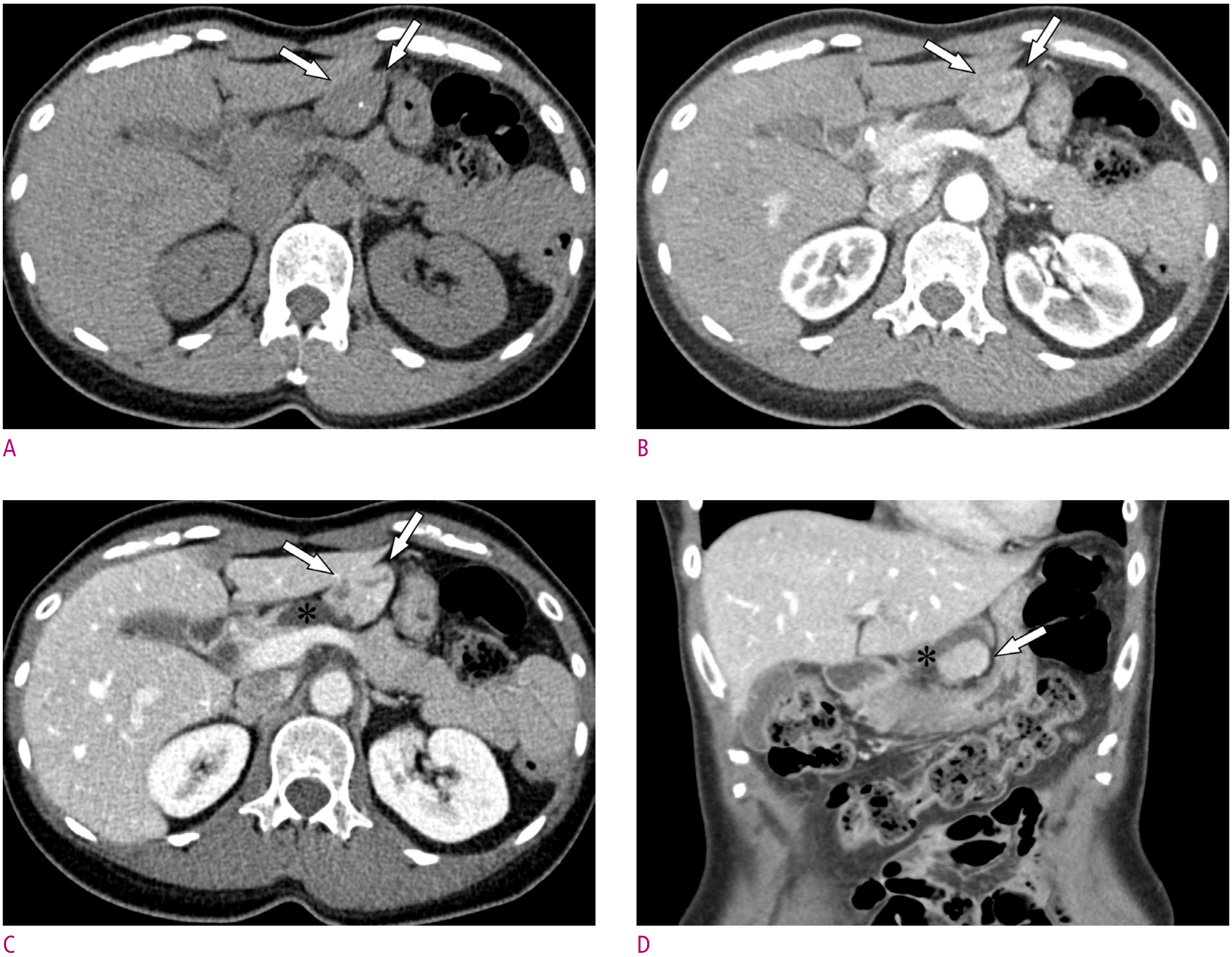

Fig. 1. Multiphasic CT reveals a 3.5 cm mass in the peripancreatic area.
On non-contrast scan (A), the mass shows homogeneous attenuation with a tiny calcification. Pancreatic parenchymal (B) and portal venous (C) phases show well-defined mass that enhances well along with cystic components. Note elongated-shaped cystic lesion between the pancreas and the tumor (arrow). Coronal multiplanar reformatted image (D) indicates that the cystic lesion surrounds the posterior surface of the tumor.

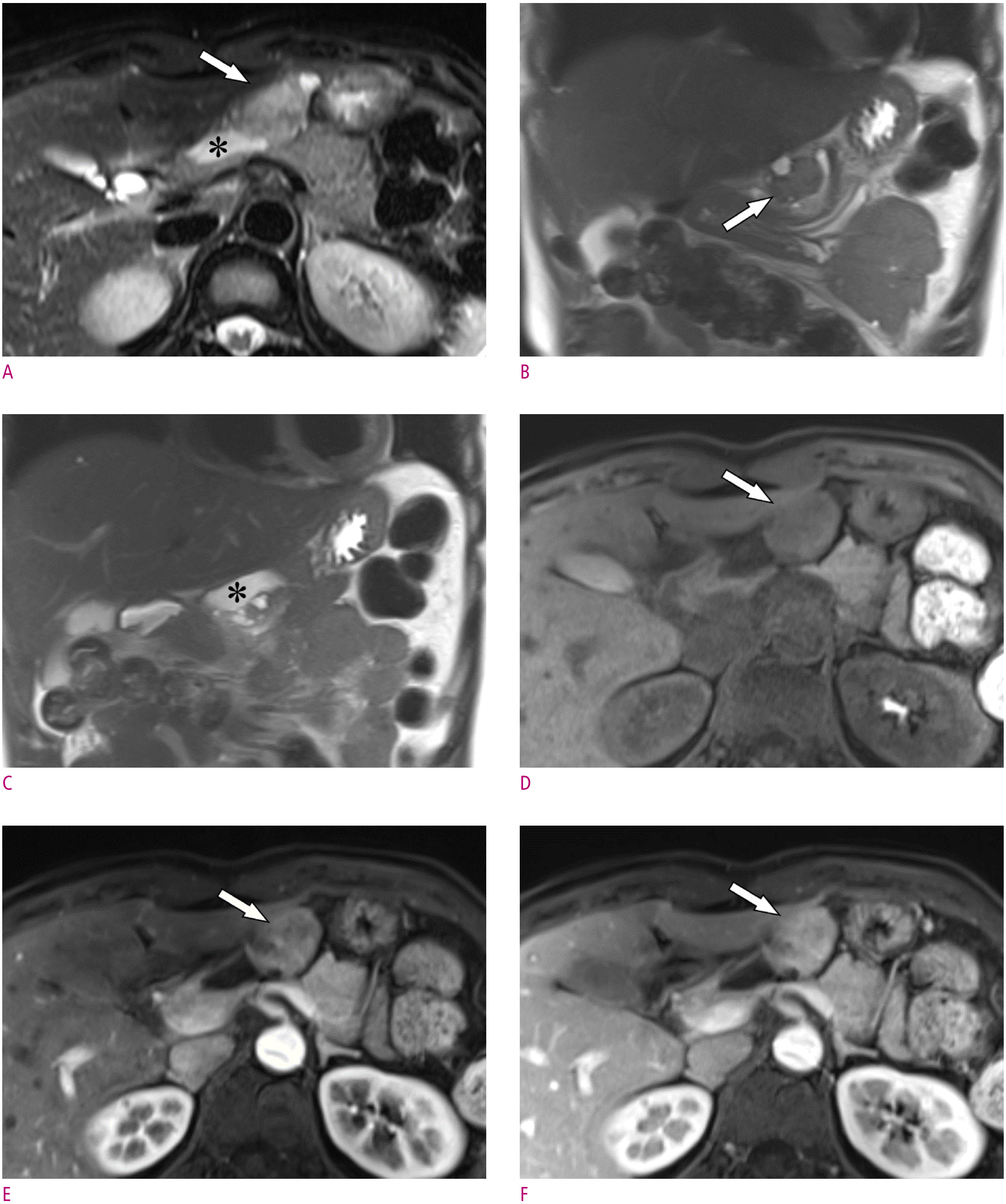

Fig. 2. MR images show a minimally lobulated mass in the peripancreatic area.
Axial TSE (TR, 3310 ms; TE, 100 ms) (A) and coronal (TR, 600 ms; TE, 93 ms) (B, C) HASTE T2-weighted images show a heterogeneously hyperintense mass with tiny cystic components. Dynamic enhancement study (D-F) shows heterogeneously enhancing mass abutting the liver.

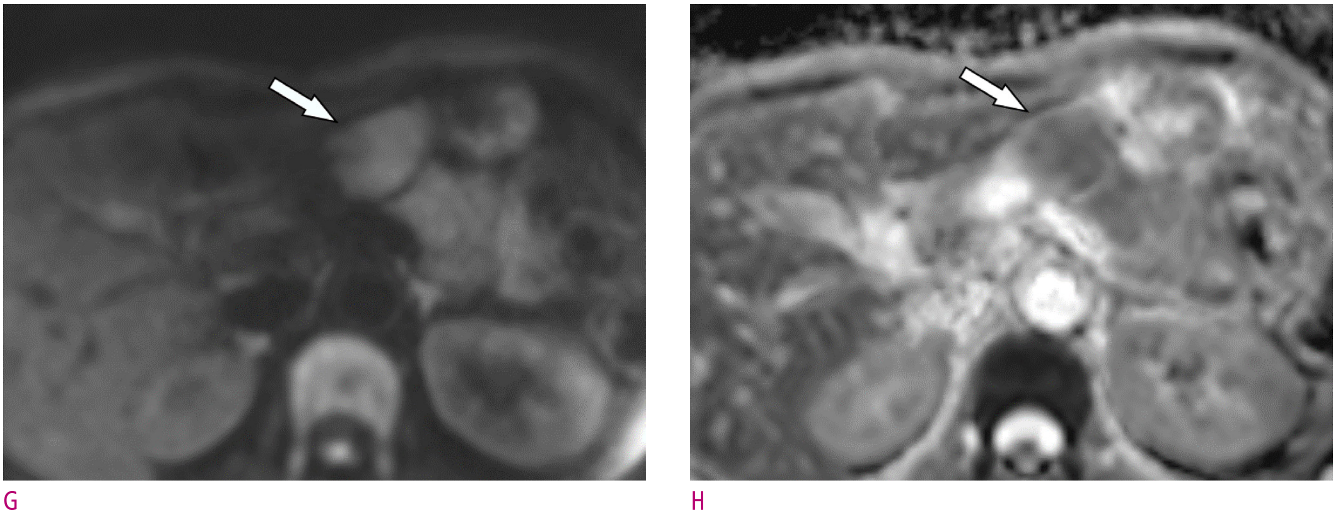

Fig. 2. Mild diffusion restriction is noted at the *b* value of 800 s/mm^2 (G) and the corresponding ADC map (H).

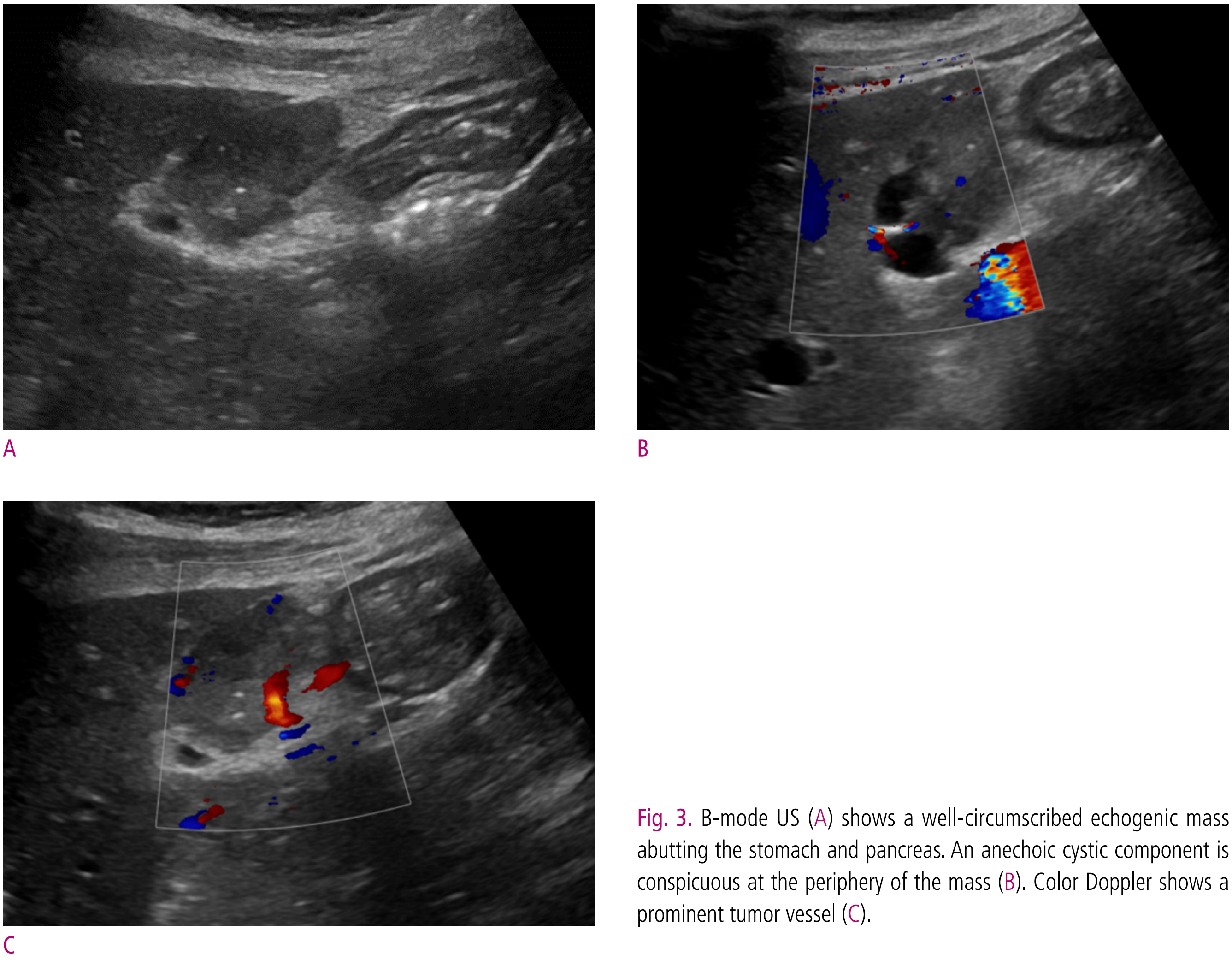

Fig. 3. B-mode US (A) shows a well-circumscribed echogenic mass abutting the stomach and pancreas. An anechoic cystic component is conspicuous at the periphery of the mass (B). Color Doppler shows a prominent tumor vessel (C).

the periphery of the mass (Fig. 3B). Color Doppler showed prominent tumor vessels (Fig. 3C). The histopathologic result of the biopsy indicated a neuroendocrine tumor, probably grade 1.

Still unsure of the origin of the tumor, diagnostic and therapeutic laparoscopy was performed. The mass was located at the lesser sac on laparoscopic exploration and was easily separated from the liver and stomach. The elongated cystic component of the mass was traced back to identify that the mass originated from the pancreas's body. Because only thin pancreatic parenchyma would remain after the tumor enucleation, distal pancreatectomy was done.

Histopathologic examination of the resected specimen revealed a 3.7 cm well-differentiated PanNET (Fig. 4) with a mitotic count of 1/10 HPF and Ki-67 proliferation rate of 1%, indicating a grade 1 tumor. Because normal pancreatic parenchyma was discovered at the periphery of the tumor, the origin was confirmed to be the pancreas. The elongated cystic lesion between the tumor and the pancreas had lined by an epithelium, suggesting a retention cyst.

Discussion

PanNETs are rare tumors responsible for up to 2% of all clinically detected pancreatic tumors. They arise from precursor cells in the pancreatic ductal epithelium with neuroendocrine differentiation (1). The 2017 WHO classification system is the most updated classification of the pancreatic neuroendocrine neoplasm, which accounts for both the degree of cellular differentiation and cellular proliferation (1, 2). PanNETs are well-differentiated tumors, while pancreatic neuroendocrine carcinomas are poorly differentiated tumors that consist of atypical cells with substantial necrosis. Within the PanNETs, mitotic counts and Ki-67 proliferation rate dictate tumor grade, ranging from 1 to 3.

On cross-sectional images, PanNETs are typically hyperenhancing during the early phase and remain hyperdense during the portal venous and delayed phases. Smaller tumors are homogeneous, but larger lesions can be heterogeneous owing to cystic degeneration, necrosis, and calcification. On MRI, PanNETs are usually hypointense on T1-weighted images and are hyperintense on T2-weighted images. Diffusion-weighted images increase the sensitivity for detecting PanNETs, as they often show restricted diffusion (3, 4).

Meanwhile, several atypical imaging features have been described. As high as 49% of PanNETs are hypovascular, mimicking pancreatic ductal adenocarcinomas (5). Other unusual features include concurrent main pancreatic duct dilatation, intraductal location of the tumor, and tumor thrombus formation in peripancreatic vessels (4). An exophytic or pedunculated PanNET is also an atypical finding, such as in the current case (6, 7). Although the exact prevalence of the exophytic PanNET has not been reported, given that enucleation is endorsed as a surgical treatment option for exophytic PanNET, it might not be highly uncommon in clinical practice (8, 9). In such cases, ambiguous tumor origin demands differential diagnoses, including peripancreatic gastrointestinal stromal tumor,

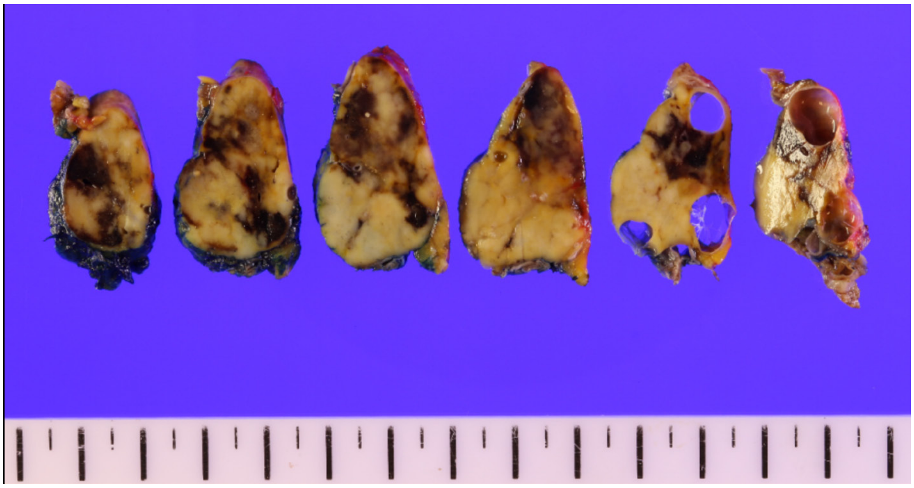

Fig. 4. Surgical and pathologic specimens revealed an exophytic solid mass with cystic components originating from the pancreas.
A well-differentiated pancreatic neuroendocrine tumor, grade 1, was confirmed.

peripancreatic paraganglioma, solitary fibrous tumor, and even lymph node (7). The most helpful clue for an accurate radiologic diagnosis is the origin of the tumor. In the current case, the gastric subepithelial tumor was ruled out by observing clearly maintained fat plane between the tumor and the stomach on the multiplanar reformatted CT images. On the other hand, the possibility of an exophytic liver mass could not be excluded because of the diminished fat plane and negative sliding sign during the real-time US. On the retrospective review, realizing that the elongated cystic lesion was attached to both the solid tumor and pancreas could have helped the diagnosis.

In conclusion, acknowledging exophytic PanNET as a differential diagnosis of various peripancreatic masses can help in making the correct diagnosis for unusual peripancreatic lesions.

References

1. WHO Classification of Tumours Editorial Board. Digestive system tumours. In: WHO classification of tumours series. 5th ed. Vol 1. Lyon, France: International Agency for Research on Cancer, 2019.
2. Choe J, Kim KW, Kim HJ, Kim DW, Kim KP, Hong SM, et al. What Is New in the 2017 World Health Organization Classification and 8th American Joint Committee on Cancer Staging System for Pancreatic Neuroendocrine Neoplasms? Korean J Radiol 2019;20:5-17.
3. Khanna L, Prasad SR, Sunnapwar A, Kondapaneni S, Dasyam A, Tammisetti VS, et al. Pancreatic Neuroendocrine Neoplasms: 2020 Update on Pathologic and Imaging Findings and Classification. Radiographics 2020;40:1240-1262.
4. Ciaravino V, De Robertis R, Tinazzi Martini P, Cardobi N, Cingarlini S, Amodio A, et al. Imaging presentation of pancreatic neuroendocrine neoplasms. Insights Imaging 2018;9:943-953.
5. Jeon SK, Lee JM, Joo I, Lee ES, Park HJ, Jang JY, et al. Nonhypervascular Pancreatic Neuroendocrine Tumors: Differential Diagnosis from Pancreatic Ductal Adenocarcinomas at MR Imaging-Retrospective Cross-sectional Study. Radiology 2017;284:77-87.
6. Lee DW, Kim MK, Kim HG. Diagnosis of Pancreatic Neuroendocrine Tumors. Clin Endosc 2017;50:537-545.
7. Raman SP, Hruban RH, Cameron JL, Wolfgang CL, Fishman EK. Pancreatic imaging mimics: part 2, pancreatic neuroendocrine tumors and their mimics. AJR Am J Roentgenol 2012;199:309-318.
8. Johnston II ME, Carter MM, Wilson GC, Ahmad SA, Patel SH. Surgical management of primary pancreatic neuroendocrine tumors. J Gastrointest Oncol 2020;11:578-589.
9. Marchese U, Gaillard M, Pellat A, Tzedakis S, Abou Ali E, Dohan A, et al. Multimodal Management of Grade 1 and 2 Pancreatic Neuroendocrine Tumors. Cancers (Basel) 2022;14:433.

외장성 성장을 한 췌장신경내분비종양의 증례

김보현[1], 김영훈[2]

[1]가톨릭대학교 서울성모병원 영상의학과, [2]가톨릭대학교 서울성모병원 병리과

초 록

췌장신경내분비종양은 대부분 완전히 췌장 실질 내에 위치한다. 그러나 드물게 췌장 실질 바깥으로 외장성 성장을 하거나 췌장 주위의 유경성 병변으로 영상검사에서 발견되는 경우가 있어 췌장 주변의 다양한 종양성 혹은 비종양성 양성 병변과 감별을 요한다. 본 췌장신경내분비종양 증례는 췌장 실질과 종양 사이가 낭성 병변으로 완전히 대치되어 있어 수술전 영상에서 종양의 기원장기를 파악하기 어려웠던 증례이다.

www.e-kjar.org
https://doi.org/10.52668/kjar.2022.00122

pISSN 2586-1719 / eISSN 2799-3299
Copyright © The Korean Society of Abdominal Radiology

Korean J Abdom Radiol 2022;6:63-67

Case Report

Massive Hemobilia Due to Arteriobiliary Fistula after the Transjugular Intrahepatic Portosystemic Shunt (TIPS): A Case Report

Hong Il Ha
Department of Radiology, Hallym University Sacred Heart Hospital, Anyang-si, Gyeonggi-do, Korea

The transjugular intrahepatic portosystemic shunt (TIPS) is an effective method for the treatment of uncontrolled refractory ascites, pleural effusion, and variceal bleeding, but the risk of complications related to the procedure is high. Arteriobiliary fistula, which is manifested as hemobilia, is one of the major fatal complications of the TIPS. Most of the TIPS-related bleeding is a complication that occurs mainly during the portal vein puncture. We are reporting a case of massive hemobilia due to hepatic arteriobiliary fistula caused by TIPS procedure.

Keywords: Hemobilia; Portasystemic Shunt; Hematemesis; Gastrointestinal hemorrhage; Fistula

Introduction

Although transjugular intrahepatic portosystemic shunt (TIPS) is an effective modality for treatment of uncontrolled refractory ascites, hydrothorax or variceal bleeding, the risk for procedure-related complications is high (1). Arteriobiliary fistula presented by hemobilia is one of major fatal complications of TIPS (2). Most TIPS associated bleeding is primarily a complication during puncture of portal vein (2). We are reporting a case of massive hemobilia due to hepatic arteriobiliary fistula caused by TIPS procedure.

Case Report

A 47-year-old man with end-stage secondary to alcoholic liver disease was admitted to our hospital for uncontrolled massive ascites, and right hydrothorax. The transjugular intrahepatic portosystemic shunt (TIPS) was planned for refractory ascites and right pleural effusion. Initial hemoglobin and platelet were 8.3 g/dL (14–17 g/dL), and 105x103/ul (130–450x103/ul), respectively. Coagulation test data were as follows: PT, 1.36 (INR, 0.88–1.13); aPTT, 39.2sec (29.1–45.1sec). Laboratory tests data were as follows: total bilirubin, 5.6 mg/dL (0.2–1.2 mg/dL); direct bilirubin, 4.1 mg/dL (0.0–0.4 mg/dL); aspartate aminotransferase, 52 U/L (8–38 U/L); alanine aminotransferase, 16 U/L (5–43 U/L);

Received: February 8, 2022 **Revised:** April 25, 2022 **Accepted:** May 9, 2022
Correspondence: Hong Il Ha, MD, PhD
Department of Radiology, Hallym University Sacred Heart Hospital, 22, Gwanpyeong-ro 170 beon-gil, Dongan-gu, Anyang-si, Gyeonggi-do 14068, Korea
Tel: +82-31-380-3880 E-mail: ha.hongil@gmail.com
This is an Open Access article distributed under the terms of the Creative Commons Attribution Non-Commercial License (http://creativecommons.org/licenses/by-nc/4.0/) which permits unrestricted non-commercial use, distribution, and reproduction in any medium, provided the original work is properly cited.

alkaline phosphatase, 102 U/L (40–130 U/L); γ-glutamyl transferase, 188 U/L (11–75 U/L); protein, 6.1 g/dL (6.4–8.1 g/dL); albumin, 2.4 g/dL (3.8–5.3 g/dL). He had a successful TIPS procedure (mean portal-systemic gradient decreased from 41 mmHg to 20 mmHg). Seven days after the TIPS, he had hematochezia, hematemesis, tachycardia, hypotension, and worsening anemia (hemoglobin dropped from 8.3 g/dL to 3.0 g/dL in 4 hours). He was in circulatory shock and was transferred to the critical care unit. He underwent CT angiography for bleeding focus evaluation. On CT angiography, the TIPS stent was patent. However, the active contrast agent leakage was noted at the distal end of stent between the right hepatic artery and the right intrahepatic bile duct. The active contrast agent leakage

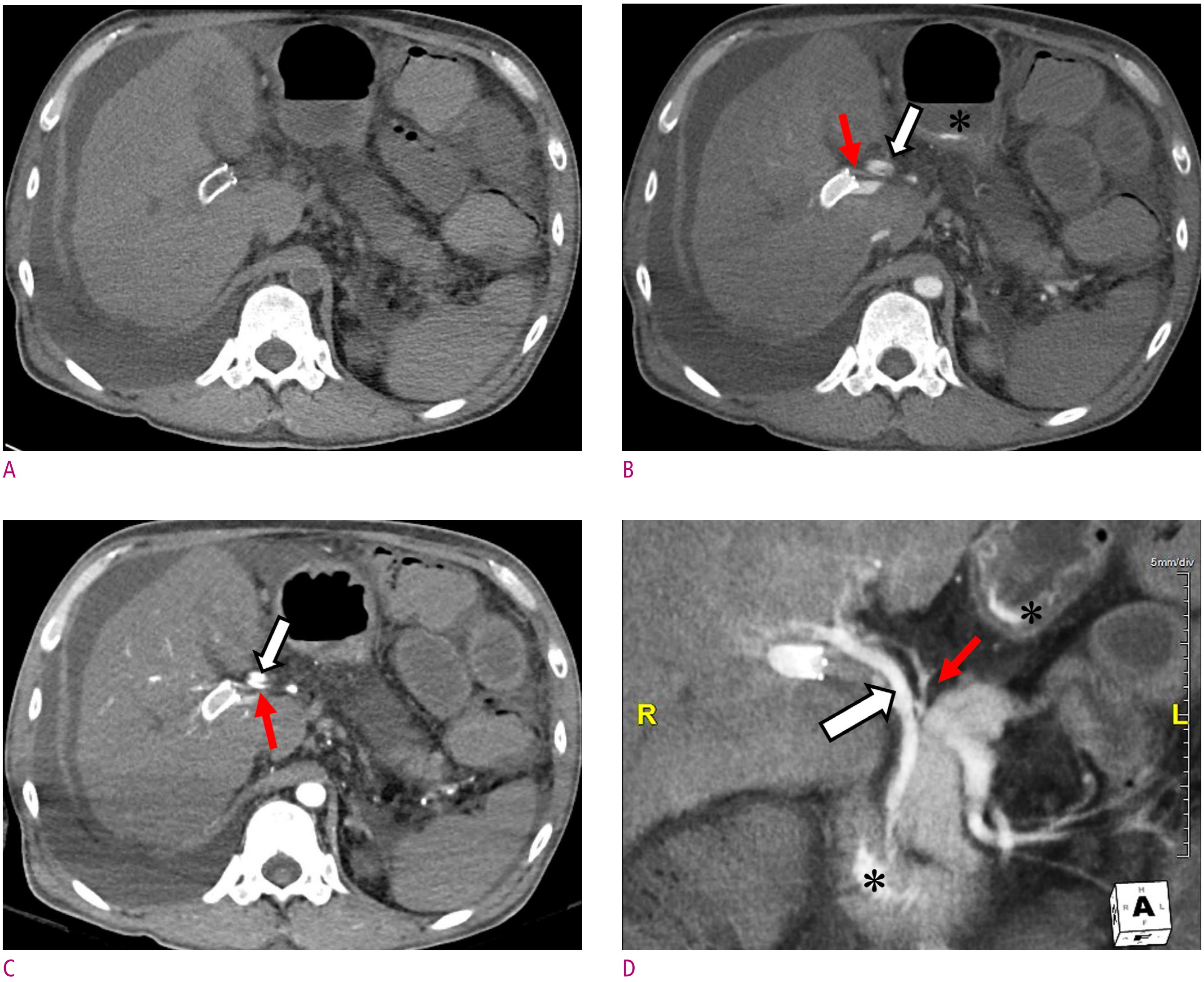

Fig. 1. CT angiography of the arteriobiliary fistula in a 47-year-old male after TIPS.
(A) Precontrast axial CT scan shows the distal end of TIPS in right portal vein. Arterial-phase axial CT scan (B) shows right hepatic artery (red arrow), portal vein and TIPS stent filled with the contrast agent, and bile duct (thick white arrow). There is small amount of the contrast agent refluxed into the gastric antrum (*) from arteriobiliary fistula. Portal-phase axial CT scan (C) shows more dense enhancement of the right hepatic artery (red arrow) and the common hepatic duct (Thick arrow). Coronal reformatted multiplanar reconstruction image parallel to the common bile duct (D) shows an arteriobiliary fistula with active contrast agent extravasation between the right hepatic artery (red arrow) and the common bile duct (thick white arrow). The leaked contrast agent was excreted into the duodenum and refluxed into the gastric antrum (*) through the common bile duct.

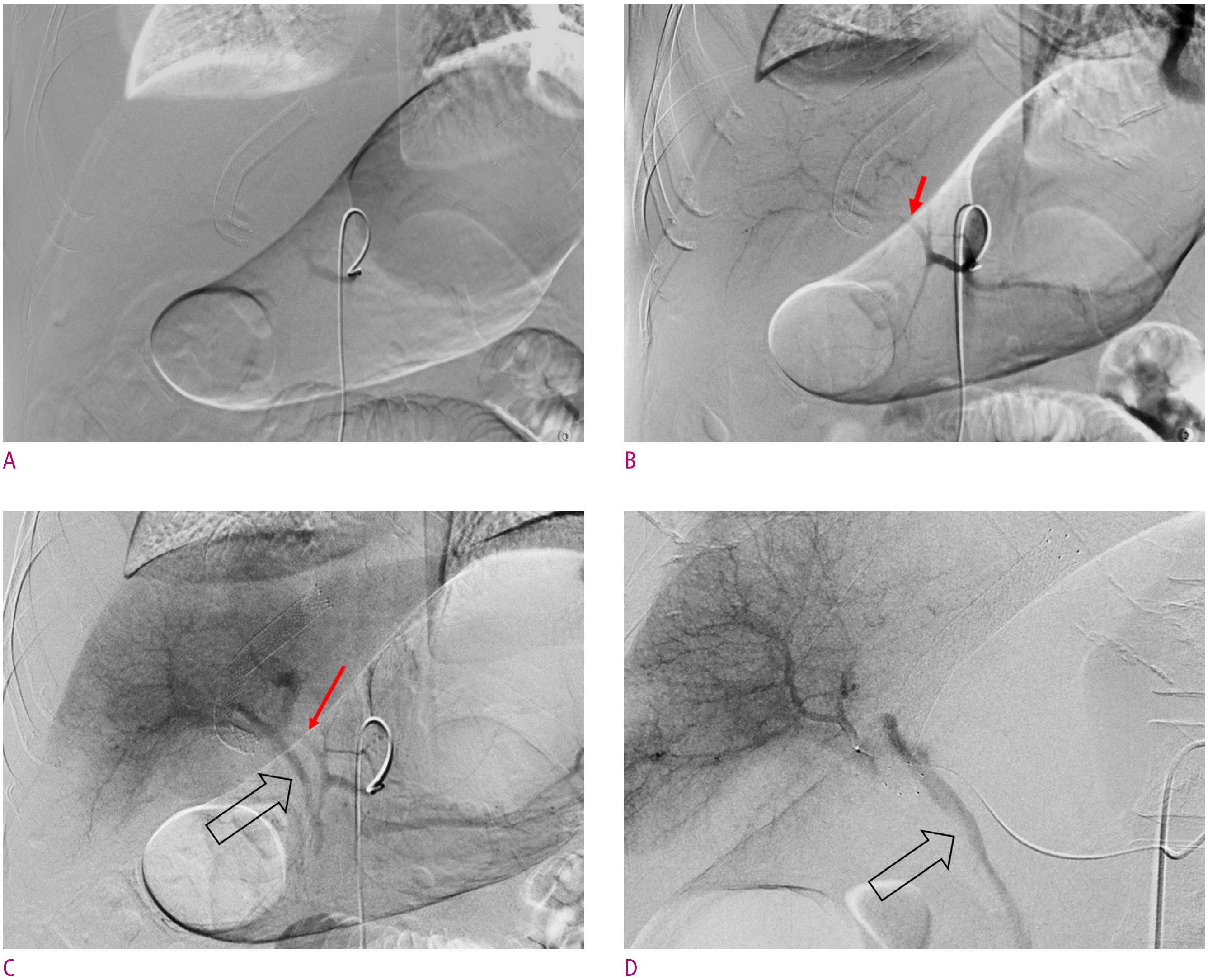

Fig. 2. Celiac angiography of the arteriobiliary fistula in a 47-year-old male after TIPS.
Early to late arterial phases (A-C) of celiac angiography show an arteriobiliary fistula with active contrast extravasation between right hepatic artery (red arrow) and right intrahepatic bile duct. Venous phase of celiac angiography shows an excreted contrast agent into the common bile duct (thick arrow).

progressed through the common bile duct and there was reflux into the gastric antrum and the duodenum (Fig. 1). The patient immediately underwent a percutaneous angiography. Celiac trunk arteriography revealed an active contrast extravasation into the common bile duct from the right hepatic artery via the arteriobiliary fistula (Fig. 2). Subsequently, selective embolization of right hepatic artery branches was successfully performed with coils, glue and gelatin sponge. However, the patient died one day after from the disseminated intravascular coagulation.

Discussion

The TIPS is the percutaneous creation of a channel between the hepatic vein and the portal vein that is used to manage complication of portal venous hypertension (3). Indications for TIPS include management of variceal bleeding, refractory cirrhotic ascites, hepatorenal syndrome, Budd-Chiari syndrome, and refractory hepatic hydrothorax (1, 3, 4). As elevated portal pressure is one of the major factors contributing to the pathogenesis of ascites and hepatic hydrothorax, TIPS is a highly effective treatment option for them (5, 6). Multiple studies have been published assessing the effectiveness of TIPS in patients with refractory ascites and technical success was achieved in 93–100% of cases, with control of ascites achieved in 27–92% and complete resolution in up to 75% of cases (1). TIPS should be considered as a treatment option for patients who require frequent paracentesis (generally >3 in a month). In addition, TIPS has been shown to resolve hepatic hydrothorax in 60–70% of patients (5, 6).

While the primary technical success rate of TIPS placement is high, complications can occur and can drastically alter patient prognosis. Potential complications of TIPS include acute liver failure, hepatic encephalopathy, hemorrhage, biliary injury, injury to surrounding organs, TIPS thrombosis, TIPS dysfunction, and TIPS migration (1).

Serious arteriobiliary fistula complication presented as a hemobilia can occasionally occur in the early postprocedural period following TIPS placement (7). Given the proximity of bile duct radicals to the branches of the hepatic artery and portal vein, the incidence of concurrent injury to these structures and consequent fistula formation is not unexpected. Approximately 3.8% incidence of hepatic vascular abnormalities was found following percutaneous transhepatic cholangiography (7, 8). The frequency of clinical hemobilia is reported up to 5% after TIPS. Often hemobilia is a self-limiting phenomenon and expectant observation is a commonly used option. Clinically significant hemobilia presents with biliary colic, jaundice, and gastrointestinal bleeding, which may range from occult to massive bleeding. The initial diagnosis can be made with endoscopy (9). CT angiography is an accurate, cost-effective tool to assess hemobilia, hematemesis, or hematochezia and can show the precise location of bleeding, thereby directing further management. Angiography with embolization is the treatment of choice for most cases of hemobilia. The goals of therapy in cases of hemobilia are to stop the bleeding and to restore bile flow. Angiography is clearly the most efficacious method for controlling intrahepatic bleeding sources, with success rates above 95% (10).

In conclusion, massive hemobilia is rare, but one of the possible complications of TIPS. A liver parenchymal puncture during a TIPS procedure may damage vascular structures such as the hepatic artery, portal vein, as well as bile duct. In cases of gastrointestinal hemorrhage after TIPS procedure, the possibility of hemobilia due to arteriobiliary fistula should be considered.

References

1. Rossle M. TIPS: 25 years later. J Hepatol 2013;59:1081-1093.
2. Puntel G, Puppini G, Perandini S, De Robertis R, Montemezzi S. Diagnosis and Management of Iatrogenic Hemobilia Secondary to Transjugular Intrahepatic Portosystemic Shunt Procedure. Cureus 2020;12:e7629.
3. Fidelman N, Kwan SW, LaBerge JM, Gordon RL, Ring EJ, Kerlan RK. The Transjugular Intrahepatic Portosystemic Shunt: An Update. AJR Am J Roentgenol 2012;199:746-755.
4. Boike JR, Thornburg BG, Asrani SK, Fallon MB, Fortune BE, Izzy MJ, et al. North American Practice-Based Recommendations for Transjugular Intrahepatic Portosystemic Shunts in Portal Hypertension. Clin Gastroenterol Hepatol. 2021.
5. Dhanasekaran R, West JK, Gonzales PC, Subramanian R, Parekh S, Spivey JR, et al. Transjugular intrahepatic portosystemic shunt for symptomatic refractory hepatic hydrothorax in patients with cirrhosis. Am J Gastroenterol 2010;105:635-641.
6. D'Amico G, Luca A, Morabito A, Miraglia R, D'Amico M. Uncovered transjugular intrahepatic portosystemic shunt for refractory ascites: a meta-analysis. Gastroenterology 2005;129:1282-1293.
7. Corral JE, Mousa OY, Riegert-Johnson DL. Massive gastrointestinal bleeding after transjugular intrahepatic portosystemic shunt (TIPS). Gut 2018;67:1123.
8. Mallery S, Freeman ML, Peine CJ, Miller RP, Stanchfield WR. Biliary-shunt fistula following transjugular intrahepatic portosystemic shunt placement. Gastroenterology 1996;111:1353-1357.
9. Moodley J, Singh B, Lalloo S, Pershad S, Robbs JV. Non-operative management of haemobilia. Br J Surg 2001;88:1073-1076.
10. Srivastava DN, Sharma S, Pal S, Thulkar S, Seith A, Bandhu S, et al. Transcatheter arterial embolization in the management of hemobilia. Abdom Imaging 2006;31:439-448.

경경정맥 간내 문맥 정맥 단락술 후 발생한 동맥-담관루에 의한 대량 혈담즙증 : 증례 보고

하 홍 일

한림대학교 성심병원 영상의학과

초 록

경경정맥간내문맥정맥단락술은 조절되지 않는 불응성 복수, 흉수, 정맥류 출혈 치료에 효과적인 방법이지만 시술과 관련된 합병증 발생 위험이 높다. 혈담즙증으로 나타나는 동맥담관 누공은 경경정맥간내문맥정맥단락술의 주요한 치명적인 합병증 중 하나이다. 대부분의 경경정맥간내문맥정맥단락술관련 출혈은 주로 문맥 천자 과정에서 발생하는 합병증이다. 저자는 경경정맥간내문맥정맥단락술 시행 후 발생한 간동맥-담도 누공에 의해 발생한 대량 혈담즙증 1예를 보고하고자 한다.

www.e-kjar.org
https://doi.org/10.52668/kjar.2022.00115

pISSN 2586-1719 / eISSN 2799-3299
Copyright © The Korean Society of Abdominal Radiology

Korean J Abdom Radiol 2022;6:68-71

Case Report

Retroperitoneal Desmoid Tumor: A Case Report

Sungeun Park
Department of Radiology, Konkuk University Medical Center, Seoul, Korea

Desmoid tumor is a rare soft tissue tumor and accounts less than 1% of retroperitoneal tumor. It is pathologically benign soft tissue tumor, while clinical behavior is aggressive, showing high rate of local recurrence. It consists of spindle cell, collagen and myxoid matrix thus it shows diverse imaging patterns according to its composition. In this case report, surgically diagnosed retroperitoneal desmoid tumor is presented.

Keywords: Retroperitoneum; Desmoid; Computed tomography

Introduction

Desmoid tumor is known as deep fibromatosis, aggressive fibromatosis, or well-differentiated fibrosarcoma. It accounts 1.5 to 3% of all soft tissue masses and less than 1% of retroperitoneal tumors (1, 2). Desmoid tumor can be sporadic or be associated with previous operation history, familial adenomatous polyposis (FAP, as Gardner syndrome), estrogen or pregnancy showing female predilection (2). Herein, we present a sporadic case of a huge desmoid tumor in a young male patient.

Case Report

A 25-year-old men was referred to our institution for evaluation of ultrasound detected left upper quadrant mass (Fig. 1A) due to left flank pain. He suffered from left flank pain for one month. He had undergone appendectomy for acute appendicitis eight years ago. Except this medical history, he had no other underlying disease including familial adenomatous polyposis (FAP).

On pre-operative contrast-enhanced CT, a huge (more than 22 cm) solid mass was found at the left upper quadrant (Fig. 1B-E). The solid lesion showed heterogeneous enhancement on CT. It displaced spleen medially and left kidney caudally and closely abutted to splenic flexure colon. ^{18}F-Fluorodeoxyglucose (FDG) PET-CT was performed and the mass showed FDG uptake on FDG PET-CT (Fig. 1F).

He underwent tumor excision, under suspicious of malignant mass such as lymphoma or myxoid liposarcoma. On surgical specimen, the huge yellowish mass showed adhesion to spleen, splenic flexure colon and abdominal wall. Therefore, retroperitoneal mass excision was performed with splenectomy and segmental colectomy. On histopathology, the solid lesion was filled with spindle cells on H&E staining, and was pathologically confirmed

Received: February 4, 2022 **Revised:** April 20, 2022 **Accepted:** May 19, 2022
Correspondence: Sungeun Park, MD
Department of Radiology, Konkuk University Medical Center, 120-1, Neungdong-ro, Gwangjin-gu, Seoul 05030, Korea
Tel: +82-2-2030-5527 Fax: +82-2-2030-5549 E-mail: clickse0812@gmail.com
This is an Open Access article distributed under the terms of the Creative Commons Attribution Non-Commercial License (http://creativecommons.org/licenses/by-nc/4.0/) which permits unrestricted non-commercial use, distribution, and reproduction in any medium, provided the original work is properly cited.

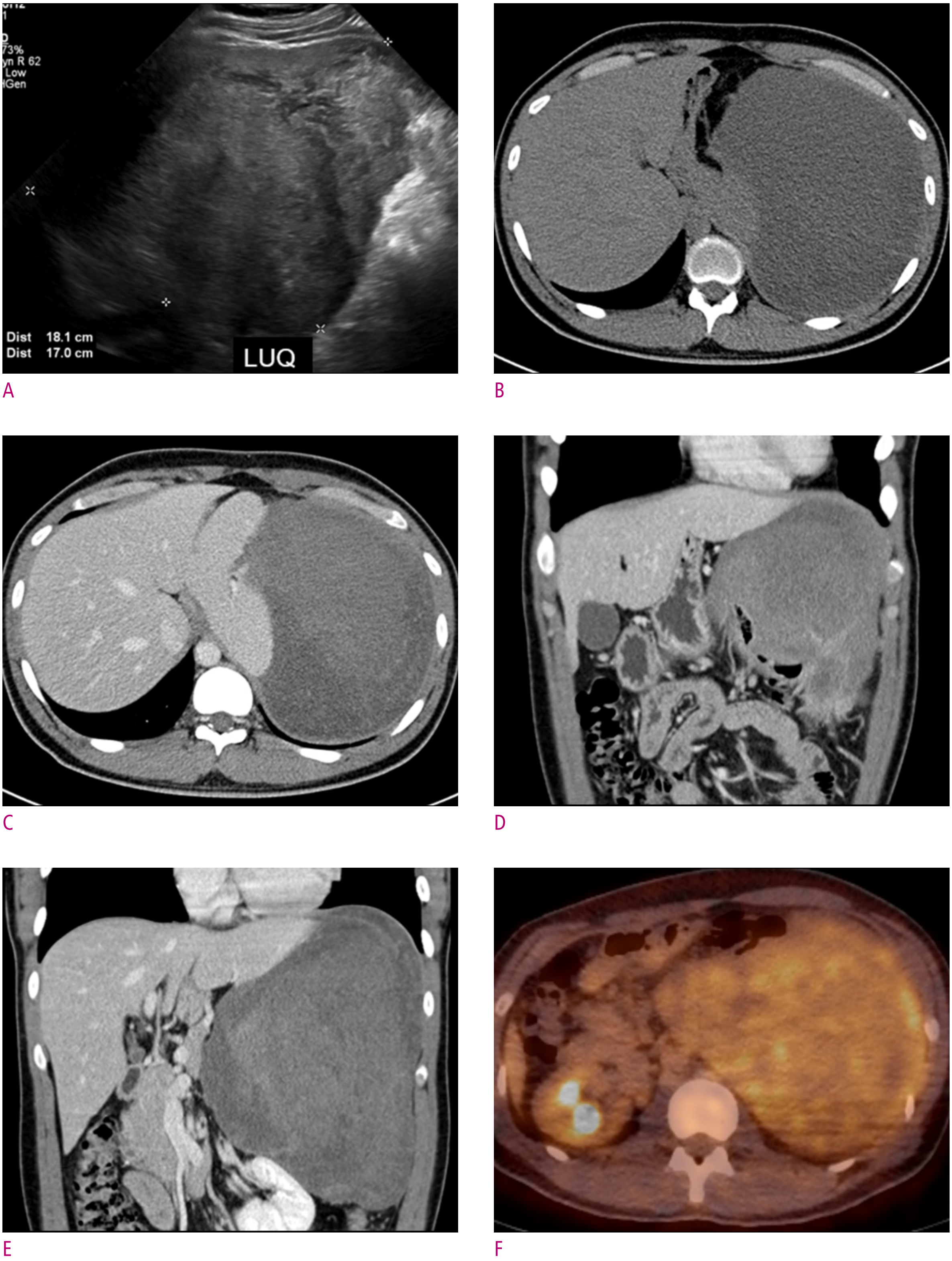

Fig. 1. Imaging findings of a desmoid tumor in a 25-year-old man.

A more than 18 cm sized low echoic lesion was seen on ultrasound at the left upper quadrant area, during evaluation for left flank pain (A). On contrast enhanced CT, a more than 22 cm sized, huge solid lesion is seen at the left upper retroperitoneum (B-E). It shows heterogeneous enhancement, displaces the spleen and left kidney, and encases splenic flexure colon. On ^{18}F-Fluorodeoxyglucose (FDG) PET-CT, FDG uptake was shown (F).

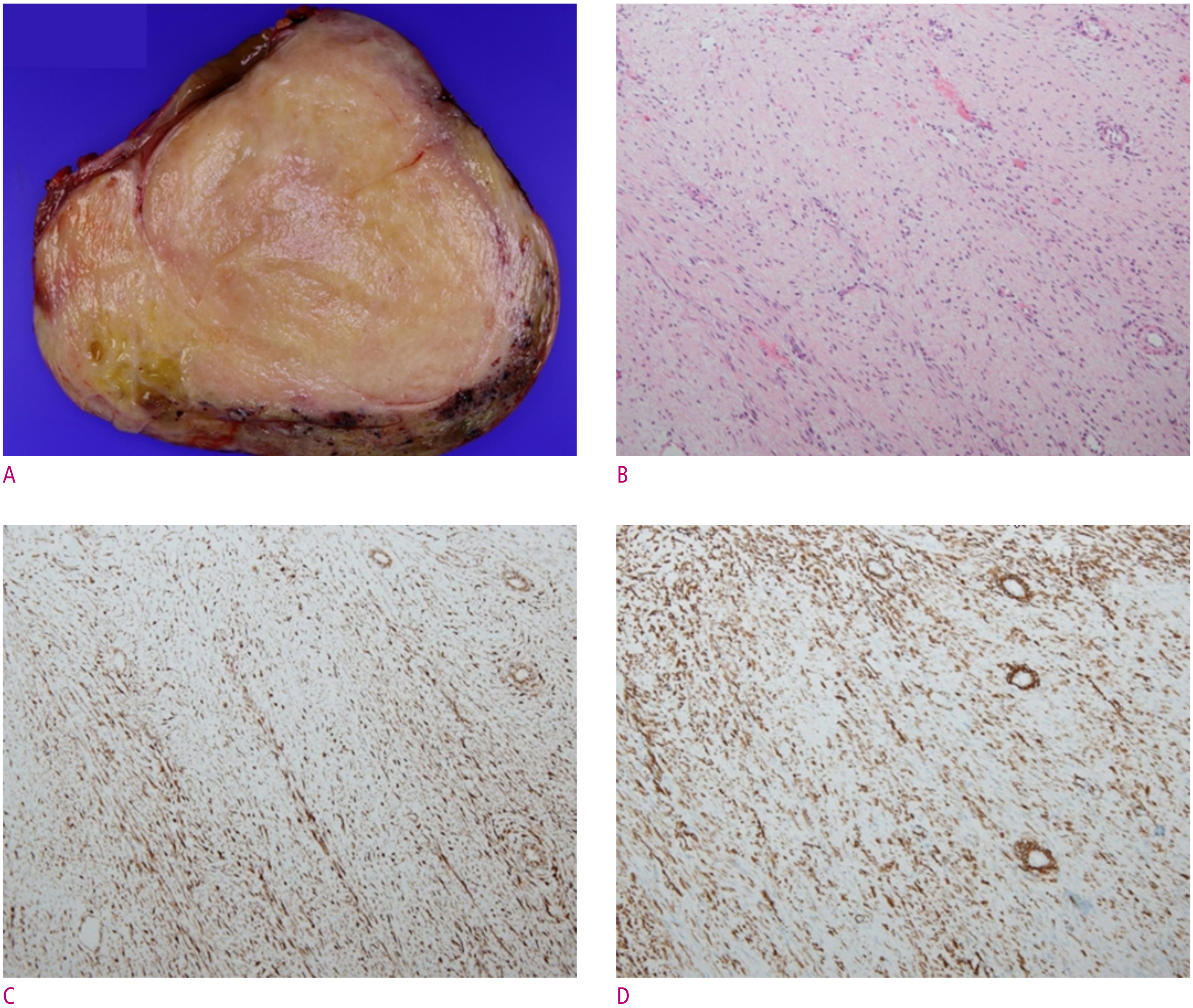

Fig. 2. Pathologic findings of a desmoid tumor in a 25-year-old man.
The huge solid tumor was hard and infiltrative to adjacent organ, thus splenectomy and segmental colectomy were performed with retroperitoneal tumor excision (A). The tumor composed of spindle cells on H&E staining (x 100) (B). On immunohistochemistry, β-Catenin (C) and smooth muscle actin (SMA) (D) staining showed positive, thus desmoid tumor was diagnosed.

as a desmid tumor, showing β-Catenin and smooth muscle actin (SMA) staining (Fig. 2).

Discussion

Desmoid tumor arises from musculoaponeurotic structures and disrupts adjacent muscular and soft-tissue planes. Desmoid tumor can appear as an ill-defined infiltrative soft-tissue mass in mesenteric or deep tumors, while it can be sharply marginated tumors, in abdominal-wall (3).

For diagnosis and follow-up, CT is the most commonly used imaging modality. It shows variable attenuation or enhancement patterns according to its compositions (spindle cell, collagen and myxoid matrix) (2). With abundant myxoid elements, it can be hypoattenuated, while necrosis and calcifications are rare (4). MRI can reflects those component, with excellent soft-tissue contrast. T2 high signal intensity can be shown with myxoid matrix, while low T2 signal intensity with abundant collagen component (3). Desmoid tumor needs to be differentiated from other neoplasms, such as lymphoma, pleomorphic sarcoma, and fibrosarcoma with imaging findings, thus pathologic confirmation is needed before definitive treatment (3).

If possible, surgical resection with a wide margin is the treatment of choice for symptomatic desmoid tumors. When operation is not feasible due to tumor's location, local invasion state or patient's conditions, the other treatment option includes radiotherapy, conventional chemotherapy, hormonal agents, and newer molecular targeted agents (3, 5).

In conclusion, we report a case of the desmoid tumor, sporadically arisen in retroperitoneum, with imaging features on CT. In our case, a huge left retroperitoneal mass showed heterogeneous enhancement, with infiltrative margin encasing splenic flexure colon and showed mass effect displacing spleen and left kidney. Although it is a pathologically benign tumor, it should be differentiated from malignant retroperitoneal tumors such as lymphoma or liposarcoma, due to its local aggressive features.

References

1. Casillas J, Sais G, Greve JL, et al. Imaging of intra- and extraabdominal desmoid tumors. Radiographics 1991;11:959-968.
2. Rajiah P, Sinha R, Cuevas C, et al. Imaging of uncommon retroperitoneal masses. Radiographics 2011;31:949-976.
3. Shinagare AB, Ramaiya NH, Jagannathan JP, et al. A to Z of desmoid tumors. American Journal of Roentgenology 2011;197:W1008-W1014.
4. Kim J-h, Moon KC, Park S-W, et al. Desmoid-type fibromatosis in the head and neck: CT and MR imaging characteristics. Neuroradiology 2013;55:351-359.
5. Alman B, Attia S, Baumgarten C, et al. The management of desmoid tumours: a joint global consensus-based guideline approach for adult and paediatric patients. European Journal of Cancer 2020;127:96-107.

후복강 유건종: 증례 보고

박성은

건국대학교병원 영상의학과

초 록

유건종은 드물게 발생하는 연조직 종양으로 후복강 종양의 1% 미만을 차지한다. 유건종은 병리학적으로 양성 연조직 종양이나, 높은 재발율을 보여 임상적 양상은 공격적이다. 이것은 방추 세포, 콜라겐과 점액성 기질로 구성되어있는데, 구성 성분에 따라서 영상 소견이 다양하게 보인다. 본 증례보고에서, 수술로 진단된 후복강의 유건종을 발표한다.

www.e-kjar.org
https://doi.org/10.52668/kjar.2022.00108

pISSN 2586-1719 / eISSN 2799-3299
Copyright © The Korean Society of Abdominal Radiology

Korean J Abdom Radiol 2022;6:72-76

Case Report

장중첩증을 유발한 회장의 염증성 섬유양 용종

이은선
중앙대학교병원 영상의학과

Inflammatory Fibroid Polyp of Ileum with Intussusception

Eun Sun Lee
Department of Radiology, Chung-Ang University Hospital, Chung-Ang University College of Medicine, Seoul, Korea

---

Inflammatory fibroid polyps are rare benign tumors of the gastrointestinal tract with the gastric antrum being the most common site, followed by the ileum. This case report presents a large inflammatory polyp causing ileal intussusception in a 78-year-old male patient, complaining abdominal pain, with a literature review.

Keywords: Intestine; Small; Intestinal polyps; Ultrasonography; Intussusception; Multidetector computed tomography

---

서 론

염증성 섬유양 용종 (inflammatory fibroid polyp)은 비교적 드문 위장관의 양성 점막하 병변으로, 염증세포의 침윤과 섬유결합조직 및 혈관의 증식을 특징으로 하는데 특히 호산구 침윤이 뚜렷하다 (1, 2) 거의 대부분 위에서 단발성으로 발생하는데, 위를 제외한 위장관에서는 회장에서 많이 발생하는 것으로 알려져 있다. 본 저자는 회장에 생긴 8 cm의 염증성 섬유양 용종이 장중첩증을 일으켜 수술적 절제를 한 증례를 경험하여 문헌고찰과 함께 영상 소견에 대하여 보고하고자 한다.

증례 보고

78세 남자가 2주 전부터 시작된 복부 전반에 걸친 통증으로 내원하였다. 환자는 이전 복강경하 담낭절제술을 받은 수술력 외에 특이 과거력은 없었다. 내원시 시행한 피검사에서 혈액 내 C-reative protein 수치가 81.5 mg/L, 백혈구가 12,360 /μL으로 상승되어 있었다. 복부X선촬영검사에서는 상복부에 뭉쳐진 소장 공기음영이 확인되어 경도의 소장 폐색이 의심되었다 (Fig. 1). 초음파 검사에서는 배꼽 아래 8 × 3 cm의 비교적 균질하고 경계가 매끈한 고형 종괴가 있었으며, 종괴의 내부에는 혈류가 확인되었다. 또한 회장-회장 장중첩증이 동반되어 있음을 확인할 수 있었다 (Fig. 2A-C). 추가로 시행한 전산화단층촬영에서 해당 종괴는 조영 전 17.8 HU에서 조영 후 문맥기 영상에서 41.0 HU으로 상승하는 경도의 조영증강이 있었고, 경계는 매끈하며 내부는 균일하였다. 경도의 소장벽 비후와 장간막 부종, 주위 혈관 확장이 있었으나 소장 괴사의 징후는 보이지 않았다 (Fig. 3A-C).

환자는 증상의 호전이 없어 부분 소장절제를 시행 받았다. 확보된 검체에서 회장에 8 × 3 × 3 cm의 내강으로 돌

Received: January 13, 2022 **Revised:** May 24, 2022 **Accepted:** May 24, 2022
Correspondence: Eun Sun Lee, MD, PhD
Department of Radiology, Chung-Ang University Hospital, Chung-Ang University College of Medicine, 102, Heukseok-ro, Dongjak-gu, Seoul 06973, Korea
Tel: +82-2-6299-3209 Fax: +82-2-6299-2017 E-mail: seraph377@gmail.com
This is an Open Access article distributed under the terms of the Creative Commons Attribution Non-Commercial License (http://creativecommons.org/licenses/by-nc/4.0/) which permits unrestricted non-commercial use, distribution, and reproduction in any medium, provided the original work is properly cited.

Fig. 1. 복부X선촬영검사에서 상복부에 뭉쳐진 소장 공기음영이 확인되어 경도의 소장 폐색을 의심할 수 있다.

출하는 커다란 종괴를 확인하였다 (Fig. 4). 현미경 검사 상 종괴 내부에는 많은 호산구와 섬유모세포가 있었으며, 면역화학 검사에서 Vimentin에 양성, CD-117 음성, CD-34 음성 소견을 보였다 (Fig. 4B, C). 최종적으로 종괴는 염증성 섬유양 용종으로 진단되었다.

고 찰

염증성 섬유양 용종은 비교적 드문 위장관의 양성 점막하 병변으로, 현재로서는 정확한 원인은 불명확하나, 소장의 부분적 외상이나 호산구성 장염, 만성 염증성 장질환과 관련된 염증성 반응 때문일 것이라 믿어지고 있다 (3). 크기는 0.2 cm에서 12 cm까지 다양하게 보고되고 있고 (2), 크기가 작을 경우 대부분 무증상이나 크기가 크면 복통, 장폐색, 장중첩증, 출혈 등의 합병증을 동반하면서 수술적 절제를 시행을 통해 진단되는 경우가 많았다. 어른에서 발생하는 장중첩증은 소아에 비해 드문데다가, 그 선행요인이 염증성 섬유양 용종인 경우는 더욱 드물어 현재까지 100

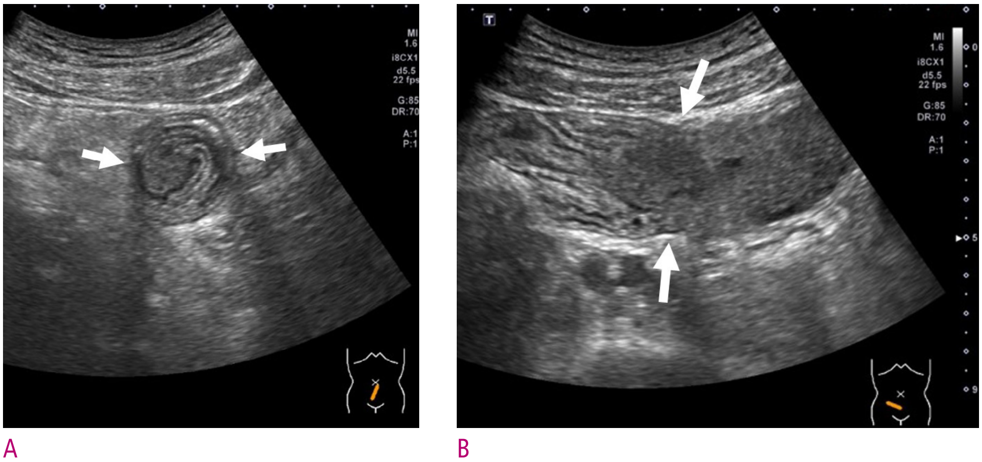

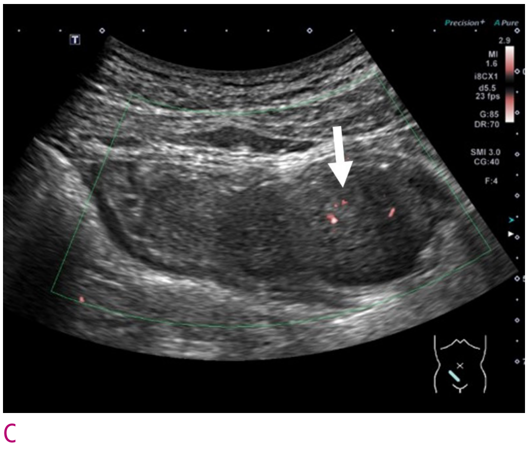

Fig. 2. 초음파검사에서 배꼽아래에서부터 우하복부에 걸쳐 8 cm 크기의 저에코를 보이는 내강으로 돌출된 회장 종양과 이로 인해 생긴 장중첩증이 횡단면 (A)과 종단면 (B)에서 확인된다 (화살표). 종양의 내부는 비교적 균질하여 경계는 좋다. 미세혈류영상에서 종양내부의 느리고 약한 혈류 (화살표)가 확인된다 (C).

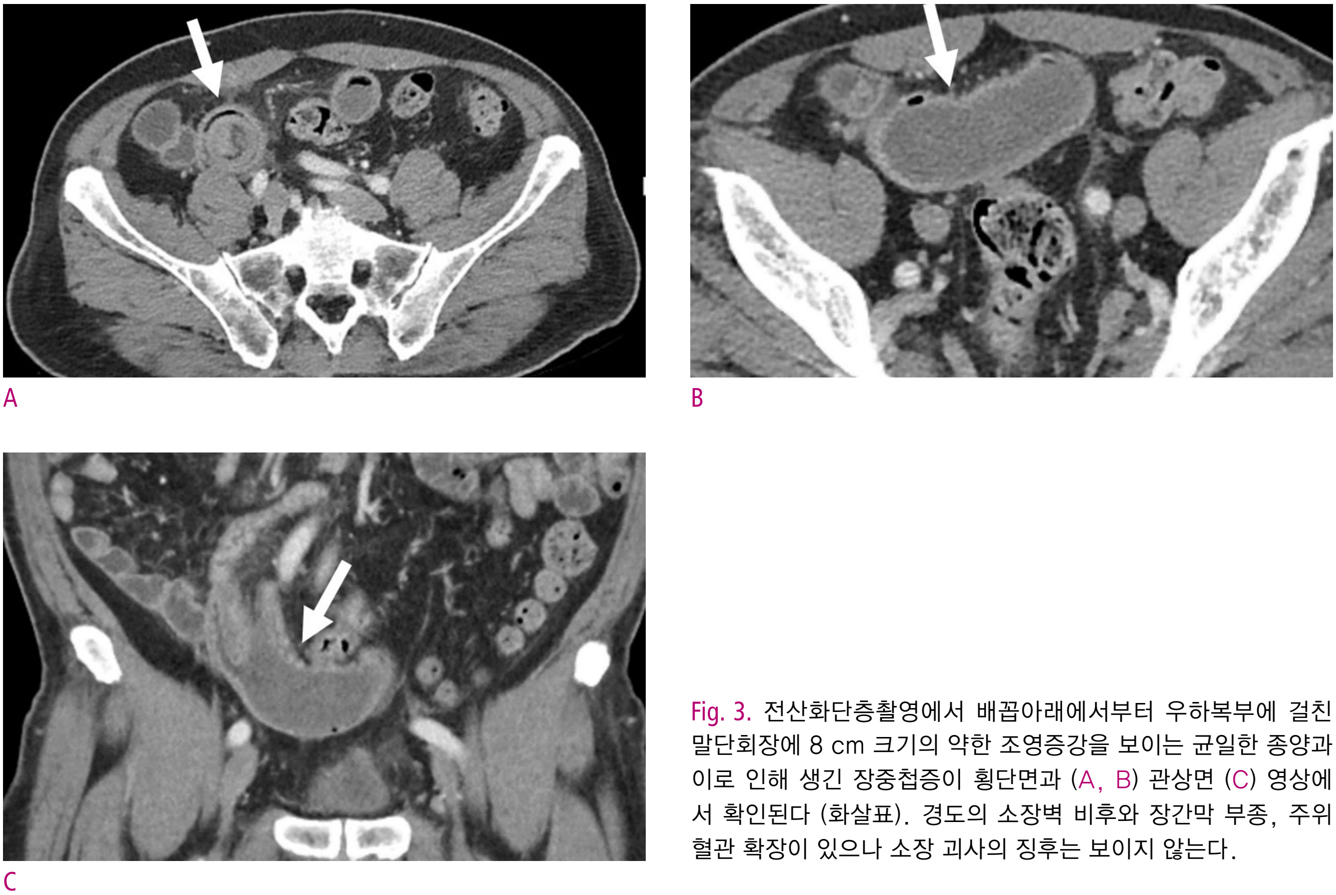

Fig. 3. 전산화단층촬영에서 배꼽아래에서부터 우하복부에 걸친 말단회장에 8 cm 크기의 약한 조영증강을 보이는 균일한 종양과 이로 인해 생긴 장중첩증이 횡단면과 (A, B) 관상면 (C) 영상에서 확인된다 (화살표). 경도의 소장벽 비후와 장간막 부종, 주위 혈관 확장이 있으나 소장 괴사의 징후는 보이지 않는다.

개 미만의 증례만이 보고되었다 (4). 보통 어른에서 장중첩증이 의심되는 경우에는 초음파보다는 전산화단층촬영이 우선되는데, 그 이유는 소아와 달리 어른에서 장중첩증이 발생한 경우에서는 대부분 종양이 그 선행요인으로 작용하기 때문이며 악성질환의 가능성이 높기 때문이다. 본 증례에서는 혈액검사에서 염증이 의심되는 복통 환자로 급성 충수돌기염을 배제하기 위해 시행한 초음파 검사에서 소장의 장중첩증과 종양을 발견하여 추가로 전산화단층촬영을 진행하였다. 현재까지 염증성 섬유양 용종의 영상소견에 대한 연구는 충분하지 않지만 보고된 증례들에 따르면, 초음파에서는 점막하층에서 기원하는 경계가 좋은 저에코의 종괴로 (5) 보인다. 전산화단층촬영에서는 조영증강의 정도는 다양하였으며, 경계가 좋은 내강 돌출형 종괴로 비교적 내부 성상이 균일한 경우가 많았다 (1, 3-6). 본 증례 또한 초음파에서 경계가 좋은 저에코의 종괴로 내부의 혈류를 확인할 수 있었으나, 그 속도와 밀도는 다소 낮았다. 전산화단층촬영상에서는 조영증강이 되기는 하나 그 차이가 문맥기 기준으로 20 HU 정도로 미약하였는데, 아마도 장중첩증이 발생하면서 공급되는 혈류의 양이 감소하여 생긴 이차변화일 가능성이 있다. 문헌상 보이는 다양한 조영증강의 정도는 동반된 장폐색이나 장중첩증 유무에 따른 혈류변화에 따른 결과로 유추된다.

기본적으로 점막하 종양인만큼 감별진단으로 위장관기질종양 (gastrointestinal stromal tumor)를 꼽을 수 있다. 다만 위장관기질종양은 크기가 클 경우 내부 궤양, 출혈 등 비균질성을 보일 요소가 많으며, 내강으로 돌출하기 보다는 양쪽으로 자라거나 바깥쪽으로 더 많이 자라는 경우가 많은데 이는 점막하층 중에서도 근육층에서 기원하는 경우가 많기 때문이다. 위에 생긴 병변일 경우에는 이소성췌장과 감별이 필요한데 대부분의 이소성췌장은 초음파에서 고에코를 보이고 내부가 비균질적이며 경계가 미세엽상을 보이게 된다. 위가 아닌 장관에서도 이소성췌장이 가능하나 성상이 기본적으로 부드러워 폐색 등의 종괴 효과를 일으키는 경우는 거의 없다.

결론적으로, 어른에서 회장에 비교적 균질하고 경계가 매끈하며 내강으로 돌출하는 양상의 점막하 종양이 발견된다면 염증성 섬유양 용종의 가능성을 생각해 볼 필요가 있다.

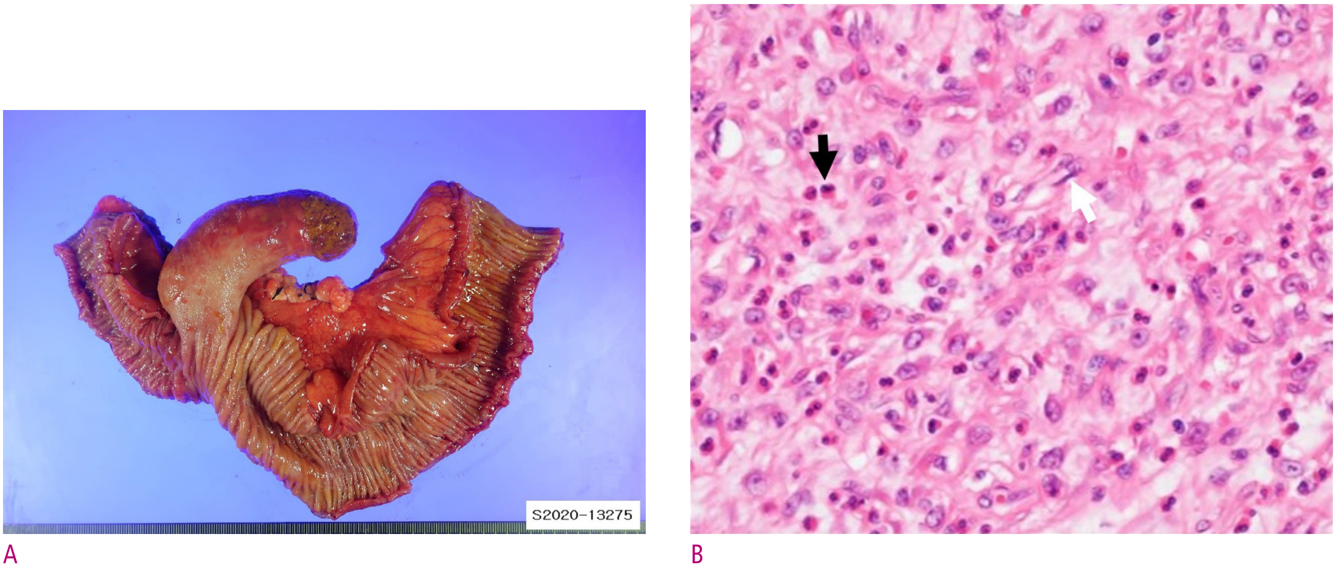

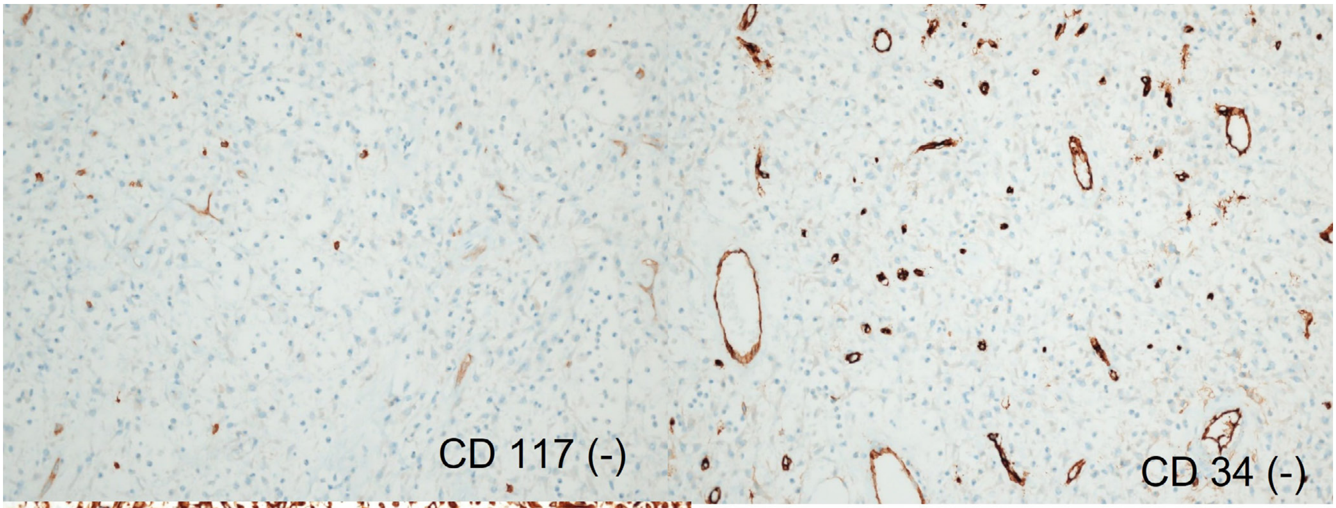

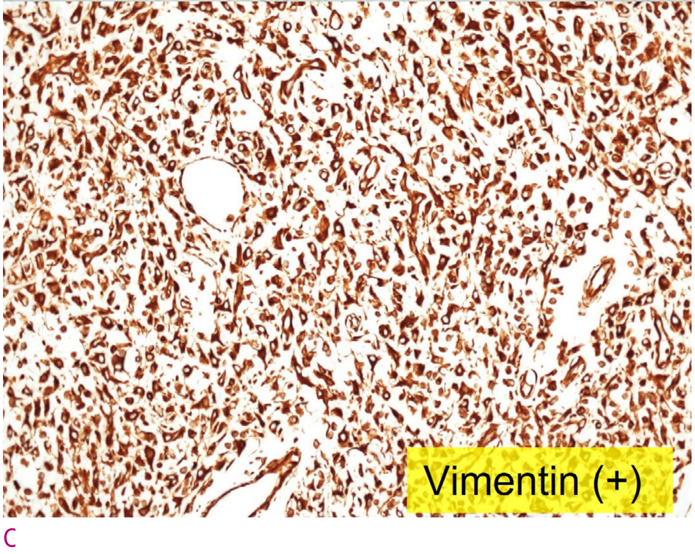

Fig. 4. 수술 후 확보된 검체에서 회장에 8 x 3 x 3 cm의 내강으로 돌출하는 커다란 종괴를 확인할 수 있으며 그 말단은 중앙부는 괴사가 진행되어 있다 (A). 현미경 검사에서 종괴 내부에는 많은 호산구 (검은 화살표)와 섬유모세포 (흰 화살표)가 관찰되며 (B), 면역화학 검사에서 Vimentin에 양성, CD-117 음성, CD-34 음성 소견을 보였다 (C).

References

1. Gara N, Falzarano JS, Limm WM, Namiki TS, Tom LK. Ileal inflammatory fibroid polyp causing chronic ileocolic intussusception and mimicking cecal carcinoma. World J Gastrointest Oncol 2009;1:89-92.
2. Kim YI, Kim WH. Inflammatory fibroid polyps of gastrointestinal tract. Evolution of histologic patterns. Am J Clin Pathol 1988;89:721-727.
3. Yoon DW, Lee BJ, Lee JH, Park JJ, Kim JS, Bak YT, et al. A case of giant inflammatory ileal polyp removed by double-balloon enteroscopy. Clin Endosc 2012;45:198-201.
4. Akbulut S. Intussusception due to inflammatory fibroid polyp: a case report and comprehensive literature review. World J Gastroenterol 2012;18:5745-5752.
5. Bhutia CT, Das D, Bhutia P. Inflammatory fibroid polyp of the ileum presenting with acute intestinal obstruction in an adult patient: a case report. J Clin Diagn Res 2016;10:EJ01-2.
6. Bae JS, Song JS, Hong SM, Moon WS. An unusual presentation of an inflammatory fibroid polyp of the ileum: A case report Oncol Lett 2015;9:327-329.

장중첩증을 유발한 회장의 염증성 섬유양 용종

이은선
중앙대학교병원 영상의학과

초 록

염증성 섬유양 용종 (inflammatory fibroid polyp)은 비교적 드문 위장관의 점막하 병변으로 위를 제외한 위장관에서는 회장에서 많이 발생하는 것으로 알려져 있으나 빈도는 극히 드물며 그 영상소견 또한 알려진 바가 거의 없다. 본 저자는 복통으로 내원한 78세 남자가 초음파와 전산화단층촬영을 통해 장중첩증을 일으키는 8 cm의 균질한 점막하종양이 회장에서 발견되어 수술을 거쳐 염증성 섬유양 용종으로 진단되었기에 이 영상 소견을 문헌고찰과 함께 보고하고자 한다.

www.e-kjar.org
https://doi.org/10.52668/kjar.2022.00171

pISSN 2586-1719 / eISSN 2799-3299
Copyright © The Korean Society of Abdominal Radiology

Korean J Abdom Radiol 2022;6:77-81

Case Report

Segmental Arterial Mediolysis of the Abdominal Vessel: A Case Report

Hyo-Jin Kang[1,2]
[1]*Department of Radiology, Seoul National University Hospital, Seoul, Korea*
[2]*Department of Radiology, Seoul National University College of Medicine, Seoul, Korea*

Segmental arterial mediolysis (SAM) is a rare but serious arteriopathy of unknown etiology with life-threatening manifestation. It is characterized by lysis of the medial layer of the arterial wall and may result in dissection, stenosis, occlusion, and aneurysm formation. We would like to report a case of SAM that occurred in the hepatic and visceral arteries and caused the ischemia.

Keywords: Segmental arterial mediolysis; Artery; Bleeding; Occlusion; Angiography

Introduction

Segmental arterial mediolysis (SAM) is a rare but serious non-atherosclerotic, non-inflammatory arteriopathy of unknown etiology with life-threatening manifestation (1). It mainly affects the medium-sized vessels of the abdomen and is characterized by lysis of the medial layer of the arterial wall. It may result in dissection, stenosis, occlusion, and aneurysm formation (2, 3). Given its rarity and angiographic similarities to other vasculopathy, the diagnosis of SAM can be challenging and is often missed. We here describe the case of SMA focused on CT angiography features.

Case Report

A 34-year-old female patient was referred to our hospital for recurrent abdominal pain. The pain is usually aggravated in the post-prandial period. Routine laboratory tests were within normal range, including high sensitivity C-reactive protein (hs-CRP) of 0.46 mg/dL.

The CT angiography revealed the concentric luminal narrowing of the celiac trunk and proximal superior mesenteric artery (SMA). There was no significant stenosis in both renal arteries (Fig. 1). Digital subtraction angiography for mesenteric arteries presented multifocal strictures of distal SMA, left colic artery, and sigmoid artery.

One-day after, the abdominal pain was aggravated. The second CT angiography revealed the segmental occlusion of the right hepatic artery with the ischemic change of the subcapsular area of the right posterior section of the liver. In addition, diffuse pneumatosis intestinalis was noted with markedly decreased bowel enhancement (Fig. 3).

Immunological laboratory tests were performed to exclude autoimmune or inflammatory causes of

Received: April 4, 2022 **Accepted:** May 4, 2022
Correspondence: Hyo-Jin Kang, MD, PhD
Department of Radiology, Seoul National University College of Medicine, 101 Daehangno, Jongno-gu, Seoul, 03080, Korea
Tel: +82-2-2072-3107 Fax: +82-2-743-6385 E-mail: loveyoon@snu.ac.kr
This is an Open Access article distributed under the terms of the Creative Commons Attribution Non-Commercial License (http://creativecommons.org/licenses/by-nc/4.0/) which permits unrestricted non-commercial use, distribution, and reproduction in any medium, provided the original work is properly cited.

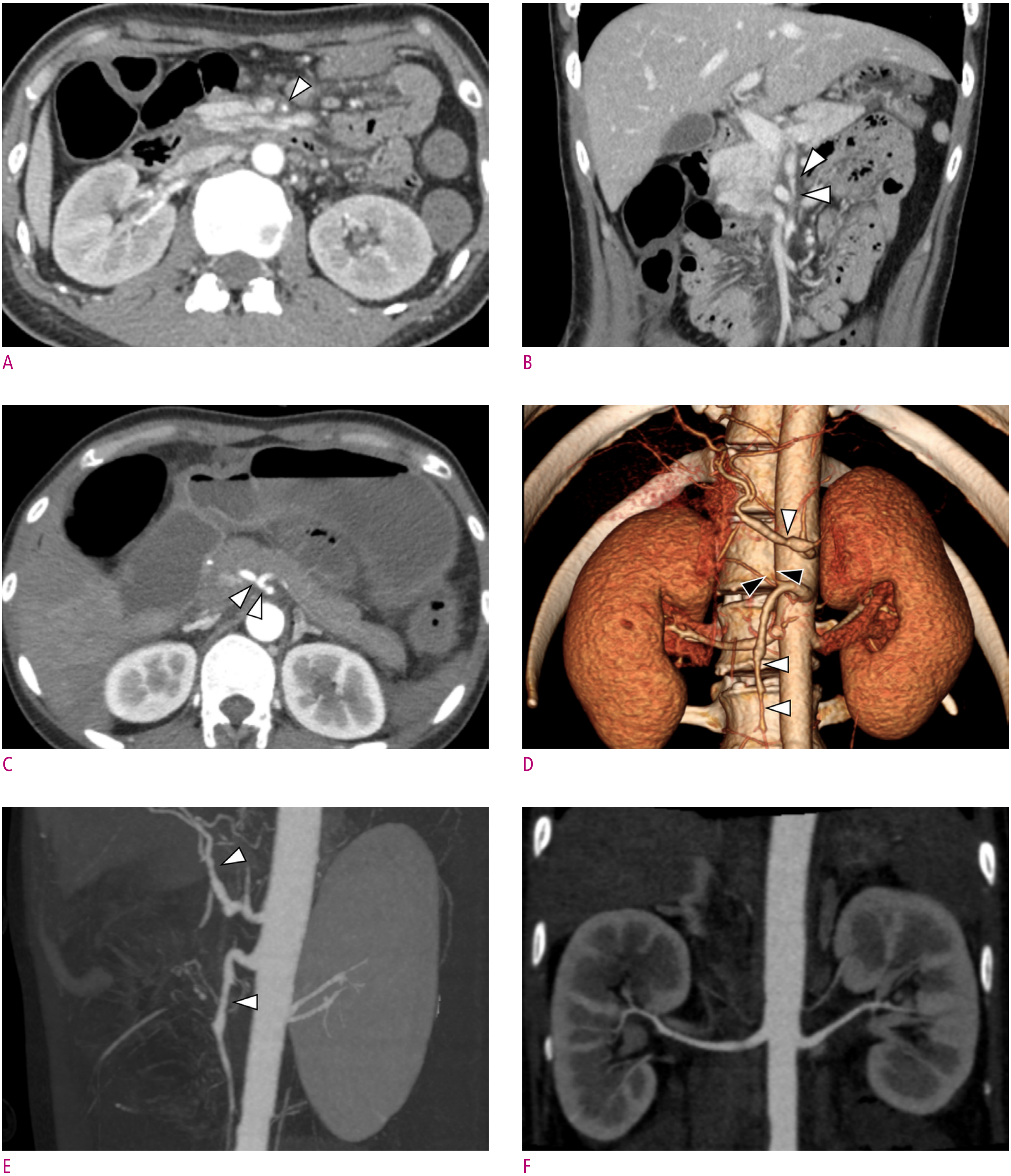

Fig. 1. (A, B) Dynamic CT revealed the segmental narrowing of the proximal superior mesenteric artery (SMA) and (C) multifocal strictures in the celiac trunk and proximal common hepatic artery (arrows). (D, E) CT angiography also showed multifocal luminal narrowing of the celiac trunk and SMA (arrows). An aberrant right hepatic artery from SMA was faintly delineated (black arrows). (F) Both renal arteries were intact.

vasculopathy, and the results were all within the normal range. The SAM was diagnosed based on the patient's history, clinical manifestation, angiography findings, and ruling out other causes.

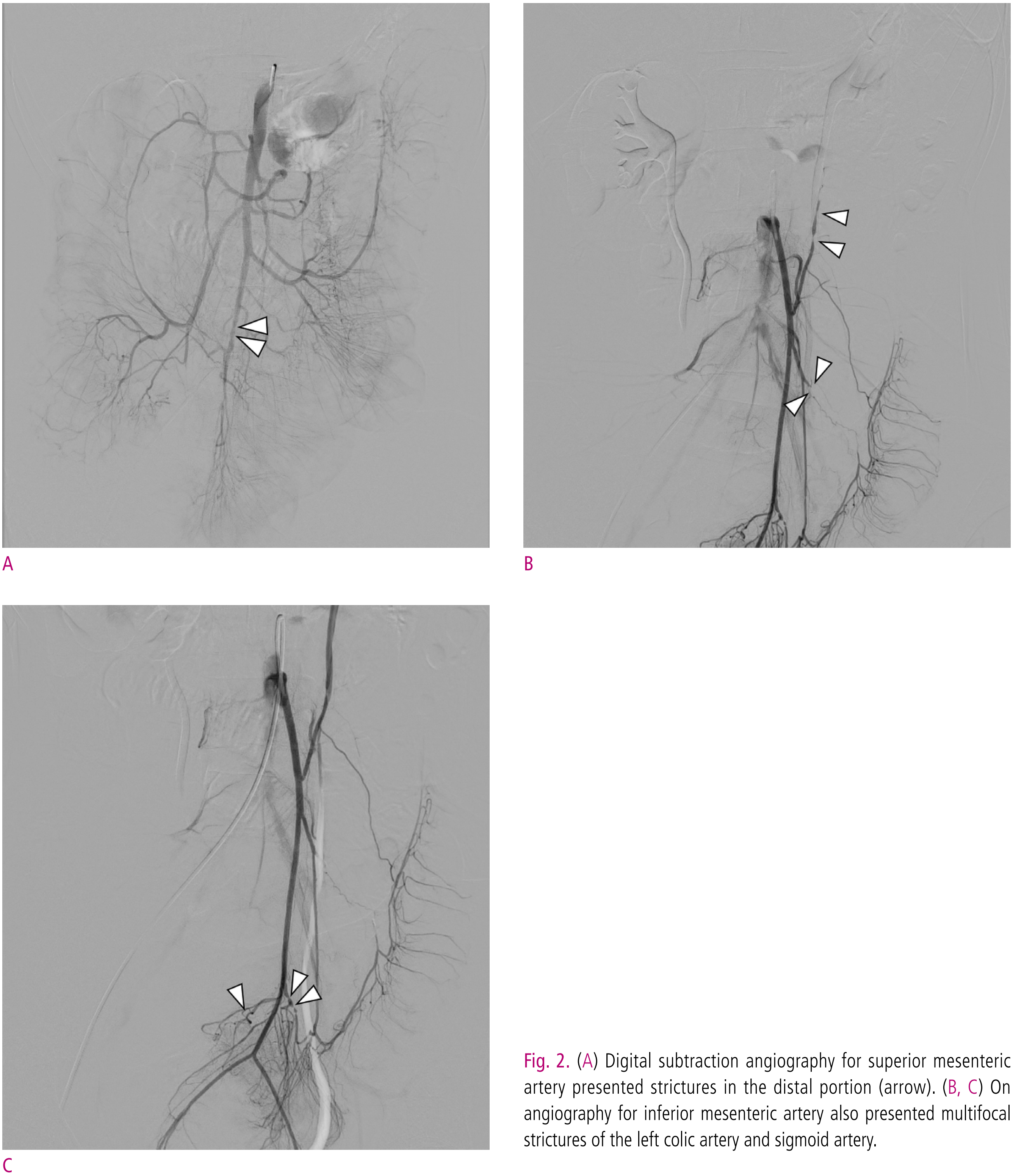

Fig. 2. (A) Digital subtraction angiography for superior mesenteric artery presented strictures in the distal portion (arrow). (B, C) On angiography for inferior mesenteric artery also presented multifocal strictures of the left colic artery and sigmoid artery.

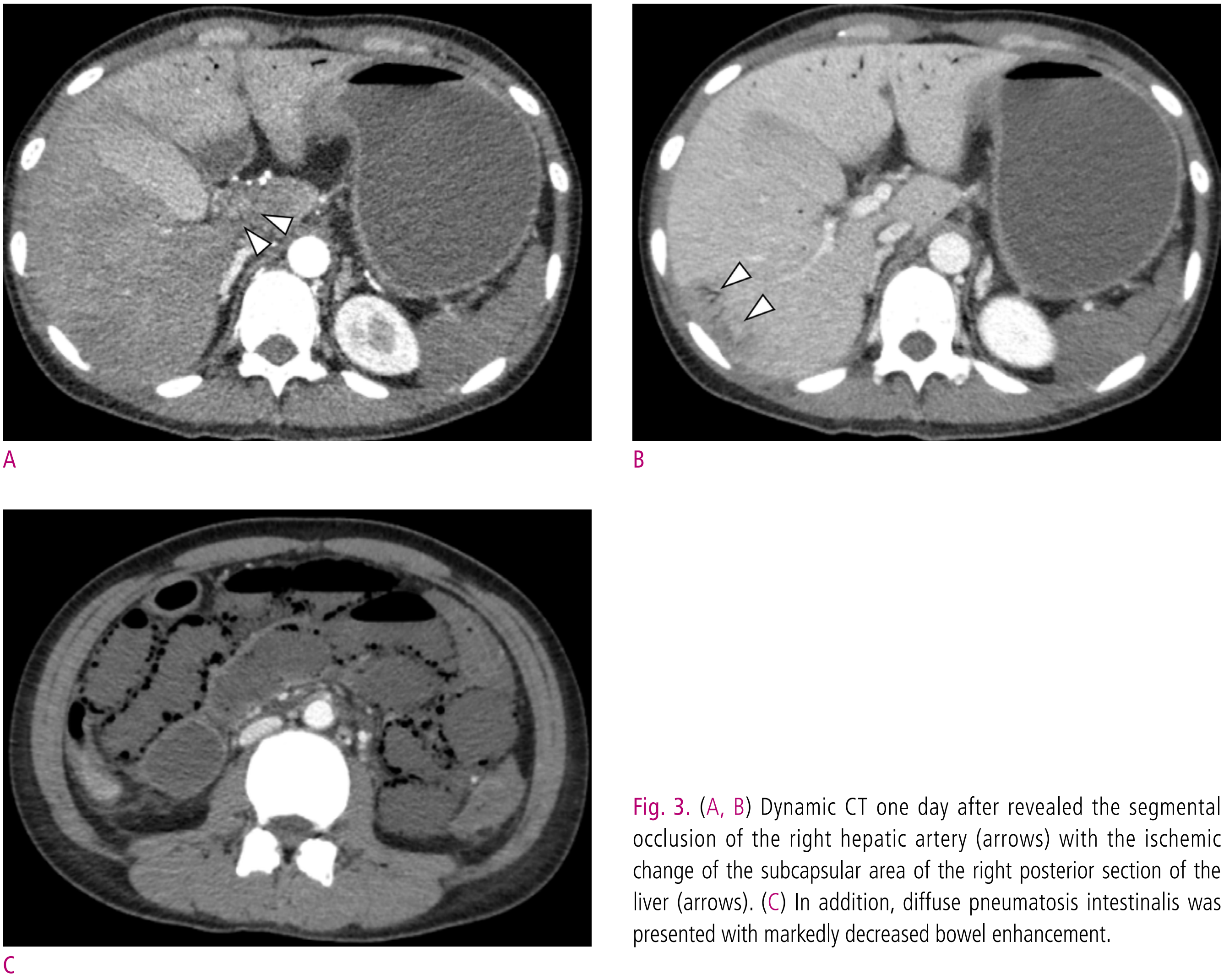

Fig. 3. (A, B) Dynamic CT one day after revealed the segmental occlusion of the right hepatic artery (arrows) with the ischemic change of the subcapsular area of the right posterior section of the liver (arrows). (C) In addition, diffuse pneumatosis intestinalis was presented with markedly decreased bowel enhancement.

Discussion

SAM is a rare arteriopathy with life-threatening manifestations. This lesion is postulated to develop due to cytoplasmic vacuolar degeneration of arteriolar smooth muscle cells. Integration of these vacuoles then leads to disruption of the media, intramural hemorrhage, fibrin deposition at the adventio-medial junction, and granulation tissue formation (4). The most commonly affected vessels are the visceral arteries, followed by the renal, intracranial, abdominal muscular, internal carotid, iliac, pulmonary, and vertebral arteries, and multivessel involvement is common.

The hallmark of angiographic diagnosis is stenosis, occlusion, aneurysmal formation, arterial dilatation, and dissection of medium-sized vessels. Numerous lesions are often identified, affecting arteries in a segmental skip pattern, with the diseased segments demonstrating the involvement of the circumference or only a portion of the arterial wall (5). Arterial dissections account for most of the reported cases of SAM, followed by pseudoaneurysms. When dissection of peripheral arteries unrelated to the aorta is observed, a diagnosis of SAM should be considered (6).

The SAM can mimic other vascular diseases, and the discrimination of SAM is essential because the management options are vastly different. The primary differential diagnoses are atherosclerosis, inflammatory vasculitis, and fibromuscular dysplasia. Atherosclerosis typically occurs at the branch points of vessels and multiple lesions throughout the vascular tree in person with cardiovascular risk factors. SAM is usually confined to vessels of one anatomy site (7). The clinical manifestation, angiographic features, and normal laboratory results of inflammatory and autoimmune factors are helpful to differentiate inflammatory vasculitis such as polyarteritis nodosa and Takayasu's arteritis. Another differential diagnosis with similar angiographic findings to SAM is fibromuscular dysplasia. It also presents a beading appearance. However, it is usually asymptomatic and affects younger patients with predominant involvement of the renal arteries (8). Also, in our case, both renal arteries were relatively intact.

The mortality rate of SAM is as high as 50% in patients who present with life-threatening bleeding, and early diagnosis and detection of disease progression have reduced the mortality rate to 25%. No formal guidelines for the management of SAM exist yet. Recently, catheter-based endovascular techniques can be a successful, minimally invasive treatment option in managing this potentially life-threatening condition and may also provide a temporary bailout measure in the acute phase before definitive surgical treatment at a later stage (2).

In conclusion, SAM is a diagnosis that should not be neglected in patients presenting with sudden-onset abdominal pain and abnormal angiographic findings. Although the mainstay of treatment has generally been surgical intervention, the less invasive endovascular treatment demonstrates an emerging role and is proving successful. In patients placed under disease surveillance, CTA scans at regular intervals are warranted to detect early disease progression.

References

1. Tameo MN, Dougherty MJ, Calligaro KD. Spontaneous dissection with rupture of the superior mesenteric artery from segmental arterial mediolysis. J Vasc Surg 2011;53:1107-1112.
2. Shenouda M, Riga C, Naji Y, Renton S. Segmental arterial mediolysis: a systematic review of 85 cases. Ann of Vasc Surg 2014;28:269-277.
3. Pillai AK, Iqbal SI, Liu RW, Rachamreddy N, Kalva SP. Segmental arterial mediolysis. Cardiovasc Intervent Radiol 2014;37:604-612.
4. Heritz DM, Butany J, Johnston KW, Sniderman KW. Intraabdominal hemorrhage as a result of segmental mediolytic arteritis of an omental artery: case report. J Vasc Surg 1990;12:561-565.
5. Tan R. Segmental arterial mediolysis: a case study and review of the literature in accurate diagnosis and management. Vasc Specialist Int 2019;35:174-179.
6. Naidu SG, Menias CO, Oklu R, Hines RS, Alhalabi K, Makar G, et al. Segmental arterial mediolysis: abdominal imaging of and disease course in 111 patients. AJR Am J Roentgenol 2018;210:899-905.
7. Slavin RE. Segmental arterial mediolysis: course, sequelae, prognosis, and pathologic–radiologic correlation. Cardiovasc Pathol 2009;18:352-360.
8. Slavin RE, Saeki K, Bhagavan B, Maas AE. Segmental arterial mediolysis: a precursor to fibromuscular dysplasia? Mod Pathol 1995;8:287-294.

복부 혈관을 침범한 동맥중막분해증: 증례 보고

강효진[1,2]

[1]서울대학교병원 영상의학과, [2]서울대학교 의과대학 의학과

초 록

동맥중막분해증은 드물지만 치명적일 수 있는 혈관 질환이다. 동맥중막의 원인을 알 수 없는 융해로 인해 혈관 박리, 협착, 동맥류가 발생하며 이로 인한 출혈 혹은 혈관 막힘이 생길 수 있다. 이 증례 보고에서는 복통을 주소로 내원한 34세 여자 환자의 특징적인 혈관 조영 소견, 임상 증상, 혈액 검사소견을 바탕으로 동맥중막분해증을 진단한 증례이다.

KJAR
Korean Journal of Abdominal Radiology

대한복부영상의학회지

투고규정

2017년 1월 6일 제정
2018년 1월 9일 개정
2021년 4월 29일 개정

1. 일반사항

대한복부영상의학회지는 대한복부영상의학회의 공식 학술지로서 연 1회 발간하며, 영문 명칭은 Korean Journal of Abdominal Radiology (KJAR)로 한다. 학술지는 매년 연 1회, 인쇄본의 형태와 온라인(http://e-kjar.org)으로 발간된다.

원고는 국문 혹은 영문으로 작성할 수 있으며, 원고의 종류는 원저, 종설, 임상화보, 증례보고, 특별기고(정책 백서, 원저소개, 편집인에게 보내는 글, 기타) 등으로 구분될 수 있다. 모든 원고는 전자 논문투고 시스템(http://submit.e-kjar.org)을 이용하여 제출한다.

2. 게재윤리사항

2.1. 윤리적 규정

이 학회지에 투고하는 모든 원고는 연구의 대상이 사람인 경우(인체실험의 경우), 헬싱키 선언(Declaration of Helsinki)에 입각하여, 피험자 또는 보호자에게 연구의 목적과 연구 참여 중 일어날 수 있는 정신적, 신체적 위해를 충분히 설명하고, 피험자 또는 보호자로부터 서면 동의서를 받았음을 원고에 명시하여야 한다. 단, 기관 생명윤리 심의위원회 (Institutional Review Boards; IRB)에서 환자 동의서 면제를 승인한 경우는 제외될 수 있다).

연구의 대상이 동물인 경우(동물실험의 경우), 실험 과정이 NIH Guide for the Care and Use of Laboratory Animals에 저촉되지 않고, 소속기관의 동물실험윤리위원회(Institutional Animal Care and Use Committee; IACUC)의 승인을 받았음을 명시하여야 한다.

또한 모든 임상 연구는 공인된 IRB의 승인을 받아야 하고, IRB가 면제를 승인하지 않는 한 연구에 참여하는 모든 피험자(또는 법적 권한이 있는 대리인)로부터 연구 참여에 대한 사전 동의서를 받아야 한다. 또한 필요 시 서면 동의서 및 윤리위원회 승인서의 제출을 요구 할 수 있다. 표절, 중복출간, 연구부정행위 등 연구윤리와 관련된 부분에 대한 처리는 대한의학학술지편집인위원회에서 제정한 '의학논문 출판윤리가이드라인'을 따른다.

2.2. 저자의 정의와 요건

대한복부영상의학회지는 2019년 ICMJE의 저자됨의 권장(http://www.icmje.org/recommendations/)을 따른다. 저자란 출판된 논문에 지적으로 상당한 기여를 한 사람을 말한다. 저자가 되기 위해서는 1) 학술적 개념과 계획 혹은 자료의 수집이나 분석 혹은 해석을 하는 데 있어서 상당한 공헌을 하고, 2) 논문을 작성하거나 중요한 내용을 수정하며, 3) 출간될 원고를 최종적으로 승인하고, 4) 논문의 정확성 또는 완벽성과 관련된 질문에 대해 적절히 설명하고 대답할 수 있는 연구의 모든 측면에 대해 책임을 지는, 이 네 가지의 조건을 모두 만족시켜야 한다. 책임저자는 저자 가운데 1명으로 학술지의 편집인이 보내는 논문 심사의 논평, 수정사항 등을 받아 연락한다. 또한 독자들이 별책(reprints)을 요구하거나 연구팀과의 연락이 필요한 때에 연락이 가능한 연락처가 기재되어 있어야 한다. 논문심사 과정 중 '현재상태로 게재' 결정이 난 후에는 저자의 추가나 책임저자의 변경이 불가능하다. 저자 명단에서 빠지기 위해서는 본인의 의사를 표시하고 서명한 편지를 제출하여야 한다.

2.3 중복게재에 대한 규정

제출된 원고와 동일한 또는 유사한 원고를 다른 학술지(ISSN 등재 학술지)에 게재할 수 없으며, 원고 전체나 원고의 중요한 부분, 표, 그림 등이 다른 학술지에 이미 게재되었거나, 게재 예정인 논문은 게재할 수 없다. 단 사용언어가 다르거나 양측 편집인의 승인이 있을 경우에 허용할 수 있으며, 이때 이차 출간한 논문 표지의 하단(각주, foot note)에 이 논문 전부 혹은 일부가 이미 출간되었음을 알 수 있도록 명시하고 원전을 기술하여야 한다. "This article is based on a study first reported in the [title of journal, with full reference]." 단, 학회 강의록 등과 같이 ISSN 등재 학술지가 아닌 경우에는 해당되지 않는다. 중복게재에 해당하는 것(예; 타 ISSN 등재 저널에 1차로

실린 논문 중 KJAR에 변형, 수록한 경우 등)을 제외하고는 KJAR에 실린 원고도 업적으로 이용할 수 있다. (예; 연수강좌 강의록을 종설로 수정한 경우 등).

2.4. 원고와 관련된 이권과 저작권 양도에 관한 문제

원고와 관련된 연구비를 비롯한 재정적 지원사항과 이권에 대한 문제(conflict of interest, 이해충돌)를 일으킬 수 있는 사항을 빠짐없이 원고의 표지에 명시하여야 한다.

게재 결정된 원고의 저작권은 본 학회에 속하며, 대한복부영상의학회는 원고를 학회지나 다른 매체에 출판, 배포, 인쇄할 수 있는 권리를 가진다.

3. 원고의 종류

A. 원저(Original Article): 원저는 기초 및 임상연구결과의 보고서로서 새로운 정보를 제공할 수 있어야 하고 논문에 포함된 통계기법은 정확해야 한다. 원고의 길이에 제한은 없지만 편집위원회에서 과다한 그림이나 큰 표 등을 제한할 수 있다.

B. 종설(Review): 종설은 특정 주제에 초점을 맞춘 고찰로서 원칙적으로 편집위원회에서 특정 저자에게 위촉한다. 요청받지 않은 논문도 투고 시 편집위원회에서 고려할 수 있다.

C. 임상화보(Pictorial Essay): 임상화보는 질 좋은 사진을 통한 교육이 주목적이며 이미 기정화 된 내용이지만 사진이나 그림들로서 교육적 가치가 크고 훌륭한 경우에 게재한다.

D. 증례보고(Case Report): 복부영상의학분야에 중요한 영향을 줄 수 있는 교육적인 소견을 보고하는 것으로, 영상의학적 진단에 직접적인 관련이 있는 임상소견들을 제시해야 한다.

E. 특별 기고문(Special Report): 본 회지는 위에 기술한 정형화된 원고 이외에 다양한 형식, 다양한 내용의 원고를 게재할 수 있다. 이미 학회지에 출판된 특정 논문에 대한 건설적인 비평 또는 의견, 복부 영상의학 분야의 제반 정책 관련 백서, 혹은 영상의학과 의사의 일반적 관심사항이나 학술분야 특정주제에 관한 기고문을 게재할 수 있다. 별도의 심사과정 없이 편집위원회에서 게재여부를 결정한다. 단 필요에 따라 외부 심사를 의뢰할 수 있다.

4. 원고의 작성

4.1. 일반사항

모든 원고는 한글 또는 영문으로 작성하며 Microsoft Word 최신 버전 사용을 원칙으로 한다. 의학용어의 번역은 가장 최근에 대한의사협회에서 발간한 의학용어집을 사용한다. 글씨 크기는 12 point, 2열 간격(200%)으로, A4용지, letter size용지의 상하좌우에 3 cm의 여백을 둔다. 표지로부터 시작하여 모든 원고에는 페이지 번호를 매겨야 한다. 원고작성에 사용되는 단위는 metric unit이다.

4.2. 표지(Title page)

표지에는 논문 제목과 모든 저자의 이름과 소속기관을 한글과 영문으로 표기하며, 외국인의 경우 영문으로 통일한다. 논문의 제목은 논문 내용을 전달할 수 있는 최소한의 단어로 작성하며 약자는 사용하지 않도록 한다. 다기관 연구에서 소속이 다른 저자들이 포함된 경우 연구가 주로 이루어진 기관을 1번으로 기록하고 그 이외의 기관은 해당 저자 이름에 2번부터 어깨번호를 하고 소속기관을 번호순으로 표기한다. 학위를 포함한 모든 저자명, 모든 저자들의 ORCID ID, 이해 상충, 연구비에 대한 기술이 반드시 포함되어야 한다. 교신저자의 이름, 주소(우편번호), 전화, 팩스 번호 및 E-mail 주소, 간추린 제목(running title), 재정지원 등의 순으로 국문과 영문으로 기재한다. 간추린 제목은 국문은 30자, 영문은 12단어가 넘을 경우 표기한다.

4.3. 본문(Main Body)

내표지는 본문 첫째 페이지로서 국문과 영문으로 논문 제목을 기재한다. 내표지와 본문의 모든 페이지에서 저자(소속, 성명)에 관한 사항은 기술하지 않는다. 영문 약어는 최소화하며 이를 사용할 시에는 최초에 풀어 쓴 후 괄호 안에 약어를 기입한다. 색인용어는 영문 초록의 하단에 MEDLINE/PubMed에서 등재된 MeSH 단어를 5개 선정하여 기입한다.

A. 원저

원저의 원고는 표지, 내표지, 영문과 국문초록(목적, 대상과 방법, 결과, 결론을 구분하여 기술한다)과 색인용어, 서론, 대상과 방법, 결과, 고찰, 요약, 참고문헌, 표, 그림 설명의 순서로 구성한다.

원고 종류	초록 최대 글자 수	최대 그림 수	최대 참고문헌수
종설	영문200단어 또는 한글 400자	30	100
임상화보	영문200단어 또는 한글 400자	40	70
원저	영문300단어 또는 한글 600자	20	50
증례보고	영문200단어 또는 한글 400자	10	20

B. 종설

영문과 국문초록을 특별한 구분 없이 기술하며, 서론, 본론, 결론으로 기술하고, 참고문헌, 표, 그림 설명을 작성한다.

C. 임상화보

영문과 국문초록, 서론, 고찰, 참고문헌, 그림 설명의 순으로 한다.

D. 증례보고

영문과 국문초록을 특별한 구분 없이 기술하며, 서론, 증례 보고, 고찰, 참고문헌, 표, 그림설명의 순서로 구성한다.

4.4. 참고문헌

본문에서 참고문헌을 인용할 때에는 인용 순서대로 번호를 부여하여 아라비아 숫자로 각괄호 안에 표기한다. 문헌 인용 시 가능하면 인용논문의 저자 이름을 사용하지 않을 것을 권고하며, 꼭 필요하여 저자명을 언급하는 경우 국내와 외국저자 모두 영문으로 기재하되 1인일 경우 'Kim (1), Bailey (3)', 2인 이상일 경우 'Park 등(2), Brougham 등(4)'과 같이 기술한다. 국내 저자가 서지사항을 영문으로 기재한 경우에는 외국 저자의 예를 따른다. 참고한 문헌은 따로 REFERENCES 난에 본문에 인용한 순서대로 정리하여 나열한다. 논문의 저자는 최대 6명까지 표시할 수 있으며 7명 이상인 경우에는 앞에서 여섯 번째까지의 저자를 나열하고 나머지 저자는 'et al'로 표시한다. 참고문헌이 온라인으로 발간되어 권, 호가 아직 결정되지 않은 경우는 digital objective identifier (DOI)를 표시해야 한다. 학술지명의 표기는 'Index Medicus'의 학술지 약어를 사용하고 그 외 명시되지 않은 기술 양식은 'The NLM Style Guide for Authors, Editors, and Publishers (http://www.nlm.nih.gov/citingmedicine)'에 따라 기술한다.

Journal articles

1. Yoo BM, Lehman GA. Update on endoscopic treatment of chronic pancreatitis. Korean J Intern Med 2009;24:169-179.
2. Caselli RJ, Dueck AC, Osborne D, Gilman AG, Rall TW, Nies AS, et al. Longitudinal modeling of age-related memory decline and the APOE epsilon4 effect. N Engl J Med 2009;361:255-263.

Books

3. Gilman AG, Rall TW, Nies AS, Taylor P. Goodman and Gilman's the Pharmacological Basis of Therapeutics. 9th ed. New York: Pergamon Press, 1996.

Chapters in books

4. Costa M, Furness JB, Llewellyn-Smith IF. Histochemistry of the enteric nervous system. In: Johnson LR, ed. Physiology of the Gastrointestinal Tract. 2nd ed. Vol. 1. New York: Raven, 1987:1-40.

Conference paper

5. Rice AS, Brooks JW. Canabinoids and pain. In: Dostorovsky JO, Carr DB, eds. Proceedings of the 10th World Congress on Pain; 2002 Aug 17-22; San Diego, CA. Seattle (WA): IASP Press, 2003:437-468.

Online publication

6. Suzuki S, Kajiyama K, Shibata K, et al. Is there any association between retroperitoneal lymphadenectomy and survival benefit in ovarian clear cell carcinoma patients? Ann Oncol 2008 Mar 19 [Epub]. http://dx.doi.org/10.1093/annonc/mdn059.

Web content

7. American Cancer Society.Cancer reference information [Internet]. Atlanta (GA): American Cancer Society, c2009 [cited 2009 Nov 20]. Available from: http://www.cancer.org/docroot/CRI/CRI_0.asp.
8. National Cancer Information Center.Cancer incidence [Internet].Goyang (KR): National Cancer Information Center, c2009 [cited 2009 Oct 20]. Available from: http://www.cancer.go.kr/cms/statics.

4.5. 표

표는 그림에서 알 수 있는 내용을 중복하지 않으며 본문의 내용을 읽지 않고도 설명이 가능하도록 간결 명료하게 작성해야 한다. 표는 별도의 페이지에 작성하며 본문에 인용한 순서대로 아라비아 숫자로 'Table 1.'과 같이 표기하고 이어서 제목을 기술한다. 표준 약어 이외의 약어는 하단 주석에서 기술한다(예: EVR, early virologic response; SVR, sustained virologic response.). 표 하단에는 전체적인 내용 설명, 약어 설명, 기호 설명의 순으로 각각 행을 바꾸어 기재한다. 기호 사용 시 *, †, ‡, §, ‖, ¶, **, ††, ‡‡의 순으로 하며 이를 설명 하단에 표기한다.

4.6. 그림

각각의 그림은 본문에 포함하지 않고 개별 파일로 해상도가 300dpi 이상인 TIFF 형식으로 제출해야 한다. 화살표 등이 포함된 그림은 화살표의 위치를 확인할 수 있는 파일(TIFF, PPT, DOCX 등)을 원본과 별도로 제출해야 한다. 그림은 본문에 인용된 순서대로 번호 지어지며, 동일번호에서 2개 이상의 그림인 경우, 아라비아숫자 이후에 알파벳 글자를 기입하여 표시한다 (예: Fig. 1A, Fig. 1B). 원칙적으로 같은 그림 번호 안에 서로 다른 환자의 그림을 포함시키지 않는다. 모든 그림은 설명을 포함해야 하며 구나 절이 아닌 하나의 문장형태로 기술한다. 모든 그림은 출판에 적합하도록 편집자가 조정할 수 있다.

4.7. 기타

상기 기술된 사항 이외는 대한복부영상의학회지의 편집위원회에서 결정한다.

5. 논문의 투고 및 투고 전 확인 사항

5.1. 논문의 제출

- 모든 원고는 온라인으로 투고하여야 한다. 주요문서와 그림파일을 제출해야 하며 주요문서는 표지, 내표지, 초록, 색인용어, 원고 전문, 참고문헌, 표, 그림 설명을 포함한다.

5.2. 제출 전 확인사항

- 원고의 파일 형태가 적절하다. (.doc, .docx, tiff)
- 논문제목, 저자, 저자들의 소속기관을 한글과 영문으로 표기한 표지를 독립된 파일로 작성한다
- 문서는 원고의 종류에 따른 규정을 준수하였다. 그림은 각각의 파일로 이루어져 있다.
- 이전에 출판되었던 내용은 재출판에 대한 편집인의 동의서가 준비되었다.
- 모든 저자의 동의서가 준비되었다.

6. 논문의 심사 및 게재

제출된 원고는 편집위원회에서 해당분야 전문가에게 심사를 요청하고 그 결과에 근거하여 게재여부를 결정하며 원고의 수정 및 보완 사항을 저자에게 권고한다.

논문 심사 후 저자는 심사결과에 따라 심사의견서 내의 지적사항을 토대로 논문을 수정 작성해야 한다.

IOHEXOL

BONOREX®

240 / 300 / 350

최적의 농도

BONOREX® 240/300/350주

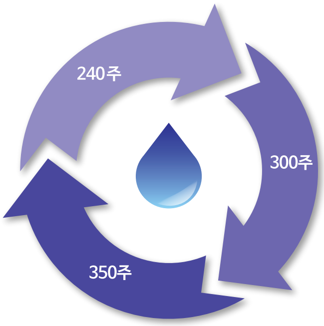

보노렉스는
240, 300, 350 mgI/mL의
최적의 농도가 있어
검사에 따라 **합리적인 선택**을
할 수 있습니다.

합리적인 용량

BONOREX® 130 mL

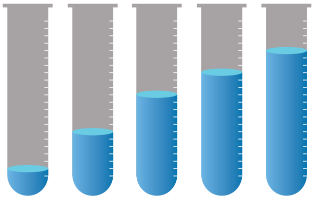

보노렉스 130 mL는
CT 장비의 발전에 따른
조영제 사용량 감소 추세에 맞춰
국내 최초로 발매한
130 mL 포장 단위입니다.

다양한 포장용기

– 병(유리/PP), 관, 백

보노렉스는
병(유리/PP) 뿐만 아니라
관 등 **다양한 포장용기**를 통해
환자의 안전성과 **사용자의 편의성,**
의료기관의 경제성을
높일 수 있습니다.

CMS
Central Medical Service
센트럴메디컬서비스(주)
Central Medical Service
www.cmscorea.co.kr / Tel.+82-2-3394-5161~3 / Fax.+82-2-3394-5165

www.withhealthcare.com

With Safety
With Omnihexol

New manufacturing process
Innovation non-ionic
Low osmolar and Contrast agent

omnihexol® Inj.

iohexol 300mg / 350mg

판매원 : 위드헬스케어 WITH HEALTHCARE

Scanlux® 300/370

Dasol Life Science

SANOCHEMIA
Diagnostics International

HOOD05162003045893

The clinical overlay is not that of the individual pictured.
It was modified for better visualization. · 8186 1019

MAGNETOM Vida with BioMatrix

Embrace human nature at 3T

siemens-healthineers.com/vida

The first 3T BioMatrix system

The increasing number of exams, complexity, and cost-pressure are placing challenges on MRI. 3T MRI needs to better handle patient variability, deliver robust results for all patient types, and become more cost-effective.

MAGNETOM Vida, the first MR scanner with BioMatrix Technology, is equipped to master the challenges facing MRI today. 3T MRI with BioMatrix meets these needs with fewer rescans, predictable patient scheduling and consistent, high-quality personalized exams.

Embrace full 3T performance
with unparalleled magnet and gradient power

Embrace true 3T productivity
with GO Technologies

Embrace new 3T clinical capabilities
with Inline Compressed Sensing

SIEMENS Healthineers

GE Healthcare

There is a

Constant

On the radiology landscape[1]

Over 800 million patients

More than 100 countries

Over 36 years' experience

Over 6,500 published clinical articles

+PLUSPAK™
(polymer bottle)

Efficient storage and disposal
No sharp alloy ring pull
Efficient labeling

imagination at work

OMNIPAQUE™
IOHEXOL

Reference. 1. Data on file, GE Healthcare Ltd.

효능·효과: 척수조영, 혈관조영, 정맥요로조영 (IVP), CT 조영증강, 체강조영 (관절조영, ERP/ERCP, 헤르니아조영, 자궁난관조영, 침샘조영, 소화관조영) **용법·용량:** 일반적으로 다른 요오드계 X 선 조영제와 같은 요오드 농도, 용량을 사용하며, 투여 전후에 충분한 수분공급을 합니다. 추천 투여용량은 제품설명서를 참고하시기 바랍니다. **금기:** 1) 이 약 및 이 약의 구성성분, 요오드계 약물에 과민반응 및 그 병력이 있는 환자 2) 중증 갑상샘 질환환자 3) 중증 국소감염 또는 균혈증과 같은 전신감염이 있는 환자에 대한 척수조영 **신중투여:** 1) ① 극도의 전신 쇠약 환자 ② 기관지천식 환자 ③ 중증 심장애 환자 ④ 중증 간장애 환자 ⑤ 중증 신장애 환자 ⑥ 급성 췌장염 환자 ⑦ 마크로글로불린혈증 환자 ⑧ 다발성골수종 등의 형질세포질환 환자 ⑨ 강직증 환자 ⑩ 갈색세포종 환자 및 질환 의심자 2) 본인 또는 가족이 기관지 천식, 발진, 두드러기 등의 알레르기를 일으키기 쉬운 체질인 환자 3) 약물 과민반응의 병력이 있는 환자 4) 탈수 증상이 있는 환자 5) 고혈압 환자
※본 제품에 대한 자세한 내용은 제품 설명서를 참고하십시오

서울특별시 중구 한강대로 416 서울스퀘어 15층
Tel: 02-6201-3700 Fax: 02-6201-3801

© 2018 General Electric Company -
All rights reserved. Omnipaque is a trademark of
GE Healthcare Limited

JB1494KO

XENETIX®

Iobitridol

Flow
of **contrast**

Guerbet | COMMITTED

• **수입 및 판매원:** 게르베 코리아㈜ 서울특별시 강남구 테헤란로38길 10, 6층